MAGNESIUM ISOTOPE INVESTIGATION OF STROMATOLITIC KNOBS IN STORR'S LAKE, SAN SALVADOR, BAHAMAS: IMPLICATIONS FOR ORGANOMINERALIZATION AND LAMINAE FORMATION

by

ZIJIAN LI

Presented to the Faculty of the Graduate School of

The University of Texas at Arlington in Partial Fulfillment

of the Requirements

for the Degree of

MASTER OF SCIENCE IN ENVIRONMENTAL AND EARTH SCIENCES

THE UNIVERSITY OF TEXAS AT ARLINGTON

AUGUST 2017

Acknowledgements

I would like to thank all of those who supported me throughout the duration of my Master's research. Acknowledgment is made to the Donors of the American Chemical Society Petroleum Research Fund for support of this research.

I offer my sincerest thanks to my advisor, Dr. Elizabeth Griffith, for supporting me with unfailing patience, friendship, and instruction. Thanks to her, I expanded my scientific horizons and improved my ability, both in research and in laboratory operation. Special thanks to Dr. Merlynd Nestell and Dr. Majie Fan for joining my committee, for offering opportunity and help to do my research in their labs, and for exhaustive proofreading of my thesis.

I would like to thank Dr. David Wronkiewicz from Missouri University of Science and Technology for his tremendous help in the field trip and in the research work. I would also like to thank Dr. Varun Paul from Mississippi State University for sharing his data and ideas to promote the project.

Special thanks to my friends in Dr. Griffith's group for their kind help in the lab work and their pertinent advice for my presentations.

I would also like to thank all of my colleagues at the Department of Earth and Environmental Sciences in The University of Texas at Arlington. Thanks to Dr. Matthew Loocke for instructions on operating instruments. Thanks to Mike Read for teaching me how to make thin sections. Thanks to Lu Zhu for her help in stable isotope analysis of my samples. Thanks to Christopher Borjas for teaching me to epoxy my sample by using a vacuum impregnation system. Thanks to Larisa Komarnitskaya and Darsa Wright for their kind help whenever I had problems.

I can never fully express my gratitude to my family, who have always believed in me without fail, and never let me give up.

Finally, I thank Yuxiang Zhang, my office mate and my roommate, for his assistance when needed, for sharing happiness, and for listening to my rants.

July 21, 2017

Abstract

MAGNESIUM ISOTOPE INVESTIGATION OF STROMATOLITIC KNOBS IN STORR'S LAKE, SAN SALVADOR, BAHAMAS: IMPLICATIONS FOR ORGANOMINERALIZATION AND LAMINAE FORMATION

Zijian Li, MS

The University of Texas at Arlington, 2017

Supervising Professor: Elizabeth M. Griffith

Storr's Lake, a hypersaline lake located on San Salvador Island, Bahamas, contains modern, fine-grained stromatolites. This study focused on two morphological types of stromatolitic mounds in Storr's Lake (pinnacle mound and plateau-mushroom) and systematically investigated their mineralogy, elemental abundance, carbon, oxygen and magnesium (Mg) isotopic signature to gain insights into the organomineralization process and laminae formation of stromatolites. In addition, the hydrochemistry of Storr's Lake was characterized by in situ measurement of water parameters, elemental analysis, and Mg isotope investigation. Cations and anions analysis indicates the lake is spatially homogenous and shows little seasonal variation. Mg isotope analysis of the lake water suggests seawater is the primary Mg source to the Storr's Lake and dominates the Mg isotopic budget of the lake.

X-ray diffraction studies showed that the surficial crusts of both types of stromatolites are enriched in high-Mg calcite and their interior zones are dominated by aragonite. The mineralogic distribution is consistent with the variations of Mg/Ca and Sr/Ca molar ratios of stromatolitic sublayers. The organominralization processes

mediated by both photosynthetic and heterotrophic microbial metabolisms result in in situ micritic precipitation. The more negative $\delta^{13}C$ signature of deeper sublayers suggests organomineralization processes continue at deeper horizons, whereas the relatively uniform and positive $\delta^{18}O$ values are controlled by the evaporitic condition of the lake. An increase in the Mg/Ca molar ratio within microbial mats is assumed to be responsible for the hypothesized mineral phase transformation from initial high-Mg calcite to aragonite. The Mg isotopic composition ($\delta^{26}Mg$) of stromatolitic sublayers falls within the range of values previously reported for biogenic high-Mg calcite and aragonite, and displays strong dependence on mineral compositions. The difference between the $\Delta^{26}Mg_{carbonate\text{-}lake\ water}$ values in this study from the $\Delta^{26}Mg_{carbonate\text{-}solution}$ values of abiogenic precipitation experiments suggest vital effects on Mg isotope fractionation during organomineralization of high-Mg calcite but not aragonite. A mechanism for organomineralization and laminae formation is proposed by comparing stromatolites from Storr's Lake and other environments (hypersaline, open marine, and freshwater), which may have crucial implications for interpreting the ancient stromatolites in the fossil record.

Table of Contents

List of Illustrations

List of Tables

Chapter 1

Introduction

Microbialite Definition and Classification

Organisms play a role in calcium carbonate precipitation via two major mechanisms: biomineralization and organomineralization (Dupraz et al., 2009). Calcium carbonate precipitated via biomineralization (biological controlled mineralization) is typically produced by living organisms to harden or stiffen existing tissues and/or skeletons, therefore the morphology of the mineral is genetically controlled by organisms, e.g., coral and clams (Dupraz et al., 2009).

Organomineralization, on the other hand, is not directly genetically controlled. The precipitation of calcium carbonate formed by organomineralization (biologically influenced or biologically induced mineralization according to Dupraz et al. (2009)) can be intrinsically (e.g., microbial metabolisms) or extrinsically (e.g., degassing, evaporation) driven, and thus the morphology of the mineral is mainly controlled by environmental conditions. Key components of organomineralization are the “alkalinity” engine (microbial metabolism and environmental conditions impacting calcium carbonate saturation) and an organic matrix comprised of extracellular polymeric substances (EPS), which may provide a template for carbonate nucleation (Dupraz et al., 2009). A microbial community can produce different morphologies as conditions change due to environmental factors such as seasonal variation, storm events, changes in salinity or sedimentation rates (Dupraz et al., 2009).

When microbial communities drive organomineralization to form carbonate structures, the structure is known as a microbialite. A microbialite, as defined by Burne and Moore (1987), is an organosedimentary deposit resulting from interactions between benthic microbial communities and detrital or chemical sediments (in calcareous

microbialites; construction processes include trapping and binding, inorganic calcification (tufa), and biologically influenced calcification). Because morphology is not genetically controlled, it is difficult to discriminate the morphology of a microbialite from a structure that formed abiotically in the rock record. Currently, it is not fully understood why modern microbialites form certain morphologies, or form at all, in certain places on Earth, and form different morphologies, or do not form at all, in other places with similar conditions (Dupraz et al., 2009).

Although a seemingly infinite number of varying morphologies can be formed through microbial organomineralization, a microbialite can be classified into one of three main types of structures based on their internal morphologies (Figure 1-1): (1) a stromatolite, which has a laminated internal fabric, (2) a thrombolite, which has a clotted internal fabric, and (3) a leiolite, or cryptic microbial crust, which is structureless with no defined internal fabric (e.g., Aitken, 1967; Kennard and James, 1986; Braga et al., 1995; Dupraz and Strasser, 1999, 2002; Riding, 2000; Shapiro, 2000; Turner et al., 2000). Of the three types, stromatolites have received the most attention by the scientific community. This choice is perhaps due, in part, to the fact that stromatolites are considered to be among the oldest traces of life in the rock record (Hofman et al., 1999; Allwood et al., 2006, 2007).

In an early Earth, before the advent of plants, animals, and other eukaryotes, stromatolites would have dominated the global carbon cycle, having significant impacts on Earth's climate and atmosphere. The oldest known stromatolite has an age of 3500 Myr (Schopf, 2006). Stromatolites then became widespread and abundant in the Proterozoic (Figure 1-2; Schopf, 2006). The abundance of microbiallites had a rapid initial decline followed by relatively minor changes during the Phanerozoic (Figure 1-2B; Riding, 2000). Thus, understanding the organomineralization processes of ancient stromatolites

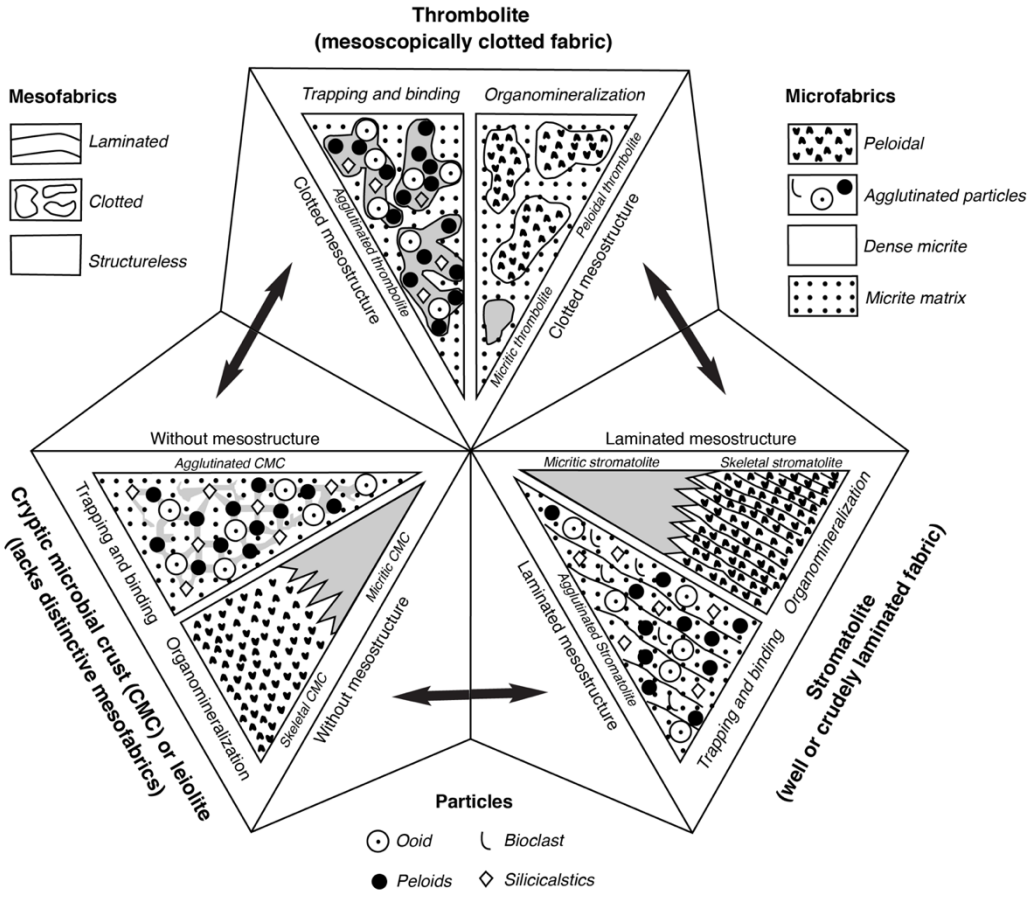

Figure 1-1 Classification of a microbialite based on meso- and microfabrics. Figure from Dupraz and Strasser (1999).

is critical to understanding Earth's history. Fossil stromatolites display a wide range of macroscopic morphologies, but all include a laminated mesostructure (Riding et al., 1991; Riding, 2000). Most fossil stromatolites that have been discovered have a fine-grained, micritic microstructure (Riding et al., 1991; Riding, 2011) and may contain chert and dolomite due to diagenetic changes (Sommers et al., 2000). Although modern stromatolites do not have a profound impact on today's global carbon cycle, the modern structures can provide a better basis for comparison and a gateway to understanding the

fossil record. Modern stromatolites can be seen today in places such as Shark Bay, Australia (e.g., Reid et al., 2003), Highbourne Cay and Exuma Islands, Bahamas (Reid et al., 2000; Dupraz et al., 2004; Glunk et al., 2011); and in Storr's Lake, San Salvador Island, Bahamas (Neumann et al., 1989; Dupraz et al., 2013; Paul et al., 2016), the field site for this study.

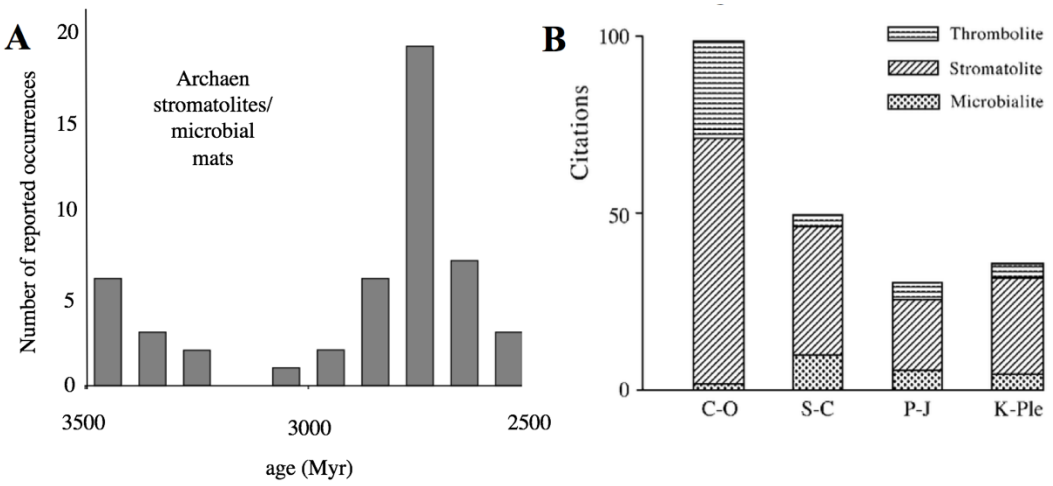

Figure 1-2 Temporal distribution of the reported occurrence of microbialites/microbial mats in geological history. (A) Archean and (B) four Phanerozoic intervals of similar time span: Cambro-Ordovician (97 Myr), Silurian-Carboniferous (145 Myr), Permian-Jurassic (154 Myr), Cretaceous-Pleistocene (145 Myr) (Harland et al., 1990). These rough data suggest rapid initial decline followed by relatively minor changes in abundance of microbial carbonates during the remainder of the Phanerozoic. Modified from Riding (2000) and Schopf (2006).

Microbial Mat and Microbialite Formation

Microbial mats are centimeter-thick microbial ecosystems formed by a multi-layered sheet of microorganisms (Reimer, 2011). Microbial mats grow at interfaces between different types of material, mostly on submerged or moist surfaces, but a few survive in deserts (Schieber et al., 2007). The propensity of microbial mats to trap, bind,

and precipitate sediments results in the formation of sedimentary structures such as stromatolites (Riding, 2000).

Typically, formation of a microbialite begins with the colonization of sediment by cyanobacteria (Reid et al., 2000). Cyanobacteria are most active ~0.5 to 2 millimeters below the sediment surface (Dupraz et al., 2013). Active cyanobacteria display high rates of photosynthesis and many can fix nitrogen in addition to creating organic carbon and oxygen through oxygenic photosynthesis, and thus create a sharp increase in oxygen concentration a few millimeters below the sediment.

Shortly after colonization by cyanobacteria, aerobic (chemoorgano) heterotrophs appear and gain energy from the organic carbon, fixed nitrogen, and oxygen created by the cyanobacteria according to the following reaction (Visscher and Stolz, 2005):

$$<CH_2O> + O_2 \rightarrow CO_2 + H_2O + \text{energy} \quad (1\text{-}1)$$

The oxygen produced by the cyanobacteria is consumed by aerobic heterotrophic chemical reactions. Anaerobic heterotrophs, specifically sulfate reducing bacteria (SRB) in marine and hypersaline environments, also play a role in the microbial community. SRB gain energy from the organic carbon created by the cyanobacteria along with the high sulfate concentrations in seawater according to the following reaction (Patterson and Walter, 1994):

$$<2CH_2O> + SO_4^{2-} \rightarrow 2HCO_3^- + 2H_2S \quad (1\text{-}2a)$$

$$2HCO_3^- \rightarrow CO_3^{2-} + CO_2 + H_2O \quad (1\text{-}2b)$$

Chemolithoautotroph (such as sulfide-oxidizing bacteria (SOB)) can then colonize and gain energy from the sulfide generated and create biomass from the carbon dioxide created by the SRB (Equation 1-2b) according to the following reaction (Visscher and Stolz, 2005):

$$2CO_2 + H_2S + 2H_2O \rightarrow 2<CH_2O> + SO_4^{2-} + 2H^+ \quad (1\text{-}3)$$

The sulfate created by the SOB will also feed the metabolisms of the SRB, which will in turn create more sulfide that can be used by the chemolithoautotrophs. Other chemolithoautotrophs, such as purple and green sulfur bacteria, can also use sulfide and carbon dioxide to create biomass, and will also produce elemental sulfur according to the following reaction (Visscher and Stolz, 2005):

$$CO_2 + 2H_2S \text{ --> } <CH_2O> + 2S^0 + H_2O \quad (1\text{-}4)$$

All of these different types of bacteria can create a mature, metabolically diverse microbial mat with complex element cycling. Physiological activities of the bacterial community in a mat can promote precipitation and/or trapping and binding of sediment within the mat (Visscher and Stolz, 2005). Generally, microbial metabolisms influence carbonate precipitation in two facets: (i) controlling the pH of the proximal microenvironment, and (ii) regulating the nucleation sites and cation availability through producing and/or degrading extracellular polymeric substances (EPS) (Dupraz and Visscher, 2005).

The transfer of CO_2 within microbial mats influences the pH of the microenvironment and thus plays a role in regulating carbonate precipitation. Both photosynthesis (primarily by cyanobacteria) and respiration (both by aerobic and anaerobic heterotrophs) of microbial systems involve the transfer of CO_2. Photosynthesis is normally simplified as:

$$CO_2 + H_2O + \text{light} \text{ --> } <CH_2O> + O_2 \quad (1\text{-}5)$$

whereas carbonate precipitation and dissolution occur according to the following reaction:

$$Ca^{2+} + 2HCO_3^- \text{ <--> } CaCO_3 + CO_2 + H_2O \quad (1\text{-}6)$$

When photosynthesis occurs, it consumes CO_2 (increasing the pH) and shifts the direction of the reaction (Equation 1-6) to the right and favors precipitation of carbonate.

Because respiration is roughly the reverse process of photosynthesis, CO_2 is generated (pH decreases) and the direction of the reaction (Equation 1-6) moves to the left which promotes carbonate dissolution.

The organic EPS matrix is considered to be primarily produced by cyanobacteria in microbial mats (De Philippis et al., 1998). EPS may include protein, peptides, non-carbohydrate acidic moieties, and even extracellular DNA (Sutherland, 2001). Negatively-charged functional groups within the EPS matrix can bind a large amount of mono- or divalent cations (e.g., Ca^{2+} and Mg^{2+}) to maintain structural integrity (Sutherland, 2001). $CaCO_3$ precipitation can commence when metal cations and dissolved inorganic carbon (DIC) are liberated due to degradation or alteration of EPS (Dupraz et al., 2009). Thus the combined actions of SRB and fermentative organisms could be responsible for the consumption of EPS and precipitation of $CaCO_3$. In addition, changes in the amount or type of EPS can also influence the rate of precipitation, mineralogy, and morphology of the crystalline phase (Braissant et al., 2003). The gel-like property of the EPS matrix in which precipitation occurs influences diffusion processes and adsorption/complexation of Ca^{2+}, both of which affect the mineral product (Given and Wilkinson, 1985). Variations in Mg concentration within the EPS matrix when supersaturation is reached produce distinct morphologies such as spheres, dumbbell-like, wheat-sheaf-like bundles or rhombs (Fernandez-Diaz et al., 1996). Organic molecules of EPS can attach and poison specific crystal faces, thereby inhibiting a part of the crystal growth, which leads to the formation of spherulite, dumbbell or smooth rhombic crystals (Zavarzin, 2002). A recent study found that ~100 nm-amorphous calcium carbonate crystals precipitate within the EPS matrix (Benzerara et al., 2006).

Lamination in a stromatolite is defined as the alternation of dark and light layers which is typically attributed to episodic growth of different micro-fabric mat communities.

Stromatolite formation is typically attributed to the process of trapping and binding of sediment and/or $CaCO_3$ precipitation associated with the photosynthetic uptake of CO_2 and HCO_3^- by different microbial mats. The associated micro-fabric mat communities include: (i) a trapping and binding community, characterized by predominantly vertically oriented filaments of cyanobacteria (Kennard and James, 1986), (ii) a carbonate micrite-precipitating community that consists of horizontally oriented coccoid cyanobacteria and heterotrophic bacteria embedded in a dense EOM-rich biofilm (Reid et al., 2000), and (iii) a community of microboring cyanobacteria, the action of which results in fused grains (Dupraz et al., 2013). During rapid sediment accretion, vertically oriented cyanobacterial filaments trap and bind carbonate sand or ooids to form grainy laminae, which are dark in appearance (Suarez-Gonzalez et al., 2014). Sometimes, the calcified cyanobacterial filaments are also involved in these laminae (Planavsky and Ginsburg, 2009). At hiatal intervals, thin micritic crusts occur as light colored laminae, which are chiefly bio-induced by the degradation of EPS from SRB at anaerobic conditions (Suarez-Gonzalez et al., 2014). In addition, strong activity of microboring cyanobacteria diagenetically obliterates the microstructure of preformed laminae (Dupraz et al., 2013; Figure 1-3).

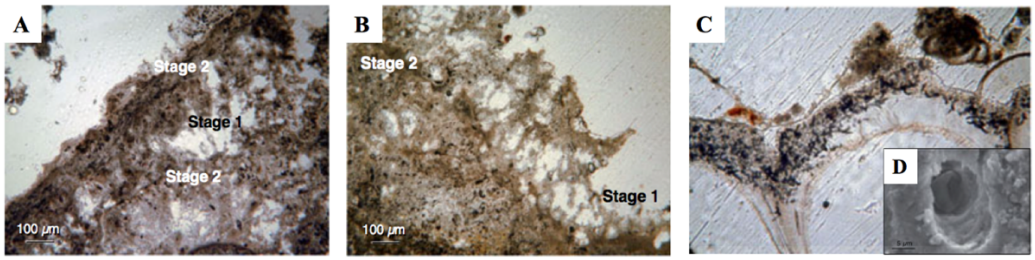

Figure 1-3 Thin section and scanning electron microscopy (SEM) images of a 'subfossil' *Scytonema* knob from Storr's Lake, Bahamas. (A-B) relics of cyanobacterial filaments. Stage 1 in subfossil knobs shows precipitation along vertically oriented filaments, whereas Stage 2 is characterized by horizontally oriented filaments (Dupraz et al., 2013). Some of the precipitated micrite displays black dots that represent microboring by coccoid cyanobacteria [see also (C)]; (C) trapped gastropod shell within a 'subfossil' knob, showing extensive bioerosion by coccoid cyanobacteria; (D) SEM image of a coccoid cyanobacterium in a microborehole. Adapted from Dupraz et al. (2013).

Thrombolites, mesoscopically clotted (unlaminated) microbialites, are not uniformly distributed in the rock record, but are essentially a Cambrian and Lower Ordovician phenomenon (Figure 1-2B; Kennard and James, 1986). Although once prevalent on the ancient Earth, modern accreting thrombolites are rare. One of the few modern sites of active thrombolitic development (open marine thrombolites) is the island of Highbourne Cay, Exuma, Bahamas (Myshrall et al., 2010). Several hypotheses exist about thrombolite formation. Thrombolite formation has been attributed to rapid rates of calcification by coccoid cyanobacteria (Konhauser, 2007; Myshrall et al., 2010). A decrease in salinity, and increase in energy and nutrient supply, and deepening water are possible factors that result in the transformation of a stromatolite to a thrombolite (Feldmann and McKenzie, 1998). More study is needed to understand how the clotted internal fabric of a thrombolite is formed.

Early Diagenesis

Original microbial carbonate fabrics have the potential to be modified by penecontemporaneous diagenesis. During early diagenesis, there is localized carbonate dissolution as well as recrystallization of secondary carbonate cements. The clotted fabric of thrombolites is observed as patchy fine-grained carbonate cements under the microscope, which supports the idea that clot formation is linked with early diagenetic processes (Planavsky and Ginsburg, 2009). Sparitic infilling of the porosity left by the cyanobacterial filaments will also take place in the early stage of diagenesis, accompanied by active microboring (Dupraz et al., 2013). Another effect of early diagenetic alteration is the dilution of the initial positive $\delta^{13}C$ signature of microbial metabolisms (photosynthesis renders precipitated carbonate enriched in ^{13}C, whereas heterotrophic respiration transforms organic carbon to bicarbonate ions and forms carbonate with lower $\delta^{13}C$ values, which were produced during early precipitation (Dupraz et al., 2013).

Mg Isotope Systematics

Notation

Magnesium is a fluid-mobile major element having three stable isotopes, ^{24}Mg, ^{25}Mg and ^{26}Mg, with natural abundances of 78.99%, 10.00% and 11.01%, respectively (Rosman and Taylor, 1998). The relative mass difference between ^{26}Mg and ^{24}Mg is >8%, which is the second largest among the non-traditional stable isotopes (Johnson et al., 2004). This characteristic may potentially produce large Mg isotopic fractionations during low-temperature incorporation of Mg into carbonates due to pronounced vibrational energy differences at low temperature. Measured Mg isotope values are reported in delta

(δ) notation as permil (‰, parts per thousand) deviations from the isotopic composition of the standard ("std", or DSM3 for Mg isotopes):

$$\delta^{x}\mathrm{Mg}(‰) = [\left({}^{x}\mathrm{Mg}/{}^{24}\mathrm{Mg}\right)_{sample}/\left({}^{x}\mathrm{Mg}/{}^{24}\mathrm{Mg}\right)_{std} - 1] \times 1000 \qquad (1\text{-}7)$$

where x refers to 25 or 26.

The isotopic fractionation associated with the equilibrium isotope exchange reaction between two substances A and B (i.e., the mass dependent isotopic fractionation of A relative to B) can be expressed by use of the isotope fractionation factor α (alpha):

$$\alpha_{A-B} = R_A/R_B \qquad (1\text{-}8)$$

where $\mathrm{R_A}$ and $\mathrm{R_B}$ are the isotope ratios (heavy isotope over light isotope) of the two phases, A and B (White, 2015).

The Mg isotope fractionation can be expressed as fractionation value which is defined as (Galy et al., 2003):

$$\Delta^{26}Mg_{A-B} = \delta^{26}Mg_A - \delta^{26}Mg_B = 1000\ ln\alpha_{A-B} \qquad (1\text{-}9)$$

Mg isotopes to trace nucleation and precipitation

In most cases, light Mg isotopes are preferentially incorporated into biogenic and abiogenic carbonates from an aqueous phase (e.g., Wombacher et al., 2011; Li et al., 2012). Due to Mg directly substituting for Ca within the carbonate lattice, Mg may be expected to fractionate isotopically in a manner similar to Ca (Gussone et al., 2003, 2005; Chang et al., 2004; Lemarchand et al., 2004; Marriott et al., 2004; Fantle and Depaolo, 2007; Tang et al., 2008a, b; Depaolo, 2011; Pearce et al., 2012). First principle calculations demonstrate that the observed Mg isotope fractionation in hydrous Mg carbonates and other minerals such as calcite and dolomite are likely due to the stability and coordination of different Mg isotopes in the precipitated mineral versus the fluid phase (Schauble, 2011), which suggests that mineralogy is an essential factor that

dominates the Mg isotopic compositions of carbonates. Previous work has shown that aragonite has a more positive Mg isotopic composition compared to calcite (Wombacher et al., 2011). The difference is because the length of the Mg-O bond in calcite is ~2.12 Å (6-fold coordination), whereas it is 2.08 Å (9-fold coordination) in aragonite (Finch and Allison, 2008). Shorter bonds have higher energy and are therefore are enriched in the heavier isotopes. There are also different extents of Mg isotopic offsets (i.e., isotopic fractionation) during precipitation of high-Mg calcite and low-Mg calcite (Eisenhauer et al., 2009).

For a specific carbonate mineral (calcite or aragonite), inorganic (abiotic) precipitation experiments have shown that equilibrium mass dependent isotope fractionation of Mg appears to have a modest temperature-dependence, but is independent of solution Ca and Mg content, P_{CO_2}, pH, and Mg/Ca (Li et al., 2012; Wang et al., 2013). Although measurable Mg isotope fractionation was found during hydrous Mg carbonate precipitation induced by cyanobacteria photosynthesis, the presence of biofilms and other heterotrophic bacteria has been found to have an insignificant effect on the overall Mg isotopic fractionation factor (Shirokova et al., 2013).

Mg isotopes to trace early diagenesis

Numerical modeling suggested that with respect to Mg isotopes, the diagenetic fractionation factor ($\alpha_{\text{diag}}^{\text{Mg}} = \frac{(^{26}\text{Mg}/^{24}\text{Mg})_{\text{diagnetic carbonate}}}{(^{26}\text{Mg}/^{24}\text{Mg})_{\text{fluid}}} = 0.9955$) was appropriate for limestone diagenesis (Fantle and Higgins, 2014) and was consistent with the fractionation factor (0.996) derived from calcite recrystallization in deep-sea carbonate sediments (Higgins and Schrag, 2012). Diagenetic recrystallization of limestone was interpreted to drive $\delta^{26}\text{Mg}$ to lower values due to the less than 1.0000 fractionation factor associated with limestone diagenesis ($\alpha_{\text{diag}}^{\text{Mg}} = 0.9955$). Therefore, early diagenesis of a

microbialite, which includes the processes of carbonate dissolution and recrystallization (Planavsky et al., 2009), which might cause mass dependent Mg isotopic fractionations.

Goals of This Study

Storr's Lake, a hypersaline lake located on San Salvador Island, Bahamas, contains modern, fine-grained stromatolites, first described by Hattin (1982). Although a significant amount of data has been collected on these stromatolites, particularly in the western portion of the lake (e.g., Mann and Hoffman, 1984; McNeese, 1988; Neumann et al., 1989; Mann and Nelson, 1989; Pentecost, 1989; Zabielski, 1991; Dupraz et al., 2013; Paul et al., 2016), the mechanism of stromatolite formation at Storr's Lake is not well understood. The primary goal of this research is to investigate the organomineralization processes and lamination formation of stromatolitic knobs from Storr's Lake with the use of Mg isotopes. The hypothesis is that the Mg isotopic composition of a stromatolitic knobs will be dominated by both biological effects and mineralogical controls. Because stromatolitic knobs precipitate carbonate minerals from the lake water, it is highly possible that the Mg isotopic compositions of sublayers from stromatolitic knobs will inherit the isotopic features of the surrounding lake water from which the stromatolite forms. In addition, because previous work has shown a difference in Mg isotopic values between aragonite and high-Mg calcite, Mg isotopic compositions of microbialite sublayers will also be controlled by the percent ratio of aragonite over high-Mg calcite, suggesting that a transformation from aragonite to calcite (possible during early diagenetic processes) could alter the primary Mg isotopic values of microbialitic carbonates. Therefore, the Mg isotope budget of the current lake system and the mineralogy of stromatolitic knobs should be explored and evaluated to constrain the controls on the Mg isotopic composition of the stromatolitic knobs.

In this study, new results are presented of investigations on the hydrochemistry of Storr's Lake including in situ water chemistry data, major elemental composition, and saturation state to constrain the source and spatial homogeneity of the lake water. High-precision elemental analysis was also conducted on the sublayers of a plateau-mushroom stromatolite and a pinnacle-mound stromatolite collected from the lake in January 2016. X-ray diffraction (XRD) analysis was coupled with thin section observation to determine the mineralogy of the sublayers from the two stromatolites and to characterize the spatial distribution of varied carbonate minerals at the meso-structure scale. Additionally, carbon, oxygen, and magnesium isotopic compositions ($\delta^{13}\mathrm{C}$, $\delta^{18}\mathrm{O}$, $\delta^{24}\mathrm{Mg}$) of the same sublayers were investigated to gain insight into the mechanism of organomineralization and laminae formation.

Additional goals of this study are to evaluate the importance of environmental conditions and microbial metabolic activities on the mineralogic variations between sublayers of the stromatolites investigated, to determine the mechanisms for laminae formation (organomineralization) and the associated biogeochemical processes, and to compare Storr's Lake stromatolites with other closed-system and open marine stromatolites in order to create a model of stromatolite formation that may influence future studies of fossil stromatolites.

Chapter 2

Geological Setting and Previous Studies of Storr's Lake

Geographic and Geologic Setting of San Salvador Island, Bahamas

The Bahama Archipelago contains many hypersaline lakes, and is an ideal setting to study stromatolite formation. The ~1400 km long archipelago is located to the southeast of the North American continental margin, and consists of 700 islands and 2,500 smaller islets and cays (Figure 2-1A; Curran and White, 1995; Curran, 1997). These islands are surrounded by shallow-water banks or platforms above thick sequences of carbonate rock (Curran, 1997). The Bahamas Platform is comprised of Pleistocene limestone overlying Tertiary and Cretaceous limestone (Bathurst, 1975). The plateau is submerged to an average depth of >7 to 10 m, and is covered with recent carbonate sediment deposits (Bathurst, 1975). The platform drops steeply at the edge to a depth of 200 m at a distance of 2 km or less (Bathurst, 1975). Most of the platform's islands consist of a sequence of subtidal, intertidal, and eolian carbonate rocks from the late Pleistocene and Holocene Epochs (Curran and White, 1995). The Pleistocene and Holocene units are separated by a disconformity that is marked by karst and soil features, including terra rossa paleosols, and caliche crusts (Curran and White, 1995). The banks of the platform are tectonically stable. Some isostatic subsidence does occur, but has been at equilibrium with carbonate sedimentation since the Early Jurassic (Mullins and Lynts, 1977; Curran, 1997). The development of sedimentary facies is mainly controlled by a gradual, eustatic sea level rise (Curran and White, 1995).

San Salvador Island, the field location of this study, is the easternmost island on the Bahamas Platform (Figure 2-1A and 2-1B). It is located on a small, isolated bank at the eastern edge of the Bahamas (Curran, 1997). The island is ~11 km wide by 21 km long, and is surrounded by a narrow platform with a steep, abrupt shelf-edge break on its

eastern side (Curran, 1997). This drop-off occurs at 36 to 185 m and breaks into a steep continental slope to about 4700 m (Adams, 1983). The western edge of the platform does not have a steep drop-off, and is submerged to a depth of about 15 to 20 m (Adams, 1983). Successive stages of carbonate eolian accretion are represented by arcuate ridges along the island (Curran, 1997). The shorelines of San Salvador Island are comprised of eroded eolianite headlands, beaches of fine- to medium- grained skeletal carbonate sand, and Holocene beachrock (Curran, 1997). San Salvador displays the same shallowing upward sequences that are recognized throughout the Bahamas (Curran, 1997).

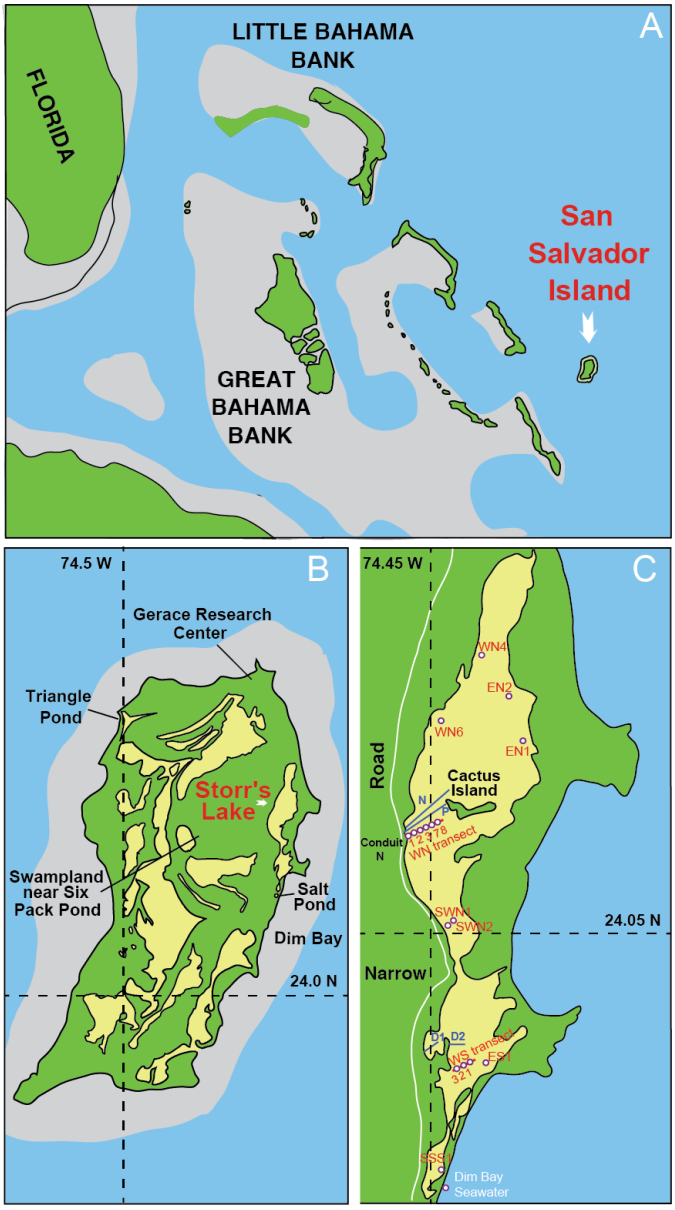

Figure 2-1 Location map of (A) The Bahamas, (B) San Salvador Island with the location of Storr's Lake, and (C) sampling locations and transects (labeled in red) of Storr's Lake for this study. Transect N, P, D1, and D2 were published in Neumann et al. (1989), Paul et al. (2016), and Dupraz et al. (2013), respectively.

Geographic and Geologic Setting of Storr's Lake

Storr's Lake is a hypersaline lake located on the northeastern, windward coast of San Salvador Island, which is also home to several other hypersaline lakes as well. The lake is located between the Queen's Highway to the west and Green Bay to the east (Fowler, 2011).

Storr's Lake is comprised of a large northern sector and a smaller, shallower southern sector, with a small zone called "the narrows" separating the two (Figure 2-1C; Zabielski, 1991). The lake once comprised three distinct depositional basins separated by two bedrock sills running east to west. The three basins were open to the ocean 4,300 ±70 years ago, but were subsequently closed off from the ocean by the southern progradation of a spit running north-south (Zabielski, 1991). The northern basin was closed off first 3,100 ±70 years ago, followed by the central and southern basins (Zabielski, 1991). The three basins became one lake after being flooded during continued Holocene sea-level rise (Zabielski, 1991). After being closed off, evaporation led to a concentration of the salt in the seawater that filled the lake, causing the lake to become hypersaline (Zabielski, 1991).

Being a fairly shallow lake, Storr's Lake only reaches a maximum depth of two meters, and water levels fluctuate throughout the year (around 25 cm variations; Mann and Nelson, 1989). During the dry season (December-April), evaporation reduces the water level, which recovers during the wet season (May-November) as the result of increased rainfall and groundwater recharge (Mann and Nelson, 1989). Although some tidal influx and outflow of seawater does occur through five known conduits at the northernmost end of the lake and through a small seep in a barrier dune at the southeast margin, these effects are negligible, and daily tidal fluctuation of lake water levels has never been observed (Mann and Nelson, 1989).

Storr's Lake is hypersaline and density-stratified, but salinity levels fluctuate dramatically in response to water level. During dry periods, the salinity of the lake can increase to as high as 93.5 PSU as salt is concentrated due to evaporation, and salinity will decrease again to as low as 38 PSU as the salt is diluted by recharge and rainfall during wet periods (Mann and Nelson, 1989).

Morphological type and distribution of microbialites

Several types of microbialites have been identified in the northern section of Storr's Lake (Neumann et al., 1989; Paul et al., 2016) (Figure 2-2). With increasing water depth, the frequency of lithified microbialites increases. Neumann (1989) classified the morphologies as bulbous crusts, mushroom-shaped heads, and club-shaped heads. However, Paul et al. (2016) suggested a more detailed classification, which includes calcareous knobs (Figure 2-3A), plateau-mushroom (Figure 2-3B), pinnacle mound (Figure 2-3C), cauliflower-top mushroom (Figure 2-3D), and multi-cuspate (Figure 2-3E), based on a representative transect from the Western Shore to the Cactus Island.

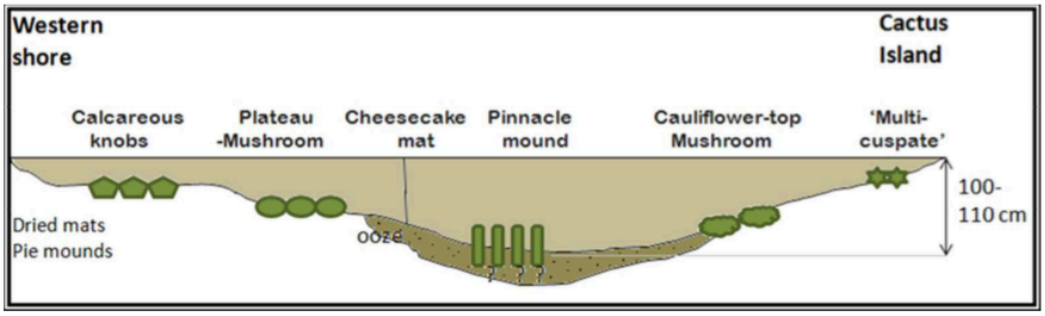

Figure 2-2 Overview of the distribution of the types of microbialites in the northern sector of Storr's Lake. Figure from Paul et al. (2016).

In the shallowest parts of the lake (Figure 2-2), the calcareous knobs or bulbous crust exhibits two distinct parts: (i) a lower, darker-colored, fused-granular, carbonate structure and (ii) an upper, lighter-colored, carbonate structure that has a smoother,

continuous carbonate buildup compared to the granular bottom portion. The next deepest forms, the cauliflower-top mushroom and plateau-mushroom, have the same overall external morphological appearance but vary in certain characteristics. The top surface of cauliflower-top mushroom consists of bulging carbonate knobs, whereas the top crust of plateau-mushroom has a reticulated structure (Paul et al., 2016). Moreover, the cauliflower-top mushroom has carbonate laminations at the bottom and plateau-mushroom lacks any horizontally stratified layers (Paul et al., 2016). In the deepest parts of the lake, pinnacle mounds can be found. The upper-most surficial crust of the pinnacle mound is a continuous layer, which is replaced below by a thrombolitic morphology (Paul et al., 2016). The multi-cuspate type near the shore of Cactus Island has more distinguished protrusions, sharper edges with well lithified structures and does not crumble easily (Paul et al., 2016).

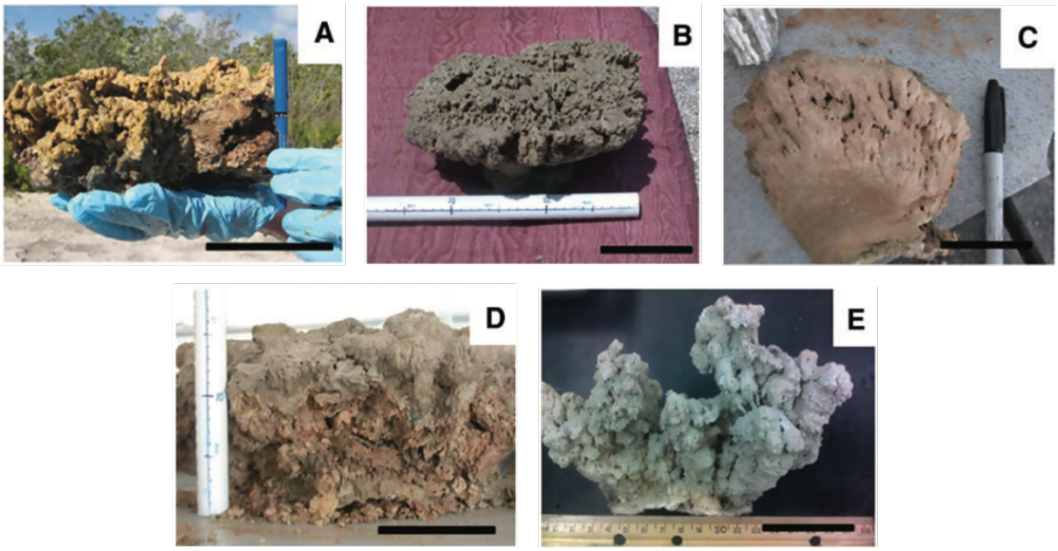

Figure 2-3 Microbialite samples and microbial mats collected from Storr's Lake. (A) Calcareous knobs; (B) Plateau-mushroom; (C) Pinnacle mound; (D) Cauliflower-top mushroom; (E) Multi-cuspate. Adapted from Paul et al. (2016).

Mineralogy

The mineralogy of the microbialite in Storr's Lake as determined by X-ray diffraction (XRD) analysis by Dupraz et al. (2013) was relatively constant, revealing high-Mg calcite with 12 to 17 mol% Mg^{2+} substituting for Ca^{2+}. Low-Mg calcite and pure calcite were not found. Further study by Paul et al. (2016) found a considerable amount of aragonite in a pinnacle mound and plateau-mushroom microbialite (Figure 2-4). It was also observed that the mol % Mg in the carbonate minerals of the pinnacle mound-type microbialite initially decreased from the top to middle positions, but increased moving from the middle toward the bottom of the microbialite (Figure 2-4A).

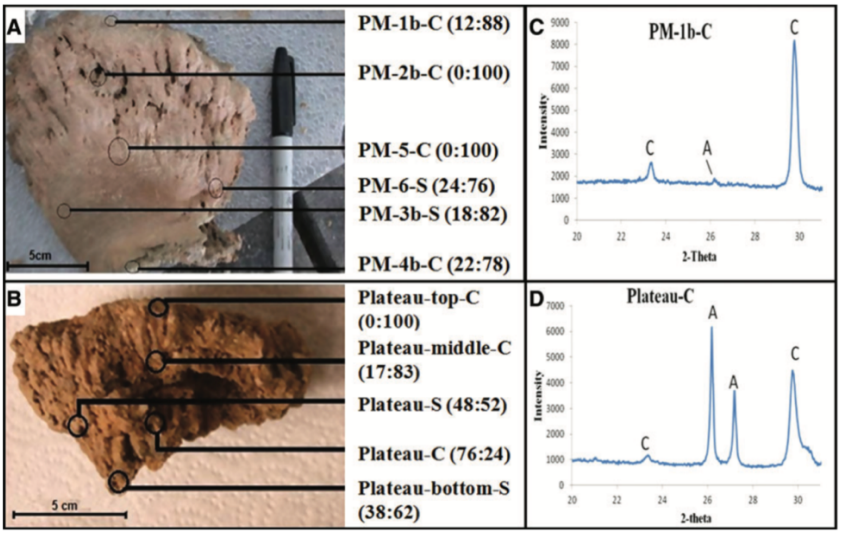

Figure 2-4. XRD analysis of microbialite samples of Storr's Lake: (A) Half-sectioned pinnacle mound (PM) and (B) half-sectioned plateau-mushroom shaped microbialite. Figure from Paul et al. (2016). Samples were collected either in the center, C, or at surface, S. Numbers to the right of the sample locations in (A) and (B) correspond to the aragonite: calcite percent ratio as determined by XRD analysis. Examples of XRD pattern for two of the samples, PM-1b-C (C) and Plateau-C (D), show peaks for aragonite and calcite, shown by the letters A and C, respectively.

Microbial Activity and Stable Isotopes

Cultivation-independent microbial diversity analyses were performed on five different types of microbial mats (i.e., calcareous knob, plateau-mushroom, pinnacle mound, cauliflower-top mushroom shaped) isolated from Storr's Lake (Paul et al., 2016). Dendrogram and major bacterial taxa are shown in Figure 2-5, respectively. The mat on the shallow-water calcareous knob was most similar to the plateau-mushroom microbial mat in terms of microbial population. Furthermore, the two mats clustered closest with the cheesecake microbial mat. The deep-water pinnacle mound microbialite grouped closely with the cauliflower-top mushroom microbialite, both of which are located at greater water depths and farther away from the western shore of the lake.

At least twelve dominant bacterial phyla were identified in five different microbial mat communities (Paul et al., 2016). Cyanobacteria were generally low in abundance and ranged from ~0.01% OTUs (operational taxonomic unit) in the deeper pinnacle mounds to ~3.2% OTUs in the shallow calcareous knobs (Paul et al., 2016). Other photosynthetic members included green non-sulfur bacteria of the phylum Chloroflexi and purple sulfur bacteria of the class Gammaproteobacteria (Paul et al., 2016). All mat types contained significant amounts of sulfate-reducing and dehalogenating bacteria (Paul et al., 2016).

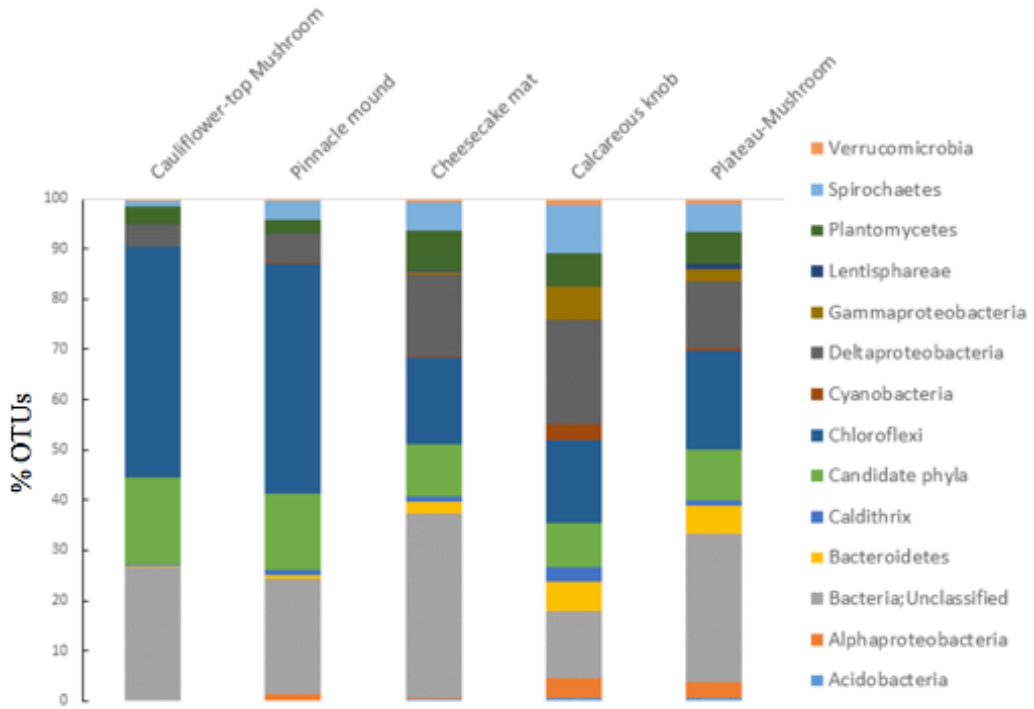

Figure 2-5. Dendrogram showing relative percentage abundance of major bacterial taxa detected in five Storr's Lake microbial mats (adapted from Paul et al., 2016).

Carbon isotope data of carbonate laminae from a Storr's Lake *Scytonema* knob (a type of stromatolitic knob with the dominant micro-organism of heterocystous filamentous cyanobacterium *Scytonema* sp.) showed a slighted enriched $\delta^{13}C$ signature in the upper photosynthetically active lamina (top 1-2mm) of the knob (Figure 2-6), but a shift to more negative values deeper within the knob (Dupraz et al., 2013). It was hypothesized that photosynthesis by cyanobacteria consumes lighter carbon at the surface, whereas the anaerobic respiration of SRB releases lighter carbon at deeper depth (Dupraz et al., 2013). The combination of the two processes can explain the carbon isotope signature observed in Dupraz et al. (2013).

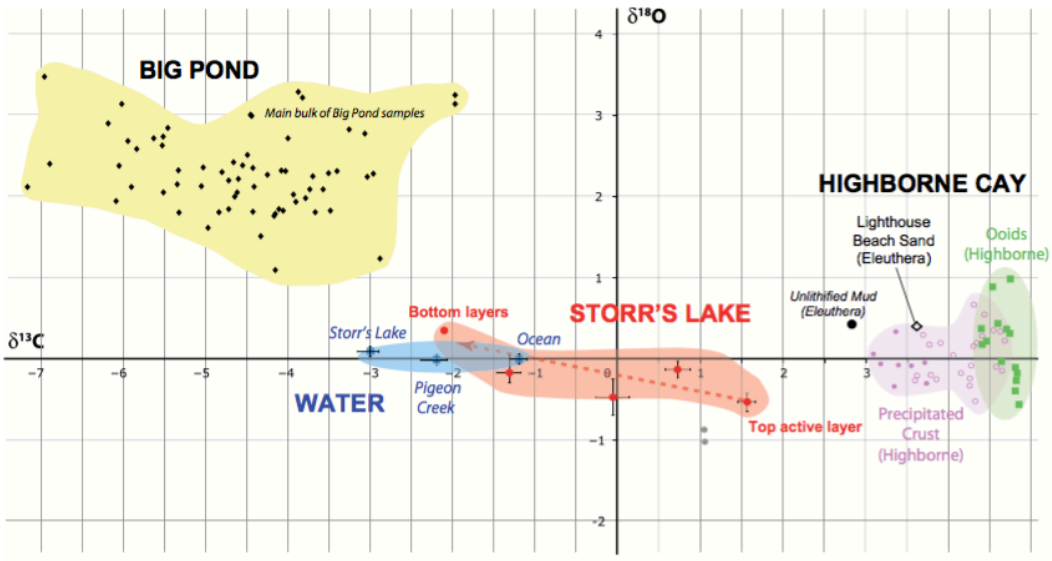

Figure 2-6 Carbon and oxygen isotopic composition of carbonate laminae from Storr's Lake. *Scytonema* knob in red and water in blue (from Dupraz et al. 2013), Big Pond microbialites (Eleuthera Island, Bahamas; data from Glunk et al. 2009), sediment collected on Eleuthera Island (Bahamas; Dupraz et al. 2013), and precipitated micritic crust and ooids from open marine stromatolites (Highborne Cay, Bahamas; data from Andres et al. 2006). Figure from Dupraz et al. (2013).

Chapter 3

Methodology

Water Chemistry Analysis

Sample Collection

Field work was conducted on San Salvador Island (SSI) (Figure 2-1B) from January 6th to 14th, 2016. Samples (water and stromatolitic knobs) were collected from Storr's Lake (Figure 2-1C). Water samples were also taken from Salt Pond, Triangle Pond, swampland near Six Pack Pond, a freshwater well at the Gerace Research Centre, and seawater from Dim Bay (Figure 2-1C). Water samples were filtered on site through disposable 0.45 µm cellulose acetate syringe filters into 60 ml acid-cleaned Nalgene LDPE bottles and kept in the dark and frozen most of the time until acidification back at The University of Texas at Arlington (UTA) in June 2016. Stromatolitic knobs were collected exclusively from Storr's Lake because they were not observed at any other sampling sites. Stromatolitic knobs were manually removed from the bottom of Storr's Lake. A portion of these samples has been stored in lake water of corresponding sample sites in a refrigerator at UTA, whereas larger samples were air dried for storage. Historic water samples (representative of summer 2012 and 2013) were provided for comparison by Dr. David Wronkiewicz at the Missouri University of Science and Technology and Dr. Varun Paul currently at Mississippi State University. These older samples were filtered at UTA prior to acidification and further analysis.

Field Measurements

Locations of sampling sites were recorded as GPS coordinates in NAD27 using a GARMIN eTrex® 10 and water depths were determined with a meter stick. Air temperature, humidity and wind speed were measured using a Kestrel 4500 Pocket Weather Tracker at each site.

Physical and chemical parameters of the water, including temperature, conductivity, and dissolved oxygen (DO) were measured in situ at each sampling site using a portable YSI Professional Plus multi-parameter probe. Calibration of the YSI pH probe using solutions of 3, 7, and 11 was unsuccessful in the lab, so the YSI was not used to measure pH in the field. Redox potential was also measured using the YSI multi-parameter probe for the first few days of field work, but it was determined that the measurements (extremely negative ORP) were questionable due to issues during calibration with the Zobell solution. These ORP values are not reported. The YSI multi-parameter probe was calibrated in the lab every morning of the sampling trip. Conductivity was calibrated with a 100,000 µS/cm standard (RICCA CAT# 2249-32). Dissolved oxygen (DO) was calibrated following a 1-point calibration method using water saturated air as a 100% standard. Duplicate measurements in the field reproduced values within 1% for water temperature in ºC, 2% for conductivity in mS/cm, and 13% for DO in mg/L.

The measurements of pH were performed using an Accumet AP 115. Duplicate samples reproduced a standard deviation of 0.01 for pH. A standard of pH 7 was measured in the field each day, typically multiple times, to correct in situ pH measurements of the water.

Alkalinity (measured as mg/L $CaCO_3$) and Ca and Mg hardness measurements were performed within 1 hour (on shore for alkalinity) to 6 hours (at the Gerace Research Centre for hardness) after sample collection following the colorimetric titration with a digital titrator HACH method 8203 and HACH method 8329 respectively. Alkalinity measurements were performed without sample dilution. For Ca and Mg hardness measurements, samples were diluted 1:100 with ultrapure water before testing. The ultrapure water was confirmed to not contribute to the hardness values. Duplicate

samples reproduced within 1 mg/L as $CaCO_3$ (SD; n = 2) and 14 mg/L as $CaCO_3$ (SD; n = 3) for alkalinity and Ca/Mg hardness, respectively.

The turbidity of water was measured near the field site on shore after sample collection with a HACH 2100Q Portable Turbidimeter. A standard of 100 NTU was also measured to correct the instrument after measurement of water samples. Triplicate measurements of one sample yielded 3 NTU (SD; n = 3). Data collected, along with instrumentation used, is reported in Table 3-1.

Table 3-1 Instrumentation for Field Measurements

FIELD METHODS – IN SITU MEASUREMENTS	
Parameter	Instrument
Coordinates	Garmin eTrex 10
Air temperature	Kestrel 4500 Pocket Weather Tracker
Humidity	Kestrel 4500 Pocket Weather Tracker
Wind speed	Kestrel 4500 Pocket Weather Tracker
Water temperature	YSI ProPlus Quatro
Water depth	Meter Stick
pH	Accumet AP 115
Dissolved oxygen	YSI ProPlus Quatro
Conductivity	YSI ProPlus Quatro
Turbidity	Hach 2100 Q
Alkalinity	Hach Digital Titrator
Ca and Mg Hardness	Hach Digital Titrator

Anions Analysis

Filtered water samples were collected for chloride (Cl^-) and sulfate (SO_4^{2-}) analyses. Samples were stored on ice in the dark in the lab at The University of Texas at Arlington (UTA) prior to analysis. Chloride and sulfate concentrations were determined using a Dionex ICS-2100 ion chromatography (IC) system by Dr. Lixin Jin at The University of Texas at El Paso. Hypersaline samples and seawater were diluted 1000x with ultra-pure water prior to analysis. External precisions for the IC method confirmed on

duplicate analyses (n=2) of a standard are 0.4% for Cl^- and 1.2% SO_4^{2-}. Duplicate measurements of two randomly chosen samples yielded relative standard deviation (RSD) values of 0.3% for Cl^- and 0.2% or less for SO_4^{2-}. Bicarbonate (HCO_3^-) was calculated from in situ alkalinity measured in the field.

Cations Analysis

The filtered water samples were acidified using trace metal grade nitric acid to preserve the dissolved metal ions. Hypersaline samples and seawater were diluted 100x to 500x in 2% trace metal grade nitric acid for cation analysis. Ca^{+2}, Mg^{+2}, Na^{+1}, K^{+1}, and Sr^{+2} concentrations were measured by a Shimadzu ICPE-9800 inductively coupled plasma optical emission spectrometer (ICP-OES) at the Shimadzu Center for Material Science and Environmental Forensics at UTA. Measurements were made at wavelengths 183.801 (Ca), 285.213 (Mg), 589.592 (Na), 766.490 (K) and 216.596 (Sr). Bulk, mixed standard solutions were prepared with certified ICP standard solutions and were used for calibration and for quality control checks during each run. Based on replicate analyses (n=3) of an intermediate concentration standard during the analytical run, the external precision for all cations is better than 2.5% (RSD). The internal precisions based on duplicate measurements of randomly chosen samples resulted in a range of RSD values of 2.9% to 3.7% for Ca; 5.1% to 9.4% for Mg; 0.5% to 6.0% for Na; 0.9% to 10.1% for K, and 3.6% to 7.2% for Sr.

Saturation Index and Ionic Strength Calculation

After ion analysis, water chemistry data from each sampling location were used to calculate saturation indices of potential minerals (calcite and aragonite) and ionic strength using the Geochemist's Workbench Student Edition (Bethke and Yeakel, 2016). Saturation indices (S.I.) are calculated as the log of the ratio of a mineral's ion activity product (IAP = the product of the activities of dissolved ions, i.e., $\{Ca^{2+}\}\times\{CO_3^{2-}\}$) to the

mineral's solubility product (K_{sp}), following the equation SI=log(IAP/K_{sp}) (Stumm and Morgan, 1996). The molar ionic strength, I, of a solution is a function of the concentration of all ions present in that solution (Green, 1993). The function is denoted as:

$$\mathrm{I} = \frac{1}{2}\sum_{i=1}^{n} c_i {z_i}^2 \quad (3\text{-}1)$$

with the coefficient one half is because both cations and anions are included, c_i is the molar concentration of ion i (M = mol/L), z_i is the charge number of that ion, and the sum is taken over all ions in the solution.

Stromatolite Sample Digestion and Elemental Analysis

Sample Digestion and Preparation

Seventeen surface and sublayer samples of field or lab sectioned stromatolite samples WS1 and WN7 were carefully hand-picked, with the material being collected within individual layered features of the bioherms. All samples were gently hand crushed to a powder by using an agate mortar and pestle, rinsed three times with ultrapure water to remove soluble salts and low density organic particles, and then dried in an oven at 55°C overnight.

Around 6 mg of each rinsed powdered sample was weighted into 7 ml acid cleaned Teflon vials. Then the samples were dissolved in 1 mL 2N Teflon distilled HCl, after which the vials were capped and sonicated for 30 min and dried on a hot plate at 90°C. Approximately 1 ml of 30% H_2O_2 was added to the sample vial containing the dried residue, after which the vials were capped, sonicated for 5 min, and placed on a hot plate at 90°C for 30 min. The vials were then uncapped and the samples were allowed to evaporate to dryness. The process was repeated a second time to ensure the removal of organic carbon, after which the samples were dissolved in 3 ml of 2% Teflon distilled HNO_3. One third of the dissolved sample was removed from the vials to acid-washed

tubes for elemental analysis, the remainder was used for Mg isotope analysis. A complete procedural blank was prepared as well.

Elemental Analysis of Stromatolite Samples

The dissolved stromatolite samples were further prepared for elemental analysis by dilution with 4 ml of 2% Teflon distilled HNO_3 to form 5 ml of solution required for analysis. Bulk mixed standards and blanks were prepared in the same acid using certified plasma standard solutions. The Shimadzu Inductively Coupled Plasma Atomic Emission Spectrometer (ICPE-9800) in the Shimadzu Center for Environmental Forensics and Material Science at UTA was used to measure the concentrations of Ca, Mg, Sr, and Na in all samples. Measurements were made at wavelengths of 183.801 (Ca), 216.596 (Sr), 285.213 (Mg), and 589.592 (Na). The procedural blanks were < 0.75 µg for Ca, < 0.09 µg for Mg, < 0.15 µg for Na, and < 0.009 µg for Sr, which represented < 0.09% of Ca, < 0.27% of Mg, < 1.47% of Na, and < 0.05% of Sr in the total dissolved samples. Based on replicate analyses (n=3) of an intermediate concentration standard during the analytical run for samples from WS1 the external precision for all cations is better than 2.0% (RSD). The internal precisions of the ICP-OES on the measured Ca, Mg, Sr, and Na concentrations based on three repeat measurements of the sample solution during a single analytical run are better than 0.94‰ (RSD), 2.65% (RSD), 1.02% (RSD), and 2.83% (RSD), respectively.

X-ray Diffraction (XRD) Analysis

Seventeen surface and sublayer samples of stromatolite samples WS1 and WN7 were analyzed for their mineralogical composition by using XRD analysis. The rinsed and dried powered samples were press-mounted into sample holder disks and scanned between 3 to 65° two-theta at a scan rate of 2° (2-theta) per minute using a MAXima X XRD-7000 X-Ray Diffractometer with a CuKα radiation source and a rotation sample

stage in the Shimadzu Center for Environmental Forensics and Material Science at UTA. The software program used in the operation of the instrument is MDI Jade 9, which allowed for a semi-quantitative comparison of the relative percentages among the minerals identified. The software automatically calculates the area of the peaks observed for the high-Mg calcite and aragonite and correlates the area to calculate the relative percentages.

Carbon and Oxygen Isotope Analysis

The stable isotopic composition of carbon (C) and oxygen (O) were determined on the carbonate fraction of surface and sublayer samples of stromatolitic knobs WS1 and WN7 in the Light Stable Isotope Laboratory at UTA. Approximately 300 µg of homogenized powdered samples and both in-house standard (UHTA) and international standards (NBS 19 and NBS 18) were loaded into acid-cleaned serum-top reaction bottles, and their weights were documented. Reaction bottles were flushed with ultra-high purity helium for 10 min and then were injected with ultra-pure 100% phosphoric acid (H_3PO_4) at 75 °C to produce CO_2. Headspace was analyzed for $\delta^{13}C$ and $\delta^{18}O$ of the evolved CO_2 at standardized equilibration times using a Thermo Gas Bench II connected to a Finnegan Delta V Advantage isotope ratio mass spectrometer. Delta values were calibrated to NIST calcium carbonate reference material NBS 18 and 19 and are reported relative to VPDB. The standard deviations of both C and O isotope values, based on repeated analysis of in-house standards, are less than 0.15‰.

Magnesium Isotope Analysis

Separation of Mg from the sample matrix was achieved by a two-step cation exchange chromatography in a clean lab. The first PFA column (installed with a 4.0 mm PTFE frit, 30 micron) was loaded with ~2.3 ml of Bio-Rad 200–400 mesh AG® 50W-X8 pre-cleaned resin (rinsed with > 9 times column volume of 8N ultrapure HCl and 18.2 MΩ

Milli-Q® ultrapure water). This resin was further cleaned with > 9 times column volume of 1 N HNO_3 and Milli-Q® water. Samples containing ~20 µg of Mg were loaded onto the columns. Magnesium was eluted through this first column with 1N teflon distilled HNO_3. Because Mg isotopes can be significantly fractionated during ion exchange reactions on the columns it is essential to obtain ~100% Mg yield from the column chemistry. To assure close to 100% Mg yield, the position of the Mg cut was determined using both a pure Mg standard solution and a seawater sample. Magnesium elution curves were not noticeably shifted for these two different matrix compositions and Mg was eluted completely through the columns with 15 ml of 1 N HNO_3 (Figure 3-1; Appendix D). This column procedure was conducted one time for each sample to obtain a pure Mg solution. Each sample was checked for recovery of Mg using ICP-OES. It was found that Ca was collected within the Mg cut for some samples with high Ca/Mg molar ratios some Ca was collected within the Mg cut. These samples were further purified using a second PFA column prior to Mg isotope analysis. The second PFA column (installed with two 1.57 mm thick porous UHMW Polyethylene frits, 70 micron) was loaded with ~0.6 ml of pre-cleaned Mitsubishi 75-100 mesh MCI Gel-CK08P cation exchange resin. The resin was eluted with 3.575 ml of 1.8 N HCl, leading to complete separation of Mg from Ca (Figure 3-2). The whole procedural blank was less than 32 ng (representing <0.16% of loaded Mg), which is insignificant relative to the amount of Mg loaded on the column.

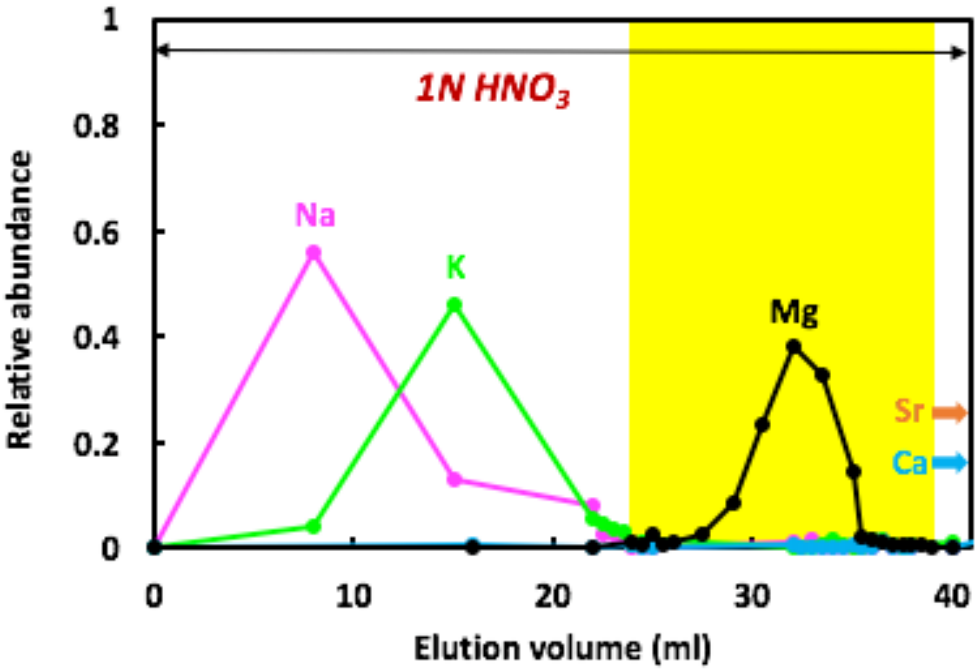

Figure 3-1 Elution curves of Mg and matrix elements for a seawater sample on a 15 mL column (4.0 mm inside diameter × 6.3 mm outside diameter × 20 cm capillary). The Mg purification procedure is conducted with cation exchange resin AG® 50W-X8 and 1N distilled HNO3. The shaded yellow interval is the Mg cut collected for isotopic analysis.

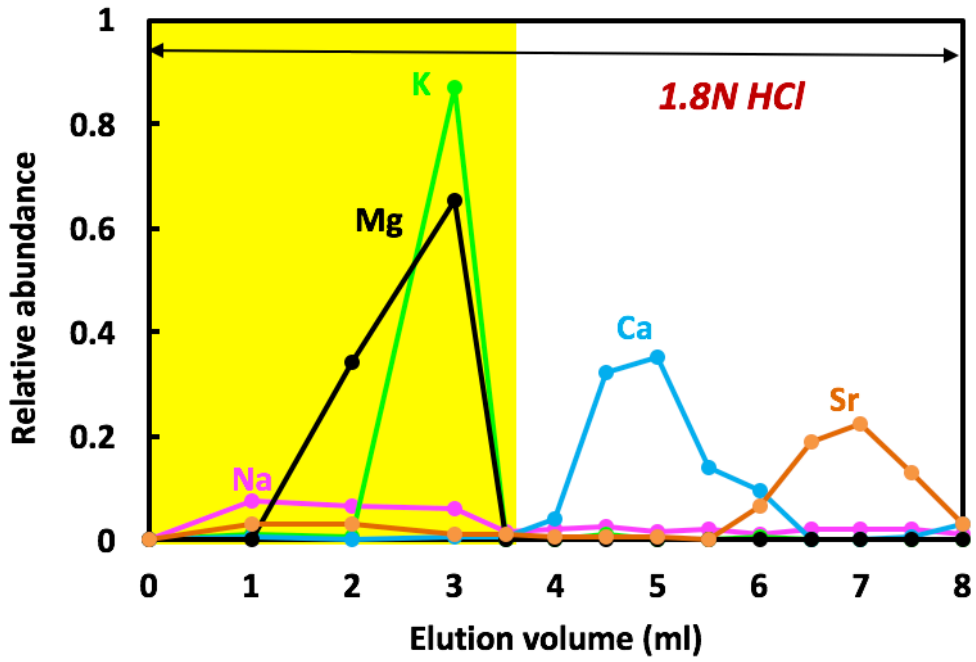

Figure 3-2 Elution curves of Mg and matrix elements for a seawater sample passed through a 6 mL column (2.4 mm inside diameter × 4.0 mm outside diameter × 15 cm capillary). The Mg purification procedure is conducted with MCI Gel-CK08P resin and 1.8N distilled HCl. The yellow shaded interval is the Mg cut collected for isotopic analysis.

Water and carbonate samples processed through column chemistry were transported and measured with a multi-collector inductively coupled plasma mass spectrometer (Thermo Fisher Neptune Plus MC-ICP-MS) at Penn State's Metal Isotope Laboratory (MIL). Following column chemistry, purified samples were resuspended and diluted in 0.3 N (2%) teflon distilled HNO_3 to a Mg^{2+} concentration of 200 ppb, and introduced to the MC-ICP-MS as a dry aerosol using a Cetac Aridus II desolvating system with a 100 µL/min C-flow PFA nebulizer (RF power 1200 W). When optimized, the Aridus technique effectively removes solvent-derived polyatomic interferences (e.g., $^{12}C^{12}C^{+}$, $^{12}C^{14}N^{+}$, and $^{12}C^{13}CH^{+}$) while maintaining a stable signal. A Ni Spectron jet sampler cone and a Ni Spectron skimmer cone were used, resulting in a 7-10 V ^{24}Mg ion

beam. Measurements were made in medium mass resolution, and ion beams at masses 24 ($^{24}Mg^{+}$), 25 ($^{25}Mg^{+}$), and 26 ($^{26}Mg^{+}$) were monitored on the L3, C, and H3 Faraday cups, respectively. Typical background intensities at masses 24 and 26 measured in the wash solution of 2% HNO_3, were <22 mV and <3 mV, respectively.

Isotope ratios were collected in a single 35 cycle block, with an 8 s integration time and a 5 s idle time. Each measurement was conducted with a 2.5 min take up time for the samples and a 5 min wash in clean 2% HNO_3. Magnet stability was assessed by the relative standard deviation of each 35 cycle run. Samples were measured in duplicate, with each sample analysis bracketed by measurements of pure Mg DSM3 standard solution. The in-run precision on the $^{26}Mg/^{24}Mg$ ratio for a single measurement run of one block of 35 cycles is < ± 0.08‰ (2SD). The internal precision on the measured $^{26}Mg/^{24}Mg$ ratio based on ≥2 repeat runs of same sample solution during a single analytical session is ± 0.20‰ (2SD). The external precision on the $\delta^{26}Mg$, based on repeated analyses of a sample (including multiple full procedural replicates) performed over the course of this investigation is ≤ ± 0.07‰ (2SD).

The alignment of the leading edges of the various Mg-specific ion beams was assessed during the warm-up and tuning period utilizing a pure Mg DSM3 standard solution. The ideal plateau mass was adjusted prior to measurement to ensure that each analytical session was conducted under relatively stable signals.

After March analyses of Mg isotopic compositions at Penn State, a new column procedure was used to eliminate a potential Si effect on Mg isotope analysis, which might be ascribed to the lack of in-column resin cleaning with hydrofluoric acid in the old column method. The new column method was developed based on the column procedures in Wombacher et al. (2009).

Mg purification for seawater-like samples (with high Mg and low Ca) was achieved by a single step of cation exchange chromatography, while a two-step cation exchange chromatography was essential for the separation of Mg from matrix in carbonate samples (with high Ca and low Mg). For both chemical separation steps, 1 ml Bio-Rad 200–400 mesh AG® 50W-X8 cation exchange resin was used. The resin was cleaned prior to loading in the columns; the same as the old column method. The ion-exchange columns were made of LDPE pasteur pipettes (AlphaLaboratories LW4691) with an inner diameter of 5.3 mm. The pasteur pipettes were cut on the top and bottom to create the column and allow for a resin bed height of 50 mm. To hold the resin in place 1.57 mm thick porous UHMW polyethylene discs (70 mm pore size) were punched out, and forced into the bottom of the columns. Liquid flow through the resin bed was driven by gravity only, with about 1 ml eluting in 9 min. Sub-boiling Teflon distilled HCl and ultrapure HF were used in the column procedures.

The first column procedure (for carbonate samples only) was used to separate Mg and matrix from Ca (Appendix E). After loading the resin in the columns, the resin was first cleaned with 3 ml 0.5N HF and 3 ml Milli-Q H_2O alternating three times, and then cleaned with 3 ml 10N HCl and 3 ml Milli-Q H_2O afterwards, and finally conditioned with 2 ml 10N HCl. The resin level was adjusted to the joint of the reservior and the capillary after the cleaning steps on the column. Samples containing ~20 µg of Mg (dissolved in 250 µl 10N HCl) were loaded onto the columns. Magnesium elution curves with two doped solutions (Ca/Mg molar ratio of 8 and 100 to simulate high-Mg calcite and aragonite, respectively) and a seawater sample were created (Figure 3-3). Magnesium and matrix were eluted through the first column procedure with 2.5 ml 10N HCl. One third of the collected samples were checked for Mg recovery using ICP-OES, and the rest (two thirds) of the samples were further purified using the second column procedure

(Appendix E). After cleaning the resin in the columns (the same as the first column procedure), the resin was conditioned with 3 ml 0.4N HCl and loaded with samples containing ~20 or 14 µg of Mg (20 µg for water samples and 14 µg for carbonate samples). The calibration experiment with a seawater sample (Figure 3-4) resulted in complete separation of Mg after rinsing the loaded column with 28 ml of 0.4N HCl followed by 1 ml of 1N HCl and collecting the next 13 ml of 1N HCl. The whole procedural blank was less than 50 ng (representing <0.25% of loaded Mg).

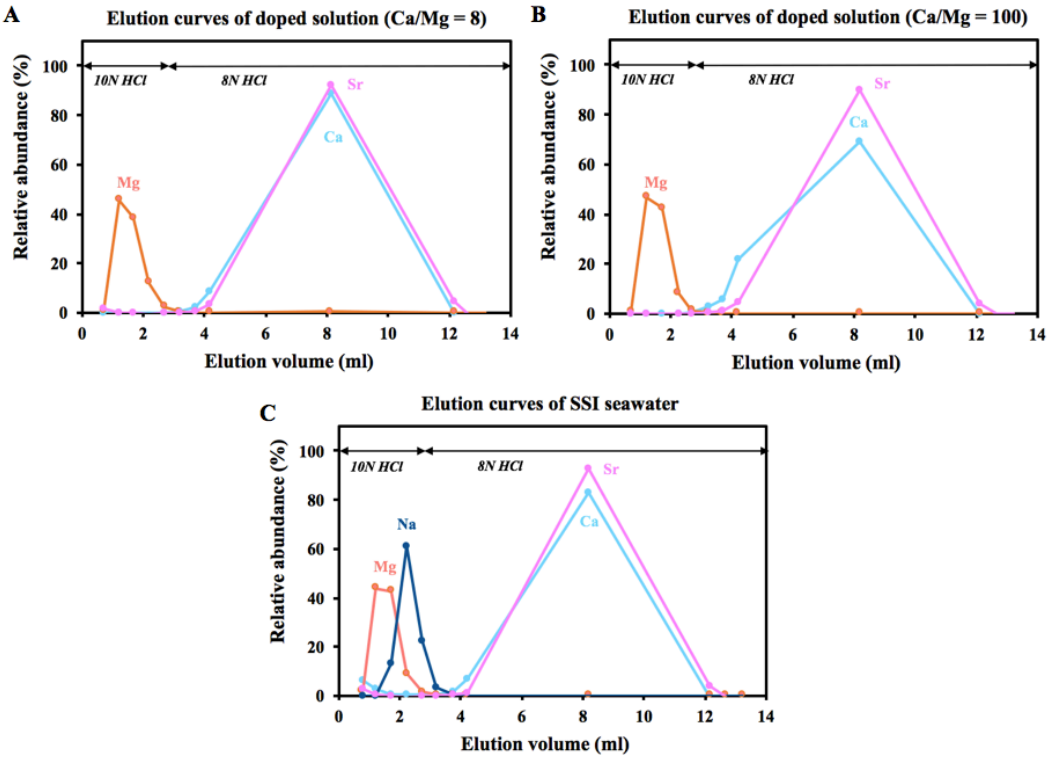

Figure 3-3 Elution curves of Mg and matrix elements for (A) a doped solution with Ca/Mg molar ratio of 8, (B) a doped solution with Ca/Mg molar ratio of 100, and (C) a seawater sample for the first step column chromatography. “SSI” represents San Salvador Island.

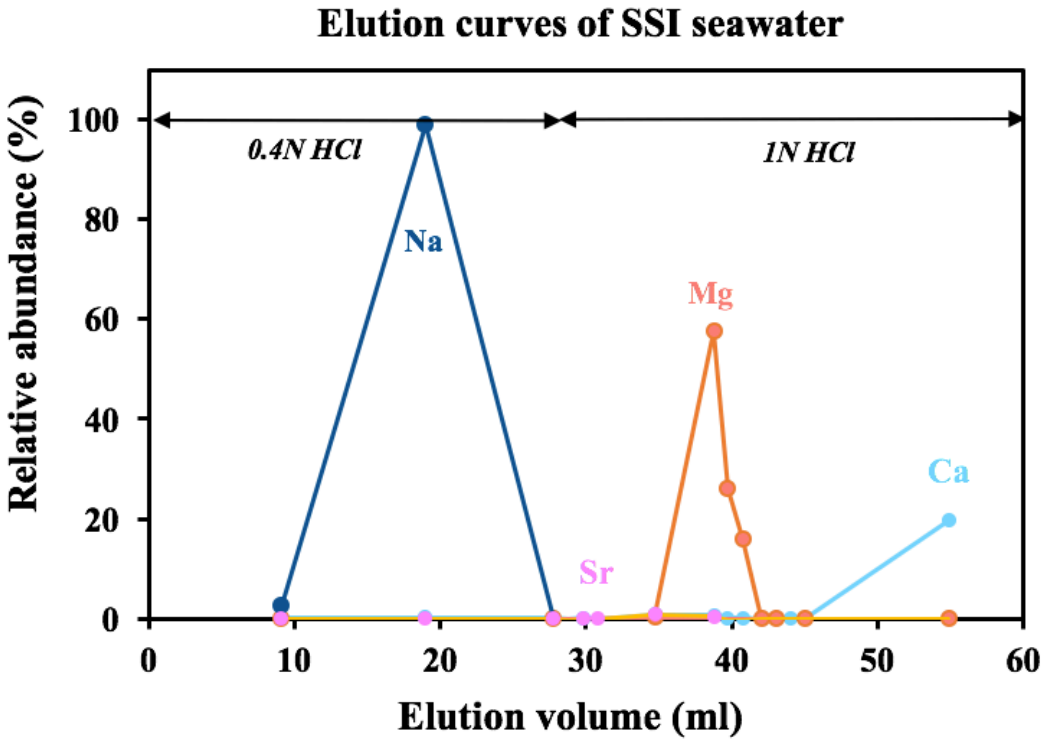

Figure 3-4 Elution curves of Mg and matrix elements for a seawater sample for the second column chromatography. “SSI” represents San Salvador Island.

The water and carbonate samples prepaired with the new column method were analyzed for their Mg isotopic compositions on the MC-ICP-MS at Penn State’s Metal Isotope Laboratory (MIL) in June using the Apex desolvating system which is different from the Cetac Aridus II desolvating system used in the March analyses. All other settings on the MC-ICPMS were the same between the March and June analyses.

Instrumental mass bias is corrected using a sample-standard bracketing approach. Additionally, the measurement of multiple in-house standards (CAM-1, SRM-3131a, and Fang-Zhen Teng’s laboratory standard, FZT-Mg) in each analytical session were used to assess analytical accuracy. On the MIL Neptune Plus MC-ICPMS, CAM-1 yielded δ^{26}Mg = -2.54 ± 0.10‰ (2σ, n = 27), SRM-3131a yielded δ^{26}Mg = -3.02 ± 0.12‰

(2σ, n = 25), FZT-Mg yielded δ^{26}Mg = -2.26 ± 0.16‰ (2σ, n = 29), and NIST980 yielded δ^{26}Mg = -4.22 ± 0.07‰ (2σ, n = 5). CAM-1 has an accepted δ^{26}Mg value of -2.58 ± 0.14‰ (Galy et al., 2003). FZT-Mg has a δ^{26}Mg value of -2.28 ± 0.03‰ (Jacobson et al., 2010).

Chapter 4

Results

Water Chemistry

Water chemistry was measured throughout Storr's Lake at different depths and locations. The total water depth (from the top of the microbialite head to the water surface) of the sampling locations ranged from 40 cm to 120 cm. Table 4-1 provides the average values for the parameters measured in the lake in January 2016. Water parameters were reported as average values ± standard deviation of diversity. The detailed water chemistry of each sample and location is provided in the Appendices A and B.

For most water parameters, the values of the northern and southern sectors of the Storr's Lake were not significantly different. The average (± SD) pH (north: 8.42 ± 0.09; south: 8.40 ± 0.05), conductivity (north: 56.32 ± 1.27 mS/cm; south: 56.12 ± 1.67 mS/cm), and salinity (north: 36.66 ± 0.51 PSU; south: 36.64 ± 1.03 PSU) of the northern and southern sectors were the same. The ocean water collected from nearby Dim Bay had a conductivity reading of 45.90 mS/cm equal to a salinity value of 29.02 PSU.

The average calcium hardness in northern sector was 1397 ± 62 mg/L as $CaCO_3$, and that of magnesium was 7322 ± 218 mg/L as $MgCO_3$, and the southern sector had similar average calcium hardness (1361 ± 30 mg/L as $CaCO_3$) and average magnesium hardness (7403 ± 186 mg/L as $MgCO_3$). The average (± SD) Ca and Mg concentrations of the two sectors were also very similar (13.40 ± 0.18 mg/L and 60.38 ± 0.99 mg/ L for north; 13.61 ± 0.17 mg/L and 61.78 ± 1.87 mg/ L for south). The two sectors had similar Mg/Ca molar ratios (4.52 ± 0.07 for northern sector and 4.54 ± 0.09 for southern sector) and identical Sr/Ca molar ratios (0.012). The northern sector had a slightly lower total alkalinity (121 ± 17 mg/L) value when compared to that of the southern sector (142 ± 11 mg/L). The average (± SD) turbidity of the two sectors were very similar, but the northern

sector (123 ± 42 NTU) displayed much more variability than the southern sector (98 ± 6 NTU).

Depth profiles at four locations (north: WN3, WN4, and SWN1; south: WS1; Figure 2-1) were systematically studied to observe the variations of the water parameters with water depth (Appendix A). Dissolved oxygen consistently showed a decreasing trend from the shallow to deeper water levels at each location (Figure 4-1A). The average dissolved oxygen decreased from 7.04 ± 1.08 mg/L at 0~25 cm to 6.51 ± 1.04 mg/L at 25~50 cm, 5.88 ± 1.59 mg/L at 50~75 cm, 5.08 ± 1.79 mg/L at 75~100 cm, and 2.97 ± 2.05 mg/L at >100 cm. The decrease of water temperature correlated with the increase of water depth at three locations (WN4, SWN1, and WS1; Figure 4-1B). At WN3, the water temperature displayed a decreasing trend with water depth from 5 cm to 80 cm and an increasing trend from 80 cm to 116 cm (Figure 4-1B). Although conductivity decreased with water depth at most locations (WN4, SWN1, and top 60cm of WN3), WS1 did not show this trend and WN3 increased conductivity deeper than 60cm (Figure 4-1C). For WN3, WS1, and SWN1 depth profile, pH generally decreases with water depth, however this trend is not observed in the WN4profile (Figure 4-1D).

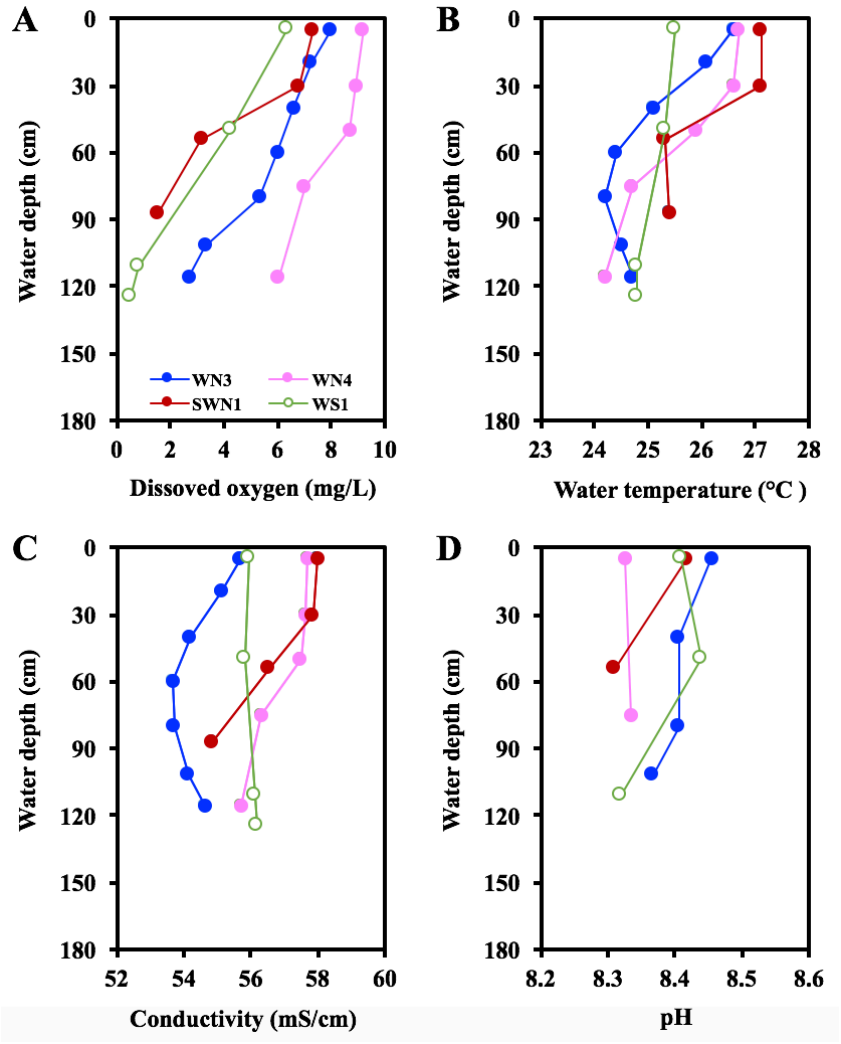

Figure 4-1 Variations of the (A) dissolved oxygen, (B) water temperature, (C) conductivity, and (D) pH with water depth at sampling locations of WN3, WN4, SWN1, and WS1 in Storr's Lake. The lack of measuring pH values at some water depths results in the missing data points in (D).

The swampy area where the conduit on the west side of the lake was sampled from a nearby depression and swamp is separated from Storr's Lake by a roadway (Figure 2-1C). There was a distinct delineation seen in the lake, where the brownish

conduit water mixed with the more turbid and hypersaline lake water. The average (± SD) conductivity of the conduit water was 3.34 ± 1.11 mS/cm with a pH of 7.96 ± 0.17. The average (± SD) calcium, magnesium, potassium, and sodium concentrations of the conduit water were 2.03 ± 0.07, 2.10 ± 0.05, 0.65 ± 0.34, and 19.3 ± 0.4 mg/L, respectively.

Proceeding from the lake shore to the more distant locations, the pH, conductivity, water temperature, and dissolved oxygen values showed a distinct transverse distribution in the near-surface water collected from the top several centimeters of water at these locations. For example, along the WN transect (Figure 4-2A and 4-2B) from west to east pH becomes higher (8.41 to 8.53) and conductivity shows a generally increasing pattern (54.4 to 56.8) traversing from the western shore to the Cactus Island. Both water temperature and dissolved oxygen increase lakeward first (starting from WN1 to WN2 and to WN3) and then decrease from WN3 to WN8 (the furthest from the shore; Figure 4-2C and 4-2D).

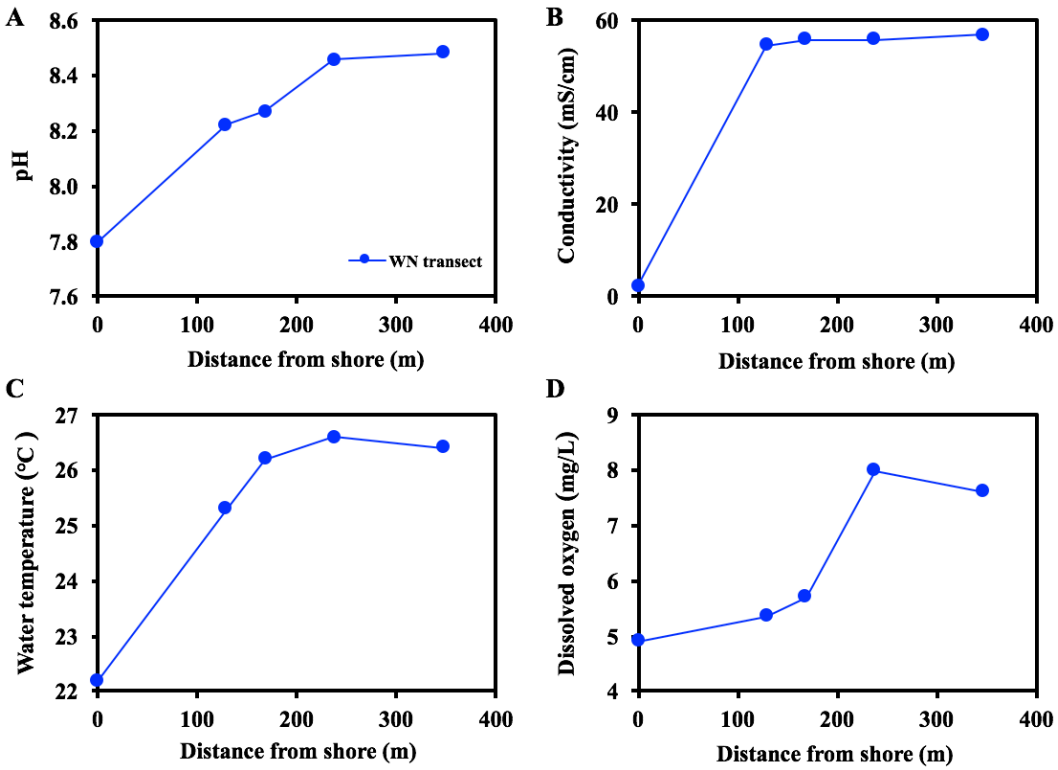

Figure 4-2 Variations of the (A) pH, (B) conductivity, (C) water temperature, and (D) dissolved oxygen with the distance from shore at WN transect (from the western shore to Cactus Island) in Storr's Lake. All the data were measured at a water depth of 5 cm. The five measuring points are conduit-N, WN1, WN2, WN3, and WN8 in an order of increasing distance from shore.

The calculated saturation index (SI) indicates whether or not a water is supersaturated with respect to aragonite and/or calcite (SI > 0). For aragonite, the SI values of northern and southern sectors averaged 0.75 and 0.81, respectively. The corresponding calcite SI values were 0.92 and 0.95. All values in the lake were higher than seawater.

Table 4-1 Water chemistry parameters measured or calculated for Storr's Lake water, conduit water, well water, and Dim Bay seawater collected in January 2016.

Sample	Temperature °C	pH	Conductivity mS/cm	Salinity[a] PSU	Turbidity NTU	DO[b] mg/L	Total Alkalinity mg/L as $CaCO_3$	Ca hardness mg/L as $CaCO_3$
Northern Sector	**25.9**	**8.42**	**56.32**	**36.66**	**123.0**	**6.36**	**121**	**1397**
stdev[c]	0.7	0.09	1.27	0.51	42.0	1.67	17	62
n	60	46	60	60	16	60	16	16
Southern Sector	**25.9**	**8.4**	**56.12**	**36.64**	**98.0**	**4.65**	**142**	**1361**
stdev	0.7	0.05	1.67	1.03	6.0	2.51	11	30
n	13	10	13	13	7	13	7	7
Conduit	**24.7**	**7.96**	**3.34**	**1.74**	**0.7**	**4.46**	**273**	**250**
stdev	3.1	0.17	1.11	0.50	0.1	0.60	10	28
n	4	4	4	4	2	4	2	2
GRC Well[d]	**26.2**	**7.54**	**n/a**	**n/a**	**1.9**	**3.60**	**247**	**n/a**
stdev	n/a[e]	n/a	n/a	n/a	n/a	n/a	n/a	n/a
n	1	1	n/a	n/a	1	1	1	n/a
Seawater	**26.1**	**8.13**	**45.90**	**29.02**	**0.8**	**7.05**	**118**	**950**
stdev	n/a	n/a	n/a	n/a	n/a	n/a	n/a	n/a
n	1	1	1	1	1	1	1	1

Table 4-1—*Continued*

Sample	Mg hardness mg/L as $CaCO_3$	Ca^{2+} mmol/L	Mg^{2+} mmol/L	Na^{+} mmol/L	K^{+} mmol/L	Sr^{2+} mmol/L	HCO_3^{-} mmol/L	Cl^{-} mmol/L	SO_4^{2-} mmol/L
Northern Sector	**7322**	**13.40**	**60.38**	**564.8**	**12.37**	**0.16**	**2.50**	**680.4**	**38.6**
stdev	218	0.18	0.99	6.6	0.39	0.01	0.15	180.2	10.7
n	16	12	12	12	12	12	16	12	12
Southern Sector	**7403**	**13.61**	**61.78**	**574.5**	**12.60**	**0.16**	**2.84**	**744.1**	**39.0**
stdev	186	0.17	1.87	15.8	0.39	0.01	0.22	71.8	3.9
n	7	7	7	7	7	7	7	7	7
Conduit	**450**	**2.03**	**2.10**	**19.3**	**0.65**	**0.06**	**5.46**	**22.1**	**0.5**
stdev	255	0.07	0.05	0.4	0.34	0.00	0.20	1.5	0.4
n	2	2	2	2	2	2	2	2	2
GRC Well	**n/a**	**1.10**	**1.42**	**2.5**	**0.09**	**0.09**	**4.94**	**3.3**	**0.5**
stdev	n/a	n/a	n/a	n/a	n/a	n/a	n/a	n/a	n/a
n	n/a	1	1	1	1	1	1	1	1
Seawater	**5950**	**10.32**	**53.12**	**439.2**	**9.84**	**0.08**	**2.36**	**346.8**	**26.8**
stdev	n/a	n/a	n/a	n/a	n/a	n/a	n/a	n/a	n/a
n	1	1	1	1	1	1	1	1	1

Table 4-1—*Continued*

Sample	Mg/Ca mole/mole	Sr/Ca mole/mole	$SI_{calcite}$	$SI_{aragonite}$
Northern Sector	**4.52**	**0.012**	**0.92**	**0.75**
stdev	0.07	0.000	0.11	0.11
n	12	12	12	12
Southern Sector	**4.54**	**0.012**	**0.98**	**0.81**
stdev	0.09	0.001	0.07	0.07
n	7	7	7	7
Conduit	**1.04**	**0.030**	**0.68**	**0.51**
stdev	0.06	0.000	0.02	0.02
n	2	2	2	2
GRC Well	**1.30**	**0.084**	**0.27**	**0.11**
stdev	n/a	n/a	n/a	n/a
n	1	1	1	1
Seawater	**5.15**	**0.008**	**0.70**	**0.53**
stdev	n/a	n/a	n/a	n/a
n	1	1	1	1

[a] Salinity was calculated by multiply the conductivity value with 0.667 to obtain PSU value (Boyd, 2002).

[b] “DO” represents “dissolved oxygen”.

[c] “stdev” represents “standard deviation”.

[d] “GRC Well” represents “Gerace Research Center well”.

[e] “n/a” represents “not applicable”.

Stromatolite Morphology

The pinnacle mound (terminology from Paul et al. 2016) sample (WS1) was collected from the southwestern shore of Storr's Lake at a water depth of 111 cm (Figure 4-3). The hand sample was the side part broken off a much larger mound (Figure 4-4) and was split off with a soil shovel in the field. The mound was found attached to a mangrove root or branch at the base with a dated ^{14}C age of 2120 ± 30 yr. The hand sample was ~22 cm long, ~6 cm wide, and ~18 cm tall and the entire mound was ~38 cm long, ~32 cm wide, and ~25 cm tall. The sample appeared buff at the top and light brownish with some reddish layers at the core and the bottom. The surficial crust was smooth and consisted of a hard bulbous structure with green spots scattered on top of it showing the residues of the microbial mat. The crust was about 7 to 8 cm thick at the top of the mound and was followed by continuous horizontal laminations within the interior of the sample shown below (Figure 4-5). The fine-laminated layers were very fragile and crumbled easily.

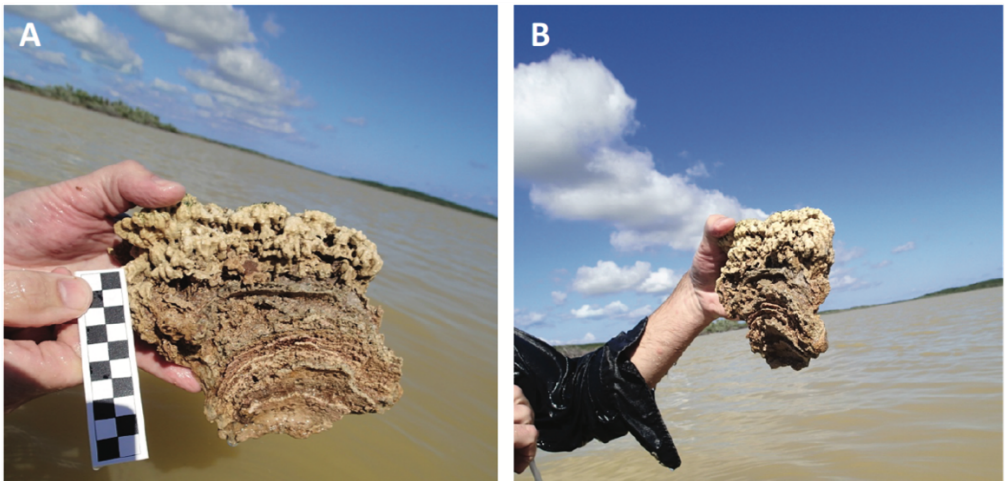

Figure 4-3 Front view (A) and side view (B) of the pinnacle mound sample (WS1) collected from the southern sector of Storr's Lake about 250 meters from the western shore.

Figure 4-4 Photograph of WS1 and the entire mound and where the collected hand sample was split off (in the person's left hand).

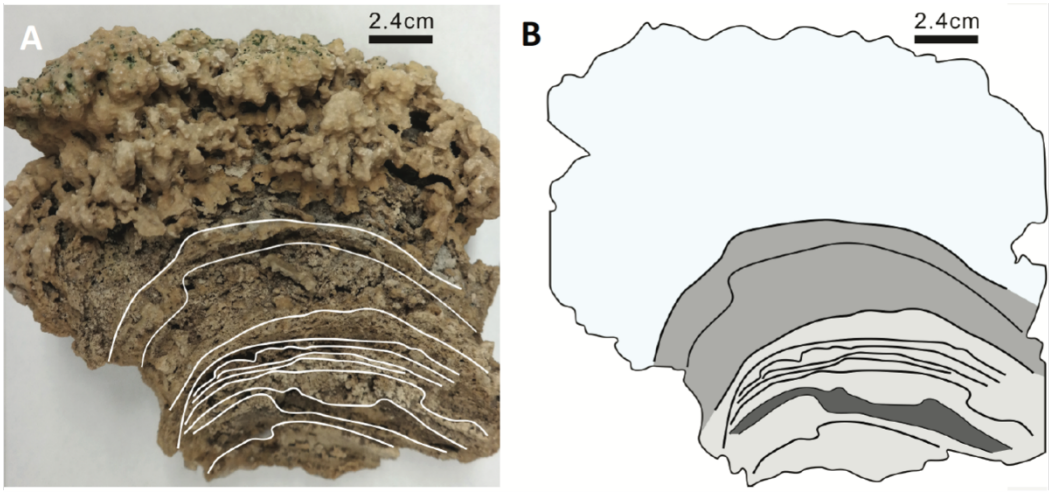

Figure 4-5 (A) Interior view of WS1 with white lines showing the identified laminations; (B) zones outlined in (A) illustrating the different growth phases: light green represents the top crust, light and dark grey represent horizontal layers.

The plateau-mushroom (terminology from Paul et al. 2016) sample (WN7) was pulled from the soft muddy sediment at the deepest part of the lake. It was covered in soft mud and lacked any green spots on the surface. The sampling location was along the WN transect (from the western shoreline to the Cactus Island, Figure 2-1C) at a water depth of ~60 to 70 cm. The entire sample was large (~30 cm long, ~22 cm wide, and ~20 cm tall) and had a buff color (Figure 4-6). The top crust had a branched, networked structure on the surface and a solid region below (as seen in cross-section) lacking any prominent, horizontal stratified layers that extended between 5 and 6 cm at the top of the sample. In its bottom-most region, it exhibited well-laminated layering for 2–3 cm (Figure 4-7).

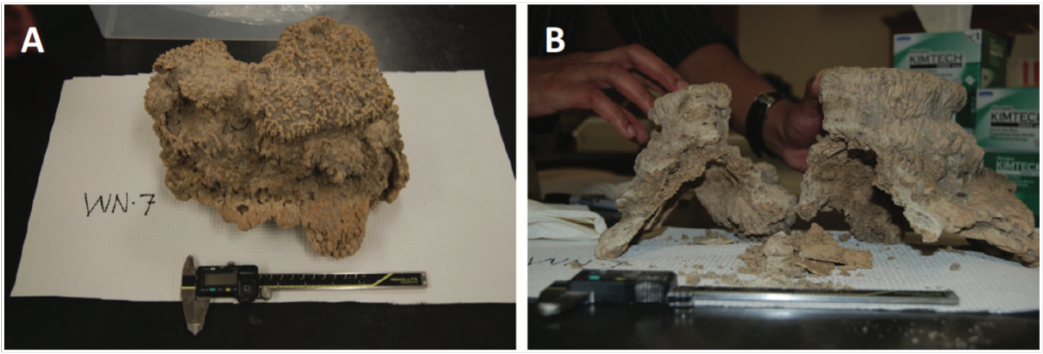

Figure 4-6 Top view (A) and side view (B) of the plateau-mushroom sample (WN7) collected from the northern sector Storr's Lake about 293 meters from the western shore. The whole hand sample was sawed in half (B). The analyzed specimen was the left (smaller) half.

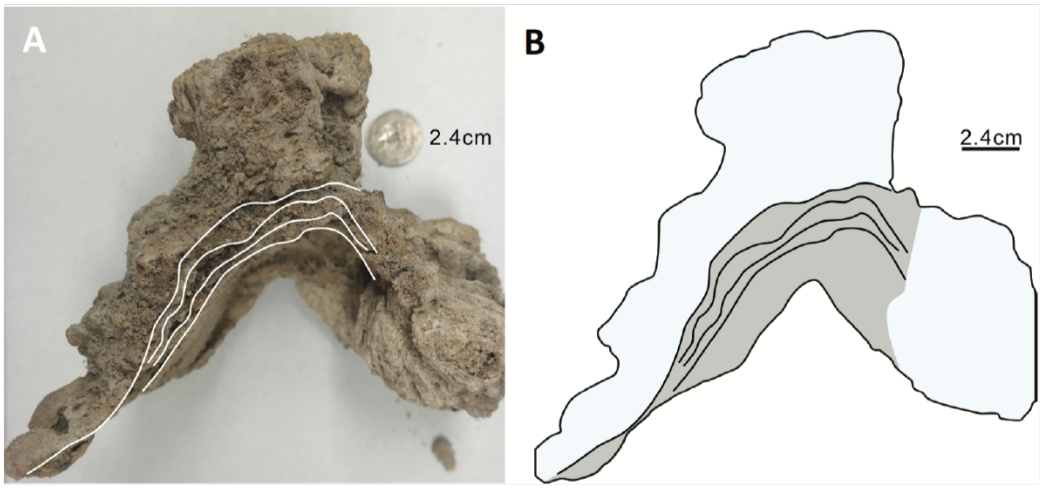

Figure 4-7 (A) Interior view of WN7 with white lines showing the identified laminations; (B) zones outlined in (A) illustrating the different growth phases: light green represents the top crust and grey represents laminations.

Microscopic Characterization

Petrographic analysis of thin sections revealed that the interior of the pinnacle mound and plateau-mushroom is characterized by a large amount of void space, trace amount of organic material and skeletal detrital components, with the bulk of the material made up of several forms of micrite and microspar (Figure 4-8 and Figure 4-10B). Micrite (crystal grains with diameters <4 μm; Folk, 1959) occurs in a clotted fabric with peloidal clusters and exhibits opacity suggesting that it is not only fine-grained but also contains organic material, whereas microspar (diameters 4-10 μm) exhibits more clarity and a crystalline form (Figure 4-10A and Figure 4-11). Brown to dark patches suggest some organics are preserved within the dense micrite (Figure 4-8). Some trapped sediment grains (e.g., ostracod shell) and micritized ooids are found primarily within the dense micritic laminae (Figure 4-9).

The smooth outer crusts (both the top and the sides of the pinnacle mound and plateau-mushroom) in thin sections are characterized by thin laminations and mainly

composed of microspar; Figure 4-10A). The interior of the pinnacle mound (WS1) has the thickest and least laminated peloidal and clotted micrite separated by pore space (~0.5-1mm) (Figure 4-10B). Microspar also lines cavities in the clotted and peloidal micrite (Figure 4-11).

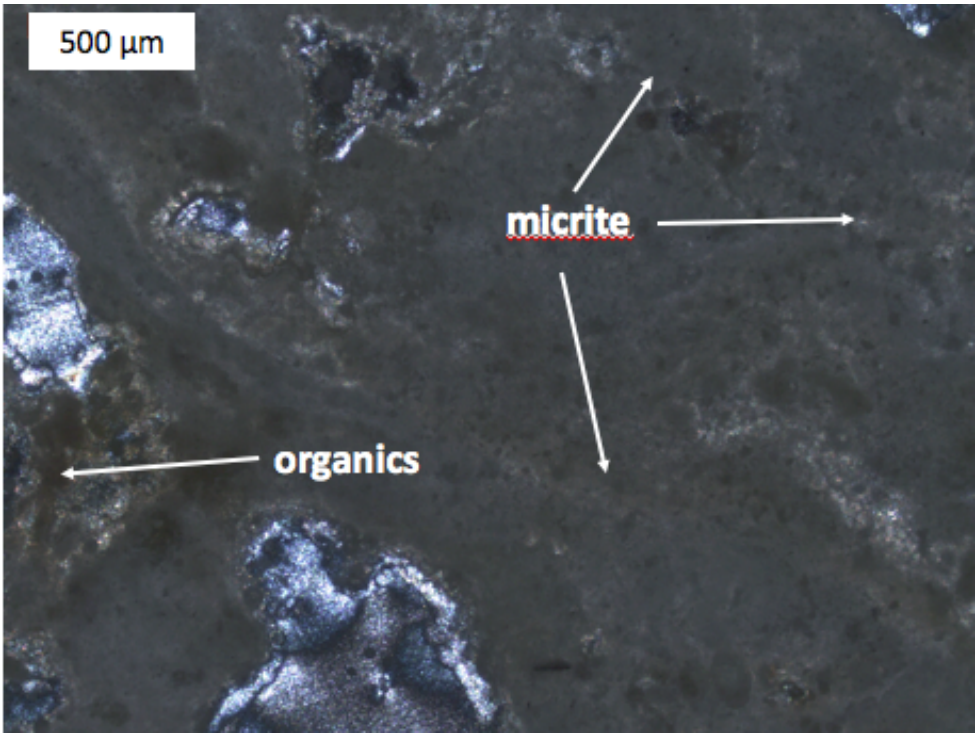

Figure 4-8 Polarized light thin section micrograph of pinnacle mound interior (WS1-1) showing organics and micrite.

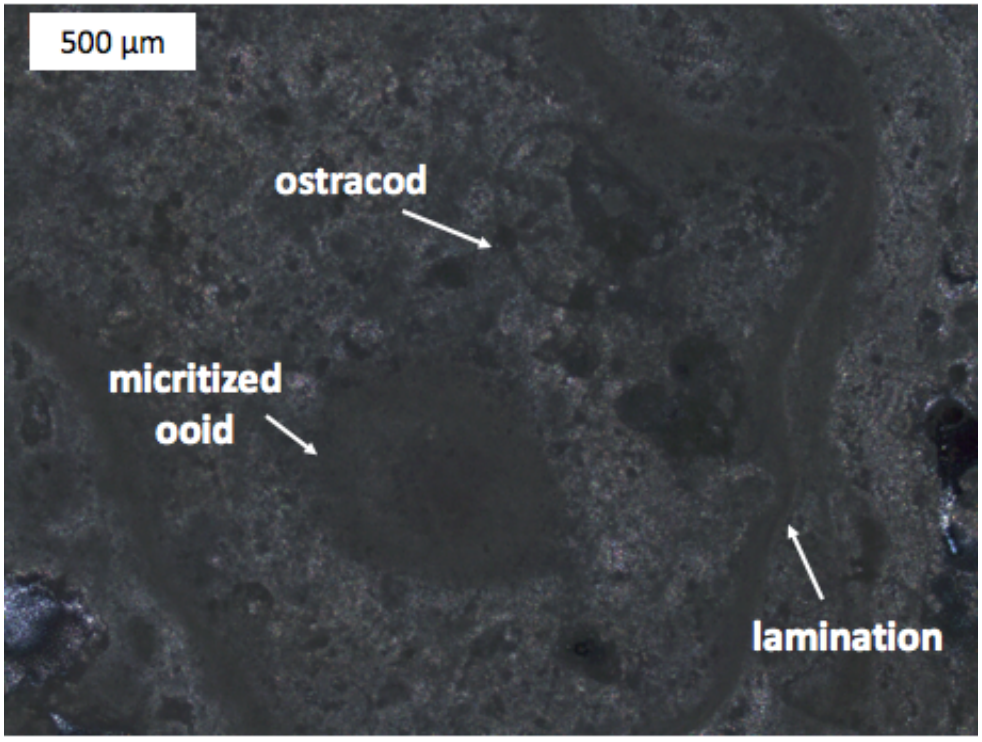

Figure 4-9 Polarized light thin section micrograph of pinnacle mound lamination (WS1-6) close to the side surface showing trapped grains (ostracod shell and micritized ooid) and micritic lamination.

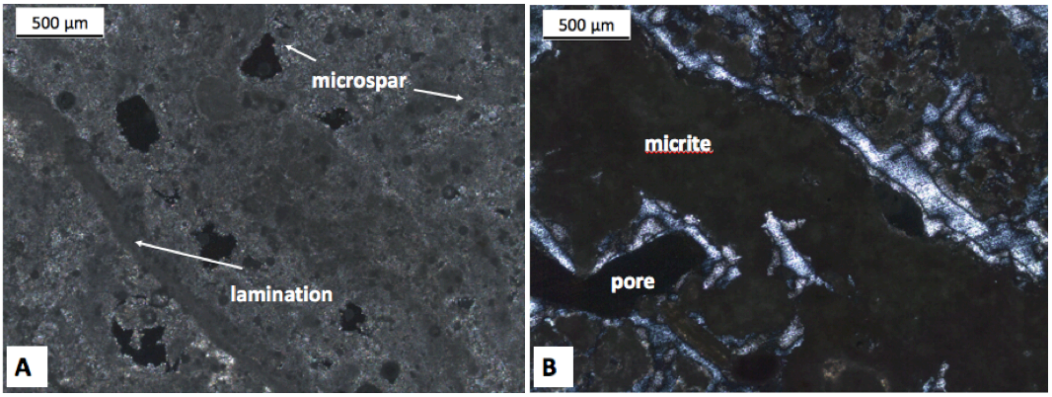

Figure 4-10 Polarized light thin section micrograph of plateau-mushroom (WN7). (A) crust zone (WN7-ii) showing microspar and laminated structure and (B) interior zone (WN7-3) showing clotted micrite that separated by pore space (~0.5-1 mm).

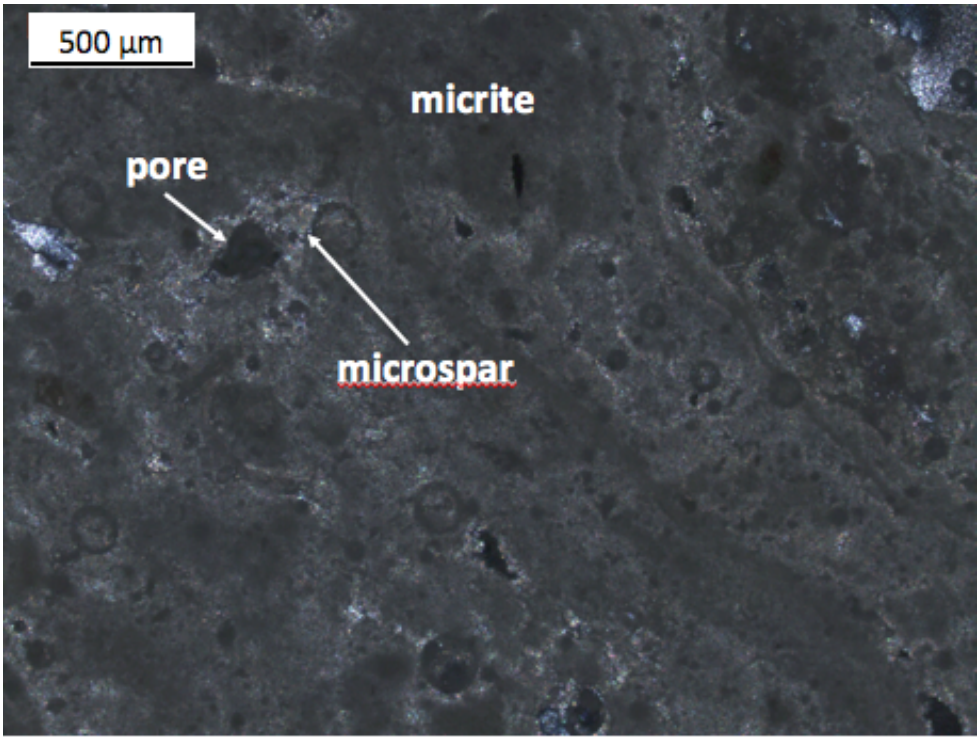

Figure 4-11 Polarized light thin section micrograph of pinnacle mound crust (WS1-i) showing microspar lined cavity in micrite and clotted micrite rimmed with microspar.

Mineralogy and Elemental Composition of Stromatolite Sublayers

Mineralogy

X-ray diffraction (XRD) analyses (Appendix B) were conducted with individual samples collected from multiple positions within the pinnacle mound (WS1; n = 13) and plateau-mushroom stromatolitic knob (WN7; n = 5) to discern whether any spatial variability exists with respect to aragonite and high Mg-calcite content (Table 4-2). Some stromatolitic sublayer samples (n = 8) were found to contain trace to minor amount of halite as determined by XRD, which was ascribed to incomplete deionized water rinse prior to analysis.

High-Mg calcite was the dominant mineral (>87 wt.%) found in the samples collected from the top 8 cm surficial bulging crust of the pinnacle mound (Figure 4-12; WS1-i, WS1-ii, and WS1-iv), with minor amounts of aragonite detected. However, aragonite content increased (18-28 wt.%) in the deeper layers (WS1-1B and WS1-1) where continuous horizontal laminations were observed. The aragonite weight percentage reached the highest with a value of 96 wt.% at the central core of the stromatolitic knob (WS1-5 to WS1-6) located ~13 cm below the top surface and then aragonite weight percentage decreased a little to 78 wt.% at the base of this stromatolitic knob (WS1-9).

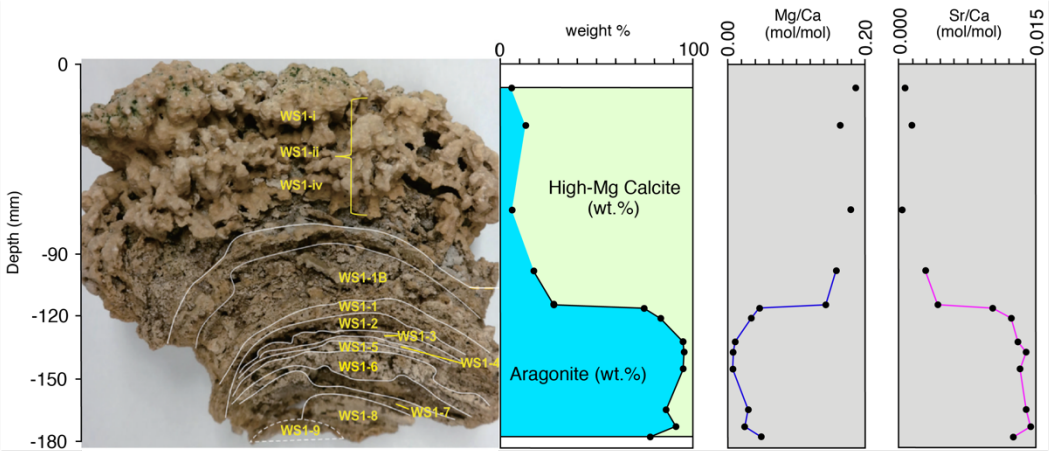

Figure 4-12 Sampling locations, mineralogical compositions from XRD, Mg/Ca molar ratios and Sr/Ca molar ratios from ICP-OES of the dissolved solid subsamples of the WS1 pinnacle mound sample. Lines connect samples that were sampled in a continuous sequence.

In the plateau-mushroom (Figure 4-13), the uppermost bulging knobs (WN7-i and WN7-ii) were enriched in high-Mg calcite (>75 wt.%) similar to the pinnacle mound, and the core to bottom (also interior) lateral layers (WN7-1, WN7-3, and WN7-4) mainly consisted of aragonite with weight percentages ranging from 87% to 90%. For both types

of stromatolitic knobs that were evaluated, there was an overall trend with aragonite/high-Mg calcite weight percentage ratios decreasing outward from the interior samples to the surface (i.e., WS1: 96/4 for interior core versus 6/94 for surficial sample; WN7: 90/10 for interior core versus 7/93 for surficial sample).

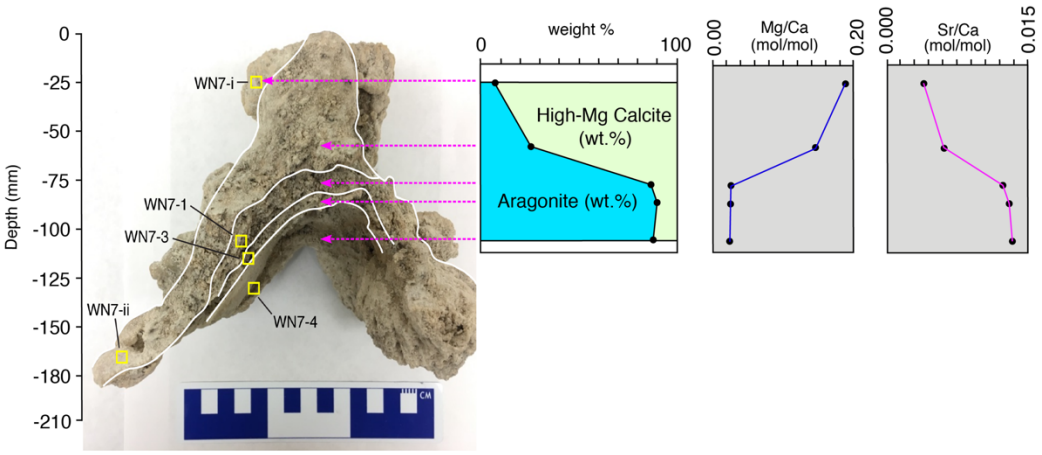

Figure 4-13 Sampling locations, mineralogical compositions from XRD, Mg/Ca and Sr/Ca molar ratios from ICP-OES of the solid subsamples of the WN7 plateau-mushroom sample.

Elemental Concentration

Insoluble components were not detected as residues by visual inspection following deionized water rinse (to remove salts), 2N hydrochloric acid digestion, and 30% hydrogen peroxide oxidation (to remove organic matter) performed on the solid powdered subsamples of the two stromatolitic knobs investigated. Concentrations of Na were at, or just above, detection limit of the ICP-OES (10 ppb). Variable mol % Mg (mol % Mg = $(M_{Mg}/M_{Ca+Mg})\times100\%$; 0.6–13.6% for WS1; 1.8-12.2% for WN7), Mg: Ca molar ratios (0.01-0.16 for WS1; 0.02-0.14 for WN7), and Sr: Ca molar ratios (0.003-0.015 for WS1; 0.004-0.013 for WN7) were identified in the samples analyzed (Table 4-2).

An inverse correlation was noted in both the pinnacle mound (WS1) and the plateau-mushroom (WN7) between the aragonite weight percentage and mole % Mg (Figure 4-14A). Both the pinnacle mound and plateau-mushroom displayed a sudden drop of mole % Mg from the outer crusts to the interior laminated zones. This signature was consistent with the sudden variations observed in aragonite weight percentage, Mg/Ca molar ratio, and Sr/Ca molar ratio. The Sr and Mg values obtained from ICP-OES analysis did correlate positively with the XRD aragonite and high-Mg calcite trends, respectively. In other words, a positive relationship was observed between wt.% Mg-calcite and Mg/Ca molar ratio; and wt.% aragonite and Sr/Ca molar ratio.

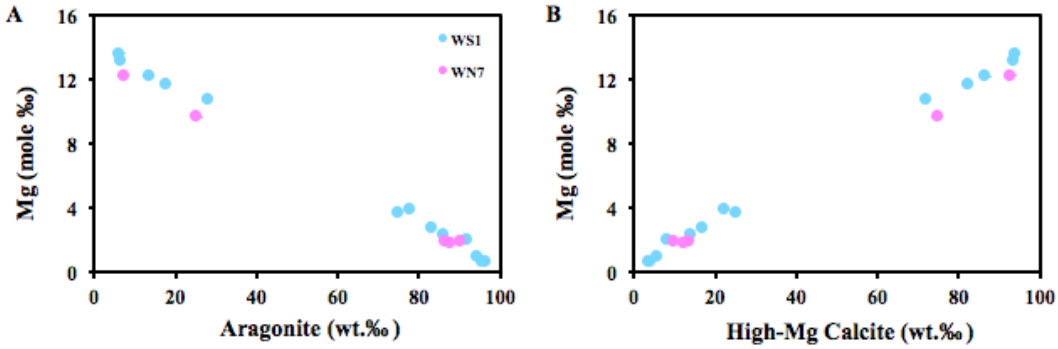

Figure 4-14 Mole % Mg shows (A) inverse correlation with aragonite weight percentage and (B) positive correlation with high-Mg calcite weight percentage for pinnacle mound (WS1) and plateau-mushroom (WN7).

Table 4-2 ICP-OES results and mineralogical compositions for the stromatolite subsamples showing the profile positions as noted in Figures 4-12 and 4-13.

	wt.%			*Molar ratio*			*Mol. %*	*wt.%/wt.%*
Sample	*Ca*	*Mg*	*Sr*	*Ca : Mg*	*Mg : Ca*	*Sr : Ca*	*Mg*	*Aragonite / Mg-calcite*
Pinnacle mound								
WS1-i	31.4	3.0	0.2	6.3	0.16	0.003	13.6	6/94
WS1-ii	33.1	2.8	0.3	7.2	0.14	0.004	12.2	13/87
WS1-iv	31.4	2.9	0.2	6.6	0.15	0.003	13.2	6/94
WS1-1B	30.7	2.5	0.4	7.5	0.13	0.005	11.7	18/82
WS1-1	32.6	2.4	0.5	8.3	0.12	0.006	10.7	28/72
WS1-2	35.9	0.9	0.9	25.6	0.04	0.011	3.7	75/25
WS1-3	35.9	0.6	1.0	34.7	0.03	0.013	2.8	83/17
WS1-4	35.9	0.2	1.1	107.4	0.01	0.013	0.9	94/6
WS1-5	36.3	0.2	1.1	146.1	0.01	0.014	0.7	96/4
WS1-6	35.8	0.1	1.1	154.8	0.01	0.014	0.6	96/4
WS1-7	34.7	0.5	1.1	40.8	0.02	0.014	2.4	86/14
WS1-8	34.5	0.4	1.1	47.8	0.02	0.015	2.0	92/8
WS1-9	33.9	0.8	1.0	24.2	0.04	0.013	3.9	78/22
Plateau-mushroom								
WN7-i	30.1	2.6	0.3	7.1	0.14	0.004	12.2	7/93
WN7-ii	32.0	2.1	0.4	9.2	0.11	0.006	9.7	25/75

Table 4-2—*Continued*

	wt.%			*Molar ratio*			*Mol. %*	*wt.%/wt.%*
Sample	*Ca*	*Mg*	*Sr*	*Ca : Mg*	*Mg : Ca*	*Sr : Ca*	*Mg*	*Aragonite / Mg-calcite*
Plateau-mushroom								
WN7-1	35.0	0.4	0.9	51.3	0.02	0.012	1.9	87/13
WN7-3	34.0	0.4	1.0	54.0	0.02	0.013	1.8	90/10
WN7-4	34.7	0.4	1.0	55.4	0.02	0.013	1.8	88/12

Carbon and Oxygen Isotopes

Oxygen isotope ratios relative to VPDB ($\delta^{18}O$) in the carbonate sublayers from the pinnacle mound and plateau-mushroom have a mean value of 1.1‰ with a standard deviation of ±0.3‰ (n= 18) and ranged between 0.7‰ and 1.9‰. Much more variation is seen in the $\delta^{13}C$ values (Table 4-3). The $\delta^{13}C$ values relative to VPDB had a mean value of -1.0‰ with a standard deviation of ±0.9‰ (n= 18) and ranged between -2.6‰ and 0.7‰ (Table 4-3).

Measurements of the $\delta^{13}C$ values of carbonate in successive sublayers of the stromatolitic knobs vary considerably (Figure 4-16), whereas the $\delta^{18}O$ values of the carbonate in the sublayers are relatively consistent (Figure 4-15). No clear pattern of variations (e.g., $\delta^{13}C$ vs. wt.% aragonite and $\delta^{18}O$ vs. wt.% aragonite) can be identified between the lamina (Figures 4-17A and 4-17B).

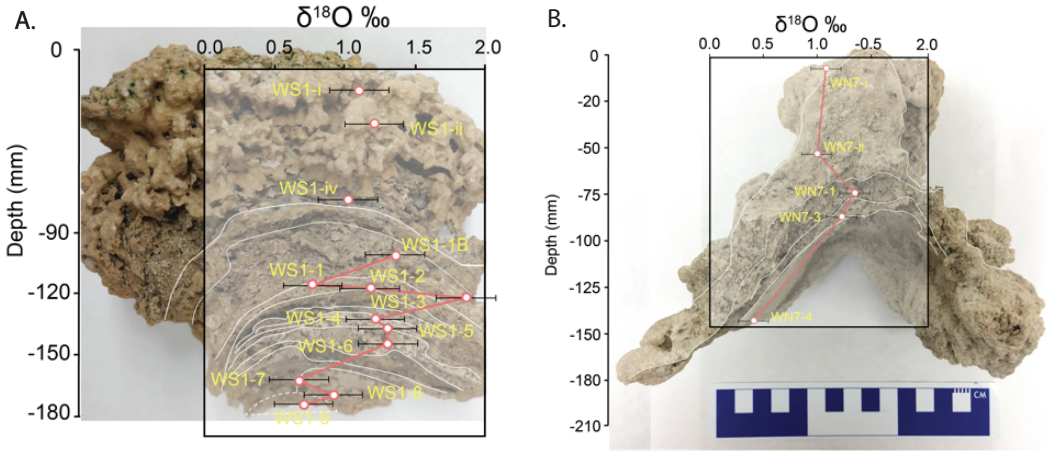

Figure 4-15 Depth profiles of $\delta^{18}O$ values measured in sublayers of (A) pinnacle mound (WS1), and (B) plateau-mushroom stromatolitic knobs (WN7) from Storr's Lake.

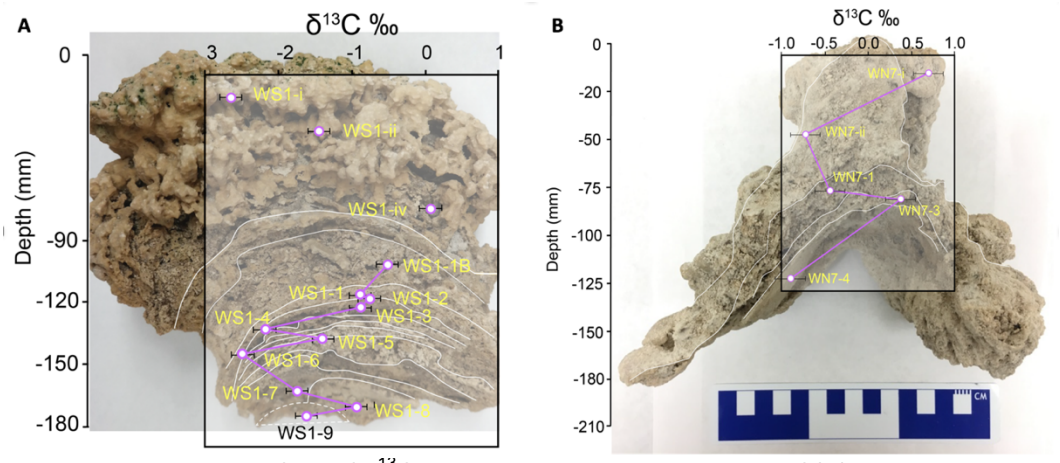

Figure 4-16 Depth profiles of $\delta^{13}C$ values measured in sublayers of (A) pinnacle mound (WS1), and (B) plateau-mushroom stromatolitic knobs (WN7) from Storr's Lake.

Table 4-3 $\delta^{13}C$ and $\delta^{18}O$ values of pinnacle mound (WS1) and plateau-mushroom (WN7) stromatolitic sublayers from Storr's Lake

	VPDB, ‰	
Sample	$\delta^{13}C$	$\delta^{18}O$
Pinnacle mound		
WS1-i	-2.6	1.1
WS1-ii	-1.4	1.2
WS1-iv	0.1	1.0
WS1-1B	-0.5	1.4
WS1-1	-0.9	0.8
WS1-2	-0.8	1.2
WS1-3	-0.9	1.9
WS1-4	-2.2	1.2
WS1-5	-1.4	1.3
WS1-6	-2.5	1.3
WS1-7	-1.7	0.7
WS1-8	-0.9	0.9
WS1-9	-1.6	0.7

Table 4-3—*Continued*

Sample	*VPDB, ‰* $\delta^{13}C$	$\delta^{18}O$
Plateau-mushroom		
WN7-i	-0.9	0.4
WN7-ii	0.4	1.2
WN7-1	-0.4	1.3
WN7-3	-0.7	1.0
WN7-4	0.7	1.1

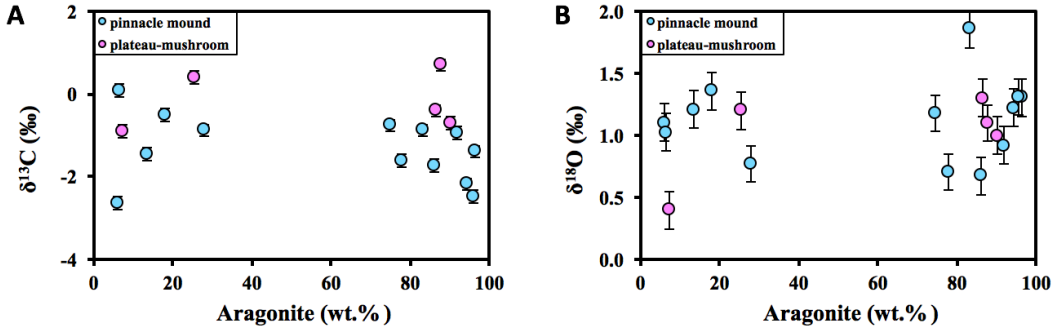

Figure 4-17 Cross plots of (A) $\delta^{13}C$ versus wt.% aragonite and (B) $\delta^{18}O$ versus wt.% aragonite. Two standard deviations for $\delta^{13}C$ and $\delta^{18}O$ are both 0.2‰ which were expressed as error bars in (A) and (B).

Mg Isotopic Compositions and Mg Isotope Fractionation

All of the Mg isotope data show a mass dependent behavior, defining a line with a gradient of 0.517 (Figure 4-18), within uncertainty of the equilibrium mass dependent fractionation line with a slope of 0.521 (Young et al., 2002). The Mg isotopic compositions of the selected lake water samples are spatially homogeneous (Table 4-4) with a mean $\delta^{26}Mg$ of -0.76 ± 0.12‰ ($2\sigma_n$, n = 12) relative to DSM3, which is identical to the $\delta^{26}Mg$ value of seawater (-0.83 ± 0.09‰; Ling et al., 2011). The values range between -0.87‰ and -0.66‰. Two seawater samples were prepared and measured together with the lake water samples. The $\delta^{26}Mg$ values of seawater from Dim Bay (San Salvador Island,

Bahamas) and from Galveston Bay (Texas, USA) are -0.86 ± 0.04‰ and -0.82 ± 0.09‰, respectively, which are in accordance with published seawater values (Ling et al., 2011).

The variation of measured $\delta^{26}Mg$ values in the sublayers of pinnacle mound and plateau-mushroom type stromatolitic knobs falls within the range from -3.04‰ to -2.33‰. Lower $\delta^{26}Mg$ values are found in high-Mg calcite sublayers for both pinnacle mound and plateau-mushroom (-3.02‰ and -2.97‰ in the pinnacle mound and plateau-mushroom, respectively). The aragonitic sublayers from the same pinnacle mound have a mean $\delta^{26}Mg$ value of -2.54‰, which is 0.04‰ heavier than the average $\delta^{26}Mg$ value of aragonitic sublayers (-2.58‰) from the plateau-mushroom. Values for $\Delta^{26}Mg_{carbonate\text{-}lake\ water}$ (= $\delta^{26}Mg_{carbonate}$ - $\delta^{26}Mg_{lake\ water}$) of aragonitic layers range from -1.51‰ to -2.00‰ for the sublayers of either the pinnacle mound or plateau-mushroom. In comparison, the $\Delta^{26}Mg_{carbonate\text{-}lake\ water}$ values for high-Mg calcite sublayers of the two stromatolitic knobs range from -2.11‰ to -2.24‰.

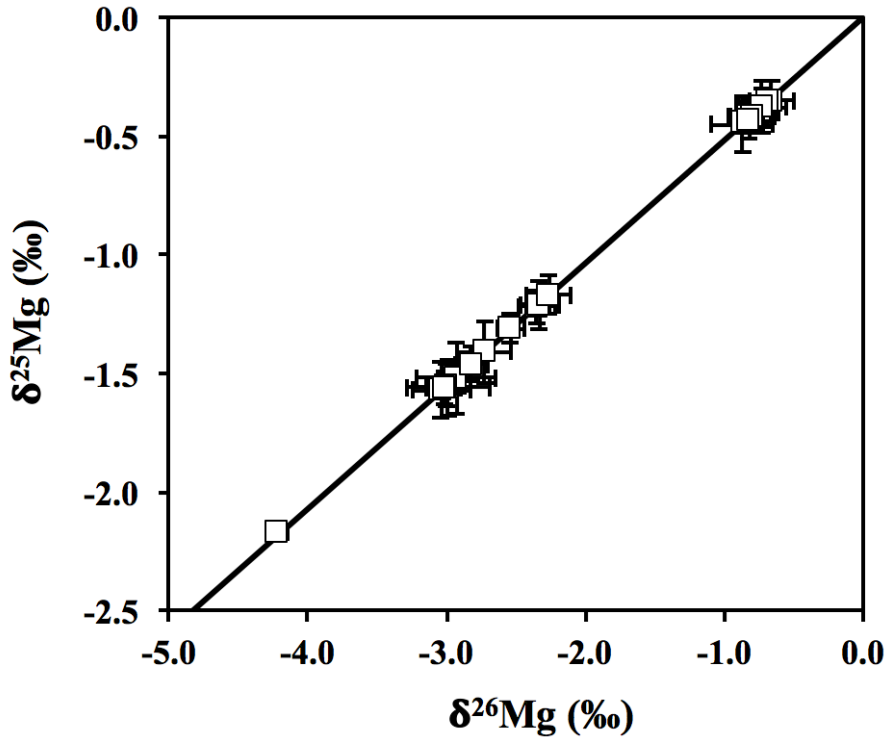

Figure 4-18 Magnesium three-isotope plot of all natural samples and standards analyzed in this study. The solid line represents the fractionation line with a slope of 0.517. Data are from Table 4-4.

Table 4-4 Magnesium isotope (δ^{26}Mg) measurements. Uncertainties are quoted as twice the standard deviation (2 σ) of "N" replicates (typically four).

Sample	δ^{25}Mg ± 2σ ‰ DSM3	δ^{26}Mg ± 2σ ‰ DSM3	$\Delta^{26}Mg_{carbonate\text{-}lake\ water}$[a] ‰ DSM3	N
Storr's Lake water				
EN1_55cm (M)	-0.39±0.06	-0.74±0.13		4
EN2_52cm (M)	-0.41±0.07	-0.78±0.12		4
WN3_102cm (J)	-0.38±0.05	-0.74±0.08		4
WN4_75cm (J)	-0.35±0.08	-0.66±0.16		4
WN6_120cm (J)	-0.42±0.03	-0.79±0.06		4

Table 4-4—*Continued*

Sample	$\delta^{25}Mg \pm 2\sigma$ ‰ DSM3	$\delta^{26}Mg \pm 2\sigma$ ‰ DSM3	$\Delta^{26}Mg_{carbonate\text{-}lake\ water}$[a] ‰ DSM3	N
Storr's Lake water				
WN8_61cm (M)	-0.42±0.06	-0.82±0.13		4
SWN2_40cm (J)	-0.38±0.08	-0.73±0.18		4
ES1_50cm (J)	-0.35±0.03	-0.68±0.05		4
WS1_5cm (J)	-0.38±0.11	-0.73±0.17		4
WS1_111cm (M)	-0.42±0.07	-0.80±0.17		4
WS3_40cm (M)	-0.45±0.12	-0.87±0.22		4
SSS1_40cm (M)	-0.44±0.07	-0.82±0.10		4
Dim Bay, San Salvador Island seawater				
SSI_SW (M)	-0.44±0.03	-0.86±0.04		6
Galveston Bay, Texas seawater				
GB_SW (M)	-0.43±0.03	-0.82±0.09		6
Pinnacle mound, Storr's Lake				
WS1-i (J)	-1.57±0.12	-3.04±0.21	-2.24	4
WS1-1 (M)	-1.56±0.12	-2.99±0.30	-2.19	4
WS1-6 (J)	-1.22±0.07	-2.35±0.13	-1.55	4
WS1-9 (M)	-1.41±0.13	-2.73±0.20	-1.93	4
Plateau-mushroom, Storr's Lake				
WN7-i (J)	-1.52±0.15	-2.93±0.28	-2.11	4
WN7-ii (M)	-1.55±0.09	-3.00±0.13	-2.18	4
WN7-1 (M)	-1.46±0.07	-2.82±0.12	-2.00	4
WN7-3 (J)	-1.21±0.10	-2.33±0.14	-1.51	4
Standards				
Cambridge 1 (M&J)	-1.31±0.06	-2.54±0.10		27
FZT (M&J)	-1.17±0.08	-2.26±0.16		29
SRM3131a (M&J)	-1.56±0.07	-3.02±0.12		25
NBS980 (J)	-2.17±0.03	-4.22±0.07		5

[a] $\delta^{26}Mg_{lake\ water}$ values of WS1_111cm and WN8_61cm were chosen to calculate $\Delta^{26}Mg_{carbonate\text{-}lake\ water}$ for sublayers of pinnacle mound and plateau-mushroom,

respectively. The sampling locations of WN8 and WN7 were close (~50 meters apart), so the WN8 water sample was used because no water samples were taken at location WN7. “(M)” means the samples were analyzed in March 2017 with Aridus delsovating system. “(J)” means the samples were analyzed in June 2017 with Apex delsovating system. “(M&J)” means the standards were analyzed in both March 2017 and June 2017 with Aridus and Apex delsovating system, respectively.

Chapter 5

Discussion

Characterization of Water Properties in Storr's Lake

Hydrochemical Facies and Lake Water Source

The use of interpretive diagrams for understanding the nature and origin of different water is well established. In this study, the Piper diagram (Piper, 1944; Figure 5-1) and Durov diagram (Durov, 1948; Figure 5-2) are used to indicate the relationship between different locations in the system and to extrapolate any mixing trends. According to the Piper diagram (Figure 5-1), the major hydrochemical facies can be classified. The water samples from the northern and southern sectors of Storr's Lake overlap in the diagram. Storr's Lake water is characterized as alkali-rich ($Na^+ + K^+$) water with prevailing chloride, belonging to a sodium chloride type water. Only one northern lake water sample (WN1 40cm) is observed to have more sulfate and less chloride compared to the other lake water. Seawater generally overlaps with the lake waters (all but WN1 40cm) and also belongs to sodium chloride type water. Conduit water plots on the left side of the lake water and seawater in all the three diagrams. Although conduit water is still classified as a sodium chloride type water, such water is characterized by increased alkaline earths ($Ca^{2+} + Mg^{2+}$) and bicarbonate compared to lake water and seawater. Gerace Research Center (GRC) well water plots away from lake water, seawater, and conduit water. GRC well water displays weak acidic anions exceeding strong acidic anions ($CO_3^{2-}+HCO_3^- > Cl^-+SO_4^{2-}$) and the prevailing of alkaline earths over alkali elements. GRC well water belongs to magnesium bicarbonate type water. Therefore, the water types in this study are divided into two categories: 1) conduit water, lake water, and seawater (sodium chloride type); 2) GRC well water (magnesium bicarbonate type).

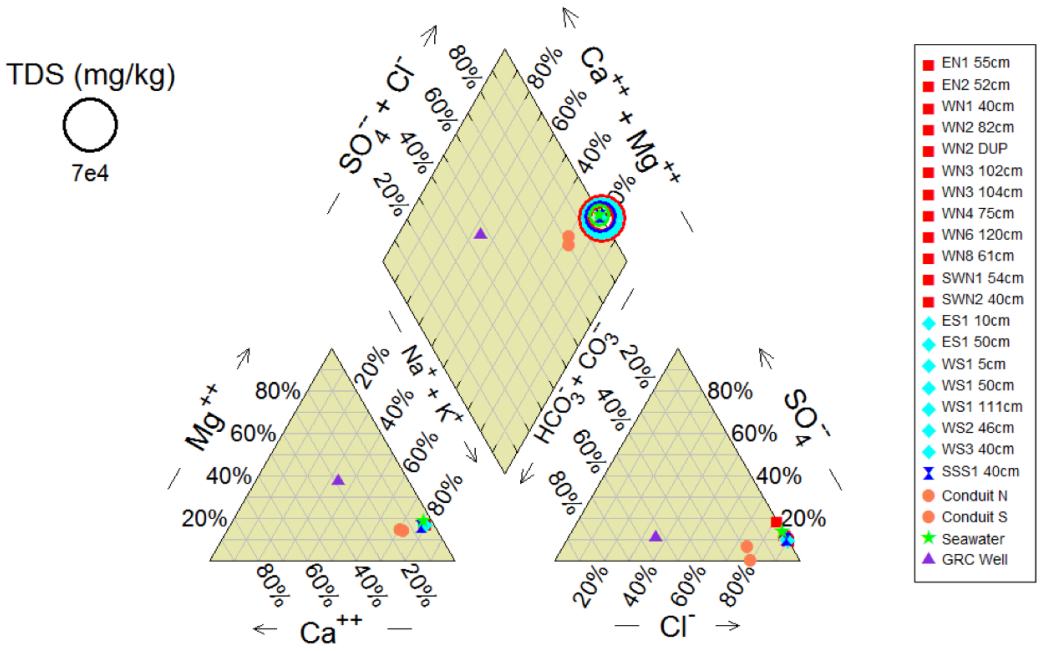

Figure 5-1 Piper trilinear diagram classifying major hydrochemical facies of Storr's Lake water, conduit water, seawater, and Gerace Research Center well water collected in this study in January 2016. Legend at right indicates where the samples were located. Red squares represent northern lake water and blue diamonds represent southern lake water. "TDS" represents "total dissolved solids". Plot constructed using Geochemist's Workbench program.

From the Durov plot (Figure 5-2), certain relationships can be inferred. Similar relationships are seen as that as observed in the Piper diagram (Figure 5-1). In the central rectangular plot (representing total major ion concentrations), lake water and seawater cluster at the lower left corner and conduit water plot upward and to the right of the lake water and seawater. GRC well water, however, is plotted in the middle of the plot. The three groups of water fall on a straight line, which can be interpreted as a mixing trend (Lloyd and Heathcoat, 1985).

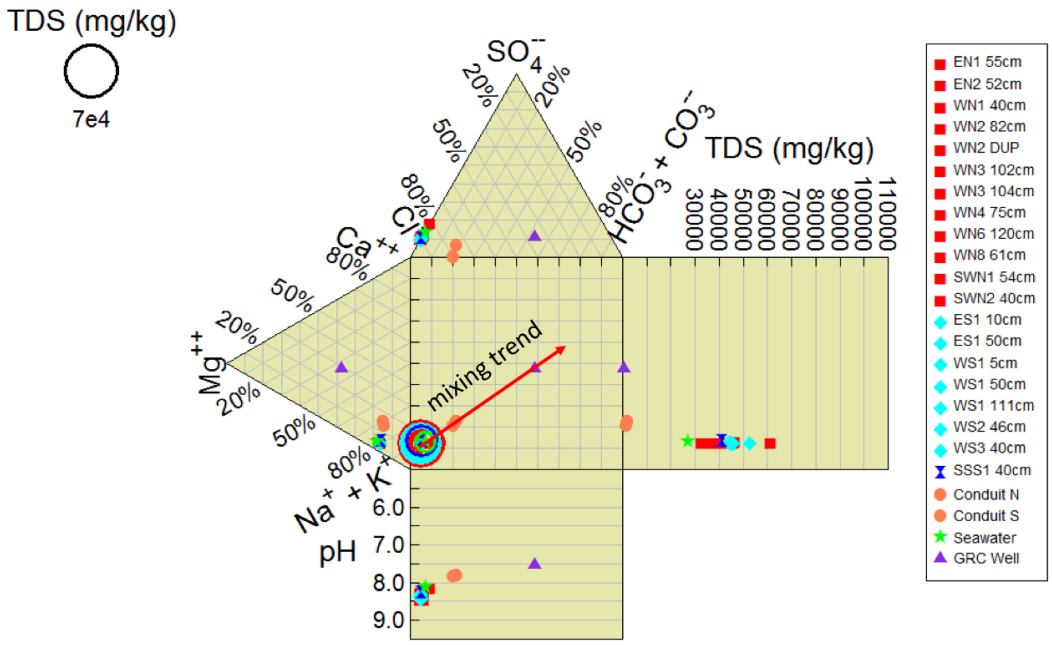

Figure 5-2 Durov plot depicting hydrochemical processes of Storr's Lake water, conduit water, seawater, and Gerace Research Center (GRC) well water collected in this study in January 2016. Red arrow indicates the mixing trend. Legend is at right. Red squares represent northern lake water and blue diamonds represent southern lake water. "TDS" represents "total dissolved solids" which is illustrated by the size of circles in this plot. Plot constructed using Geochemist's Workbench program.

The overlapping of lake water and seawater in both the Piper diagram and Durov plot suggests that seawater is the primary source for Storr's Lake water. This relationship is consistent with the evolutionary history of the depositional basins of Storr's Lake which were open to the ocean approximately 4300 years ago and started to close off ~ 3100 years ago (Zabielski, 1991). Conduit water falls on the mixing trend between seawater and GRC well water, but samples plot closer to seawater. GRC well water is regarded as the end member representing groundwater. Therefore, conduit water might be the product of mixing seawater and groundwater. The mixing trend is also observed in the

lower pH plot, where the pH values of conduit water falls in between the pH values of seawater and GRC well water. In the right total dissolved solid (TDS) plot to the right of the rectangular plot, lake water samples have TDS values ranging from 32000 to 62000 mg/kg which are higher than seawater (< 30000 mg/kg). Conduit water and the GRC well water have very small TDS values and the difference between the two types of water is indistinguishable on this plot. Lake water with higher TDS values than seawater reflects the hypersaline nature of the Storr's Lake due to evaporation.Spatial Homogeneity

Water temperature decreases from the shallow to deeper water levels at most sampling locations (Figure 4-1B). The surface layer (around 5 cm) of water is constantly mixed by wind and waves and is warmed by the sun, which explains the water temperature gradient in the water column. DO also decreases in the vertical water column profiles as shown at four sampling locations (Figure 4-1A). The decreasing trend of DO with water depth can be ascribed to several causes. The main mechanism is atmospheric diffusion where oxygen in the air is absorbed by surface water due to a difference in oxygen concentrations, while the lake water at deeper depths receives little oxygen from atmospheric diffusion. Oxygenic photosynthesis by microbial communities (e.g., cyanobacteria) releases oxygen into the water within the photic zone. However, the limited light condition at deeper horizons caused by high turbidity is unfavorable for large amounts of oxygenic photosynthesis and thus results in oxygen deficiency in deep water. Because conduit water in this study has a DO value slightly lower than the lake waters, conduit input at the surface has only a minimal impact on the oxygen content in the lake. Therefore, the entire profile can be explained by atmospheric diffusion and oxygenic photosynthesis in the surface water.

The thermal stratification observed in this study (in all three profiles except WS1) is consistent with an earlier investigation of the lake water by Mann and Nelson (1989) in

which they reported a minor and gradual stratification in the lake. The existence of stratified layers in the lake suggests that complete and rapid vertical mixing is hindered.

Besides temperature, the lake water also appears to be stratified with conductivity and pH. Conductivity of the shallower waters is generally higher than that of the deep waters for all depth profiles but WS1 (Figure 4-1C). The pH values seem to have the same variation trend for all depth profiles but WN4 (Figure 4-1D).

The profound evaporation effect of the surface water may explain the higher conductivity of the shallow waters, while the higher pH values might be ascribed to active oxygenic photosynthesis (consumes CO_2) at the surface horizons. Major cation concentrations (e.g., Mg^{2+} and Ca^{2+}) show little variations with water depth (Figure 5-3).

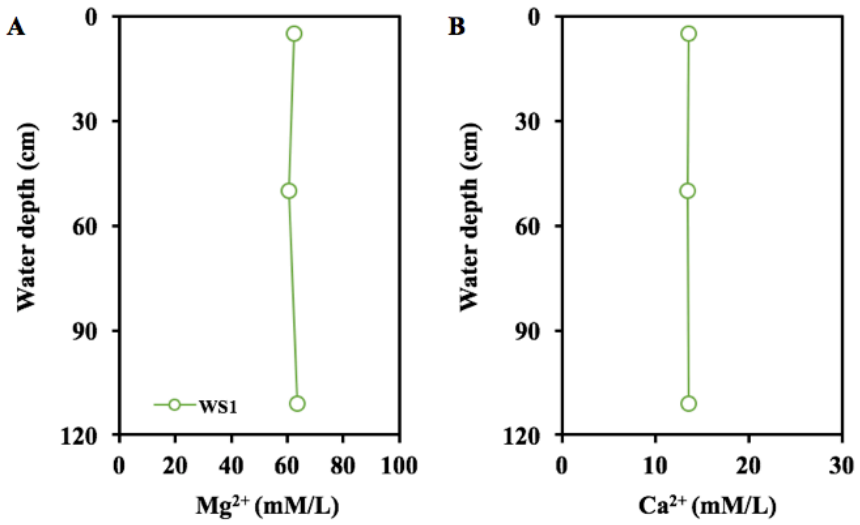

Figure 5-3 Variations of the (A) Mg^{2+} concentration and (B) Ca^{2+} concentration with water depth at sampling location of WS1 in Storr's Lake. The three water samples were collected at water depths of 5 cm, 50 cm, and 111 cm (just above the stromatolite head), respectively.

According to the investigations of the surface water from the WN transect in the North Sector of Storr's Lake, pH values and conductivity show an increasing trend from

the western shore to the middle of the lake. Surface water temperatures and DO values both display a similar increasing trend for the first four locations but drop at the fifth location (close to Cactus Island). The general increasing trend observed for the water parameters in the first four locations along the transect has also been reported in previous studies (Paul et al., 2016), and can be explained by conduit water flowing into the lake from the shore and gradually mixing with lake water. This mixing trend is not observed in major cations concentrations in the lake (e.g., Mg^{2+} and Ca^{2+}; Figure 5-4; Appendix B), which indicates that major cations are spatially homogeneous in the lake.

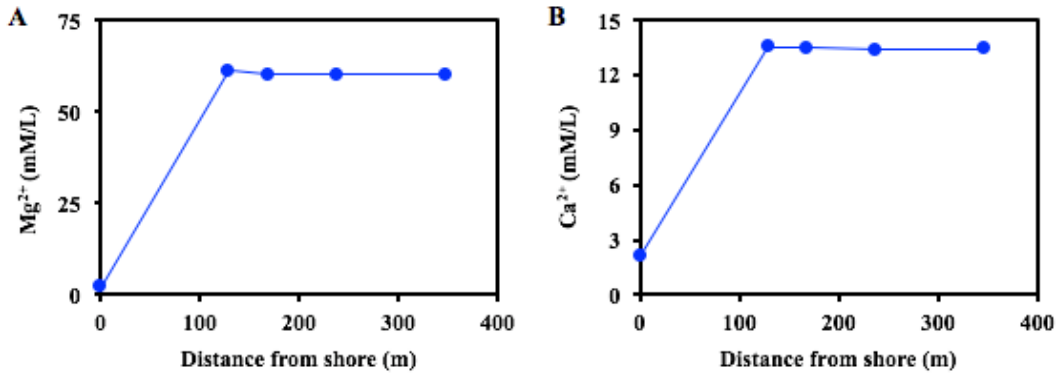

Figure 5-4 Variations of the (A) Mg^{2+} concentration and (B) Ca^{2+} concentration with the distance from shore at WN transect (from western shore to Cactus Island) in Storr's Lake. The five data points are conduit-N, WN1_40cm, WN2_82cm, WN3_104cm, and WN8_61cm. The last four lake waters were collected just above the stromatolite heads.

Seasonal Variations

Water chemistry data from Dupraz et al. (2013) and Paul et al. (2016) are summarized in Table 5-1 and Figures 5-5 and 5-6 for comparison with the data in this study to discuss potential seasonal variations of the lake water. Data for the northern lake water samples collected in the summer (Paul et al., 2016) overlap with the northern lake water samples collected in winter (this study) in both the Piper diagram and Durov plot,

suggesting major ion concentrations in the northern sector show slight seasonal variations. However, data from samples of the southern lake water collected in the summer (Dupraz et al., 2013) are different from the southern lake waters collected in winter in this study in both diagrams with prevailing alkaline earth metals and an increased TDS value, which demonstrates that the strong evaporation in summer can concentrate the southern lake water to a larger extent than in the Northern Sector. More profound seasonal variations in the southern sector compared to that in the northern sector is also observed in the saturation index of carbonate minerals (Figure 5-7; Table 4-1; Appendix B). McNeese (1988) noted that the salinity in the lake ranged from 70 to 100 PSU during the months of December to May, which were significantly higher than the salinity values of our study in January (ranging from 33 to 38 PSU). Previous studies have reported that rainfall events can cause considerable dilution of the lake water and result in lowered salinity (Pinckney et al., 1995). Hurricane Joaquin was reported to pass over the San Salvador Island in October 2015, which could explain this result.

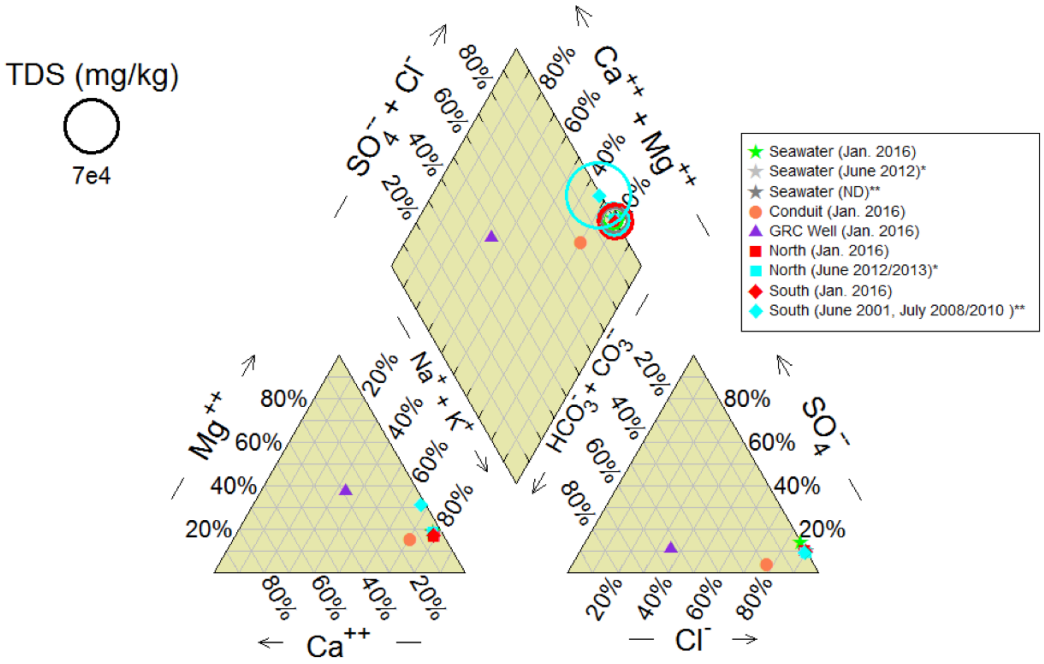

Figure 5-5 Piper trilinear diagram of Storr's Lake water, conduit water, seawater, and Gerace Research Center (GRC) well water collected in this study in January 2016 and in previous studies. "*" represents data from Paul et al. (2016) collected in June 2012/2013 and "**" represents data from Dupraz et al. (2013) collected in June 2001 and July 2008/2010. "ND" represents not determined.

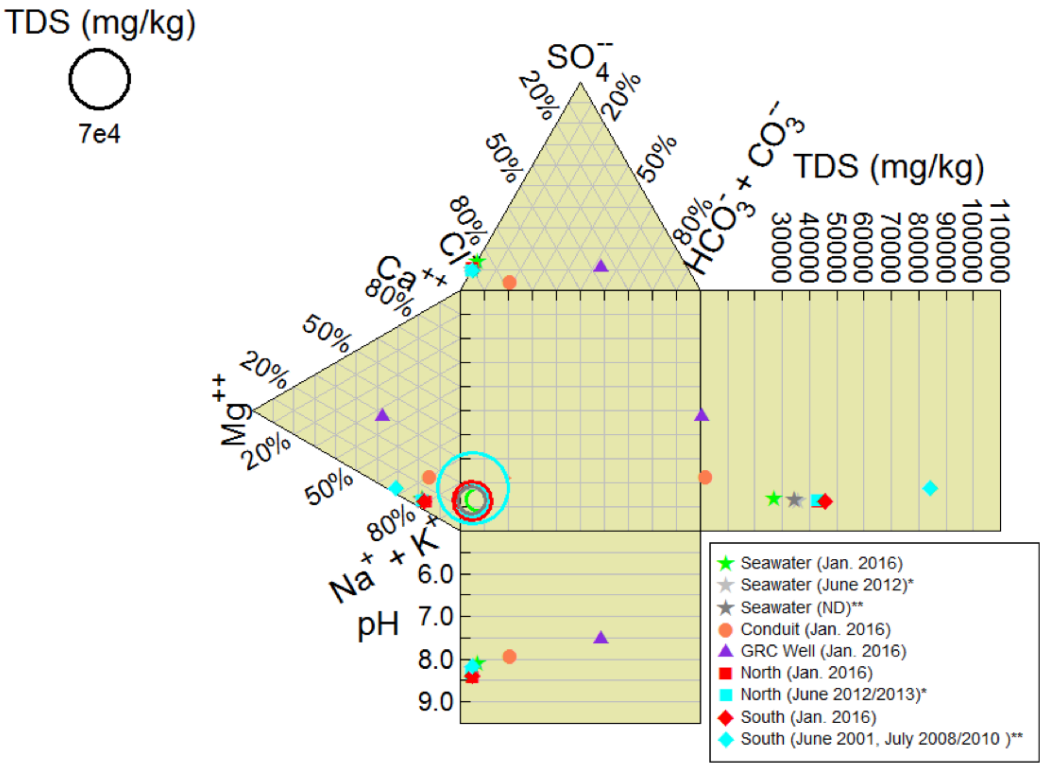

Figure 5-6 Durov plot of Storr's Lake water, conduit water, seawater, and Gerace Research Center (GRC) well water collected in this study in January 2016 and in previous studies. "*" represents data from Paul et al. (2016) collected in June 2012/2013 and "**" represents data from Dupraz et al. (2013) collected in June 2001 and July 2008/2010. "ND" represents not determined.

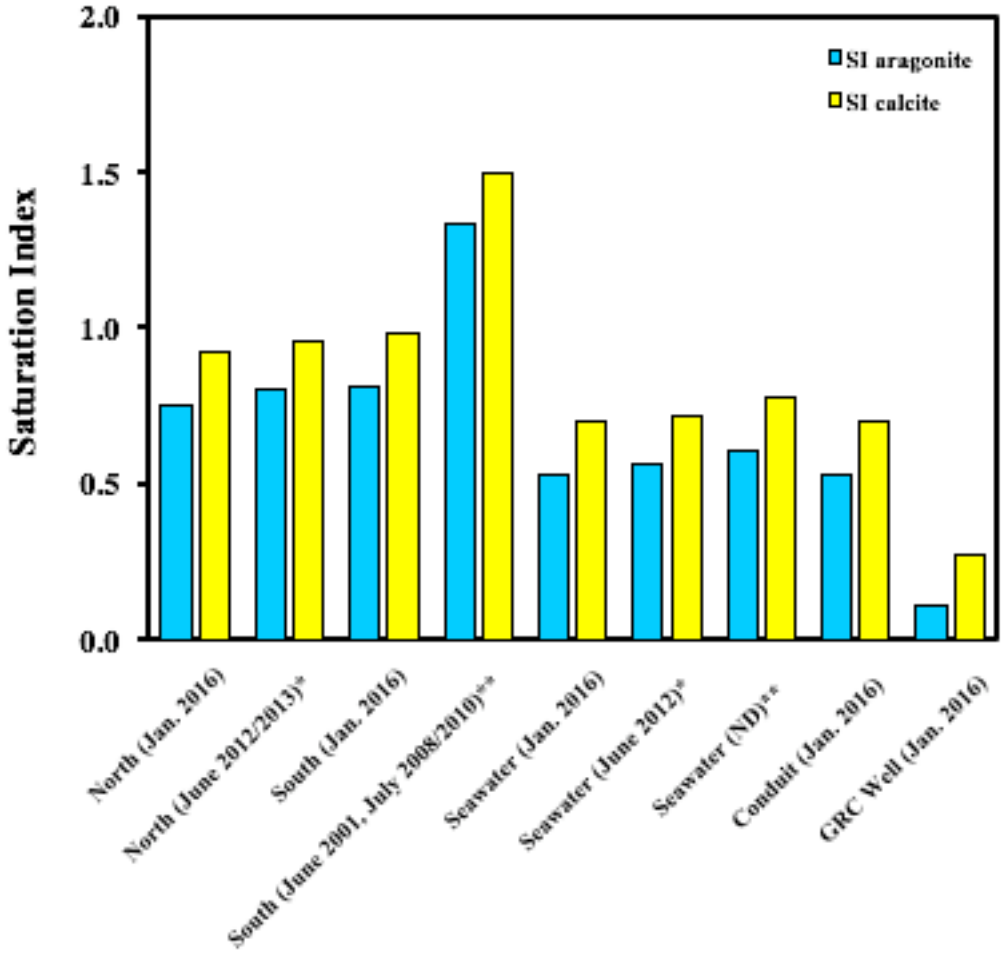

Figure 5-7 Saturation index of calcite and aragonite for Storr's Lake water, conduit water, seawater, and Gerace Research Center (GRC) well water collected in this study in January 2016 and in previous studies. "*" represents data from Paul et al. (2016) collected in June 2012/2013 and "**" represents data from Dupraz et al. (2013) collected in June 2001 and July 2008/2010. "ND" represents not determined. Saturation Index values were calculated in Geochemist's Workbench program.

Table 5-1 Water chemistry parameters of Storr's Lake water and seawater from Dupraz et al. (2013) and Paul et al. (2016).

Sample	Temperature °C	pH	Conductivity mS/cm	Salinity PSU	Turbidity NTU	DO[e] mg/L	Alkalinity mg/L as $CaCO_3$	Ca hardness mg/L as $CaCO_3$
North_P[a]	27.0	8.36	61.47	41.05	117.0	4.97	135	1239
South_D[b]	38.5	8.19	88.08	58.75	n/a[f]	n/a	658	n/a
Seawater_P[c]	28.0	8.26	53.90	36.00	5.0	4.70	113	1060
Seawater_D[d]	28.0	8.26	52.47	35.00	n/a	n/a	116	n/a

Table 5-1 (continue)

Sample	Mg hardness mg/L as $CaCO_3$	Ca^{2+} mmol/L	Mg^{2+} mmol/L	Na^{+} mmol/L	K^{+} mmol/L	Sr^{2+} mmol/L	HCO_3^{-} mmol/L	Cl^{-} mmol/L
North_P[a]	6647	13.56	74.19	622.8	13.49	n/a	2.71	634.3
South_D[b]	n/a	17.48	275.17	1181.4	n/a	n/a	13.16	1216.0
Seawater_P[c]	5840	9.63	58.40	513.8	10.67	n/a	2.26	535.9
Seawater_D[d]	n/a	10.38	53.28	467.7	n/a	n/a	2.31	545.7

Table 5-1—*Continued*

Sample	SO_4^{2-} mmol/L	Mg/Ca mole/mole	Sr/Ca mole/mole	$SI_{calcite}$	$SI_{aragonite}$
North_P[a]	31.4	5.14	n/a	0.96	0.80
South_D[b]	60.5	15.74	n/a	1.50	1.33
Seawater_P[c]	28.1	6.06	n/a	0.72	0.56
Seawater_D[d]	28.1	5.13	n/a	0.78	0.61

[a] Data is from Paul et al. (2016). The water samples were collected in June 2012 and 2013. The anions chloride and sulfate were analyzed only for the 2012 samples.

[b] Data is from Dupraz et al. (2013). The water samples were collected in spring (March 2000, 2002, and 2006) and summer (June 2001, July 2008, 2010).

[c] Data is from Paul et al. (2016). The seawater was collected in June 2012.

[d] Data is from Dupraz et al. (2013). No time information for the seawater collection.

[e] "DO" represents "dissolved oxygen".

[f] "n/a" represents "not applicable".

Mg Isotopic Compositions of Lake Water

Spatial homogeneity: The lake water samples that were analyzed for Mg isotope composition have covered the northern (EN1, EN2, WN4, WN6, WN3, WN8), the middle (SWN2), and the southern sectors of the Storr's Lake (ES1, WS1_5cm, WS1_111cm, WS3, SS1). In addition, these samples covered both the peripheral and the center zones of the Storr's Lake (Figure 2-1). More carbonates (both lake sediments and microbialites) are proposed to precipitate from the lake water with higher $SI_{calcite}$ and $SI_{aragonite}$ values. As a result, the lake water with a higher saturation state might have higher $\delta^{26}Mg$ values (carbonates preferentially uptake ^{24}Mg from aqueous solution). Because the water of Storr's Lake displays various saturation states at different locations, it is possible to form Mg isotope heterogeneity within the lake. However, the data showed that the $\delta^{26}Mg$ values of the lake water samples are relatively constant (between -0.66‰ and -0.87‰) within the analytical error (Figure 5-8; Table 4-4). This minor variability indicates that the Storr's Lake is spatially homogeneous with respect to Mg isotope composition, although the lake water from different locations has various saturation states (Figures 5-10C and 5-10D) and Mg concentrations (Figure 5-10A). If the surface and bottom water of the Storr's Lake are not well mixed with regard to Mg isotopes, the bottom water could be enriched in ^{26}Mg compared to the surface water due to carbonate precipitation close to the lake bottom. To test this hypothesis, two lake water samples at the same location but from different water depths (WS1_5cm and WS1_111cm) were analyzed for their Mg isotope composition. The results showed that the two lake water samples have identical $\delta^{26}Mg$ values within error (-0.73±0.17‰ for WS1_5cm and -0.80±0.17‰ for WS1_111cm), suggesting there is likely no Mg isotope stratification in the Storr's Lake.

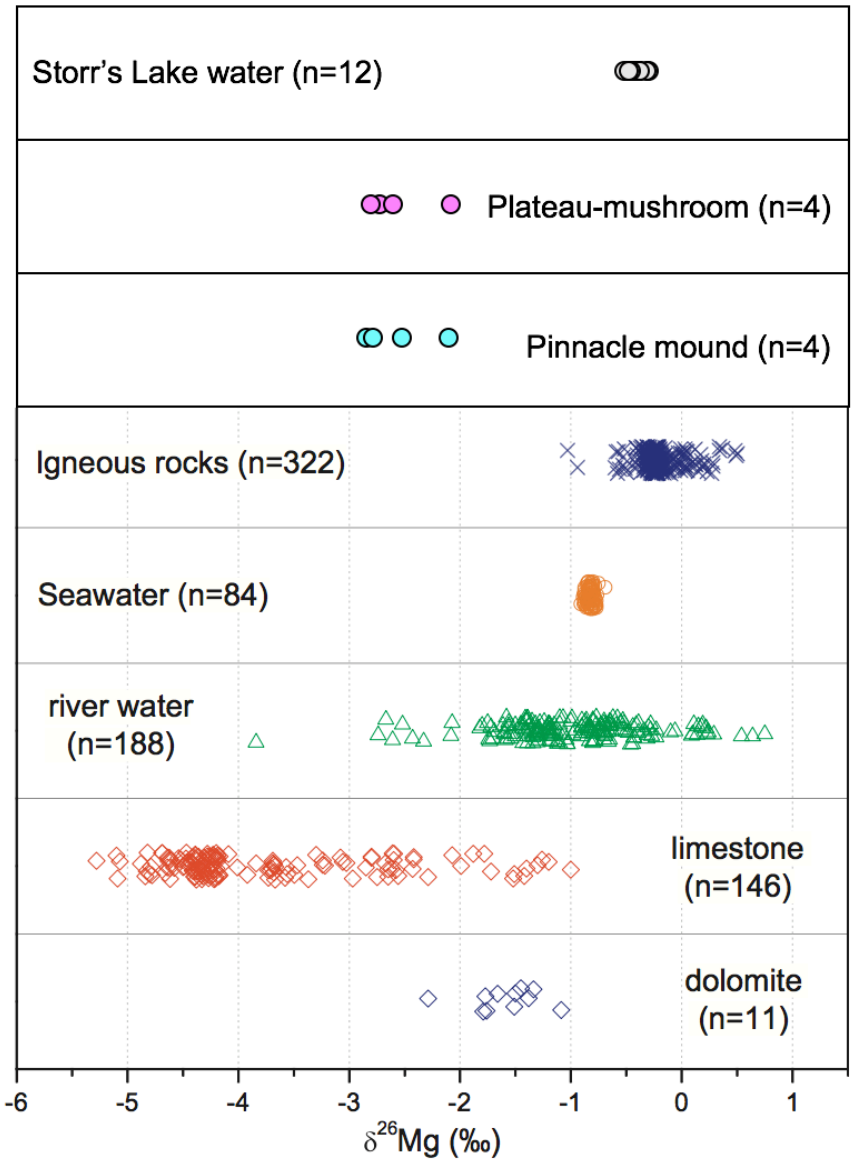

Figure 5-8 Comparison of the $\delta^{26}Mg$ values of Storr's Lake water and stromatolitic sublayers with the published Mg isotope data from different geological reservoirs. $\delta^{26}Mg$ values of igneous rocks are from Tipper et al. (2006a, 2008); Teng et al. (2007, 2010), Wiechert and Halliday (2007), Brenot et al. (2008), Chakrabarti and Jacobsen (2010), Dauphas et al. (2010), Jacobson et al. (2010), Li et al. (2010) and Liu et al. (2010); $\delta^{26}Mg$

values of seawater are from de Villiers et al. (2005), Tipper et al. (2006, 2008, 2010), Hippler et al. (2009), Teng et al. (2010) and Ling et al., (2011); δ^{26}Mg values of river water are from de Villiers et al. (2005), Tipper et al. (2006, 2006b), Brenot et al. (2008), Pogge von Strandmann et al. (2008a, b) and Wimpenny et al (2011); δ^{26}Mg values of limestone (Mg-calcite) are from Galy et al. (2002), de Villiers et al. (2005), Tipper et al. (2006), Buhl et al. (2007), Brenot et al. (2008), Hippler et al. (2009) and Immenhauser et al. (2010); δ^{26}Mg values of dolomite are from Galy et al. (2002), Chang et al. (2003), Brenot et al. (2008), and Jacobson et al. (2010). Adapted from Li et al. (2012).

Correlation with water parameters: The δ^{26}Mg values of lake waters show no correlation with water temperature (Figure 5-9A), pH (Figure 5-9B), dissolved oxygen (Figure 5-9C), total alkalinity (Figure 5-9D), and Mg/Ca molar ratio (Figure 5-10B), indicating the Mg isotope composition of lake water is independent of the variations of physical and chemical parameters of the lake water.

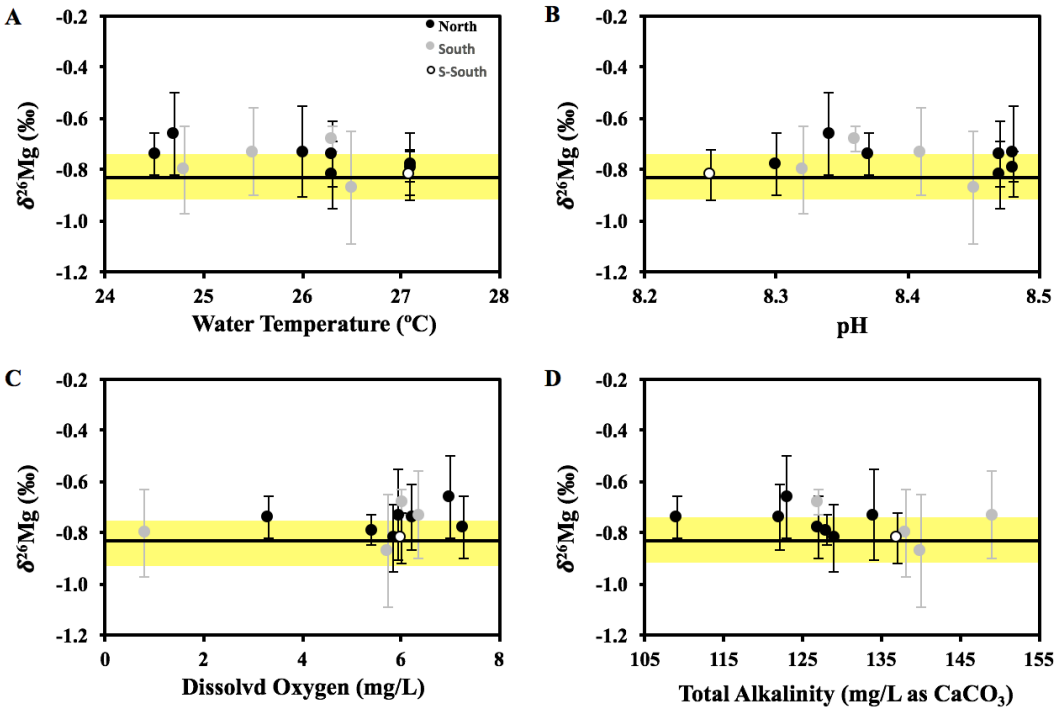

Figure 5-9 Cross plots of (A) δ^{26}Mg versus water temperature, (B) δ^{26}Mg versus pH, (C) δ^{26}Mg versus dissolved oxygen, and (D) δ^{26}Mg versus total alkalinity. Lake water samples (collected in January 2016) from the northern sector, southern sector, and south southern sector are black circles, grey circles, and unfilled circles, respectively. The horizontal line and yellow bar represent the average δ^{26}Mg of seawater (-0.83±0.09‰; Ling et al., 2011).

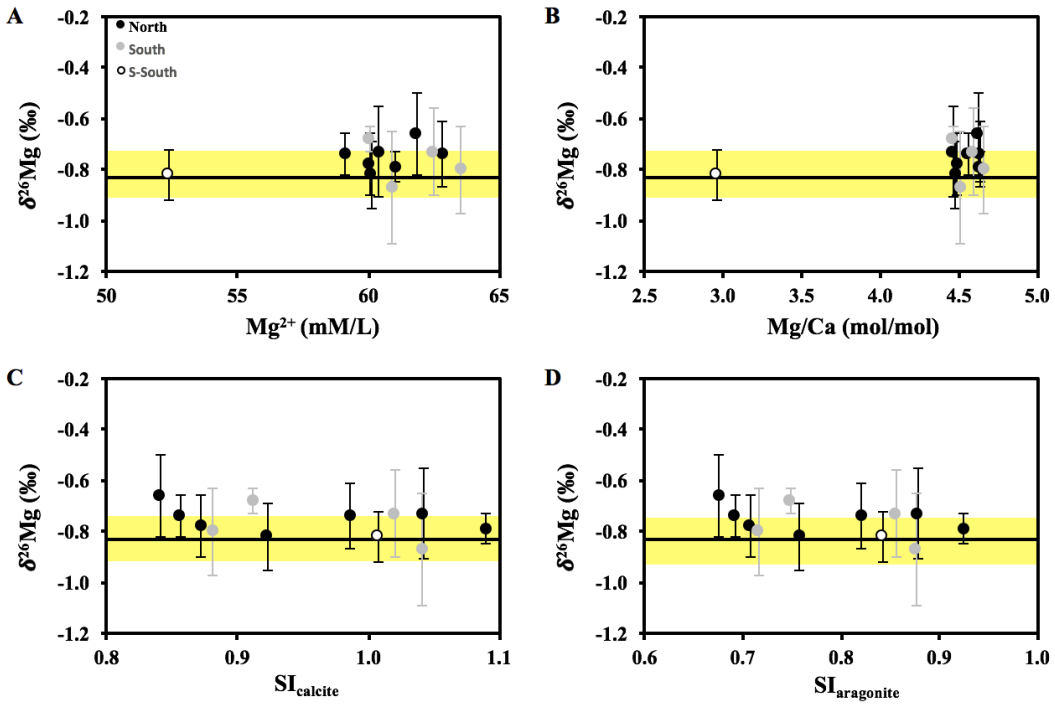

Figure 5-10 Cross plots of (A) δ^{26}Mg versus Mg^{2+} concentration, (B) δ^{26}Mg versus Mg/Ca molar ratio, (C) δ^{26}Mg versus $SI_{calcite}$, and (D) δ^{26}Mg versus $SI_{aragonite}$. Lake water samples (collected in January 2016) from the northern sector, southern sector, and south southern sector are black circles, grey circles, and unfilled circles, respectively. The horizontal line and yellow bar represent the average δ^{26}Mg of seawater (-0.83±0.09‰; Ling et al., 2011).

Mg isotope budget of Storr's Lake: The identical δ^{26}Mg values of lake water and seawater suggest that seawater is the primary Mg influx to the Storr's Lake and dominates the Mg isotope composition of the lake. In theory, ground water also brings in a fraction of Mg to the lake and therefore contributes to the Mg isotope budget of the lake. Although the Mg isotope composition of the ground water (GRC well) that enters the Storr's Lake was not analyzed in this study, it is reasonable to assume the ground water has a δ^{26}Mg value of -1.69‰ which is the δ^{26}Mg value of ground water in karstic environment from Galy et al. 2002). However, a variable δ^{26}Mg signature is not

resolvable in the δ^{26}Mg ratios of the lake water. This anomaly can be explained by the low Mg concentration in ground water and minor input flux from ground water compared to seawater input, which is consistent with the conclusion derived from the cations and anions data.

The formation of microbialite and the precipitation of carbonates in lake sediments are two primary modes of Mg removal from the water of Storr's Lake. Based on the mean δ^{26}Mg ratios of the analyzed microbialite sublayers, it is assumed that the microbialite has an averaged Mg isotope composition of -2.78‰. Because the lake sediment is dominated by aragonite, the δ^{26}Mg value of the bottom lake sediment is assumed to be -2.56‰ (the mean δ^{26}Mg ratio of aragonitic sublayers from the two stromatolitic knobs). Either the formation of microbialites or the precipitation of carbonates in lake sediments will render the lake water enriched in ^{26}Mg. However, no obvious distinction is observed in the δ^{26}Mg values of lake water and that of seawater. Based on the mineralogy study in this research, high-Mg calcite only dominates the outer crust of the stromatolitic knobs with the interior zone enriched in aragonite (contains little Mg). In addition, the lake sediment is primarily composed of aragonite. As a result, the Mg flux out of the lake via carbonate precipitation is probably minor compared to the whole mass of Mg in the lake, which explains the absence of an increase in δ^{26}Mg value of lake water. The Mg isotope budget of Storr's Lake with a steady-state lake water composition is schematically summarized in Figure 5-11.

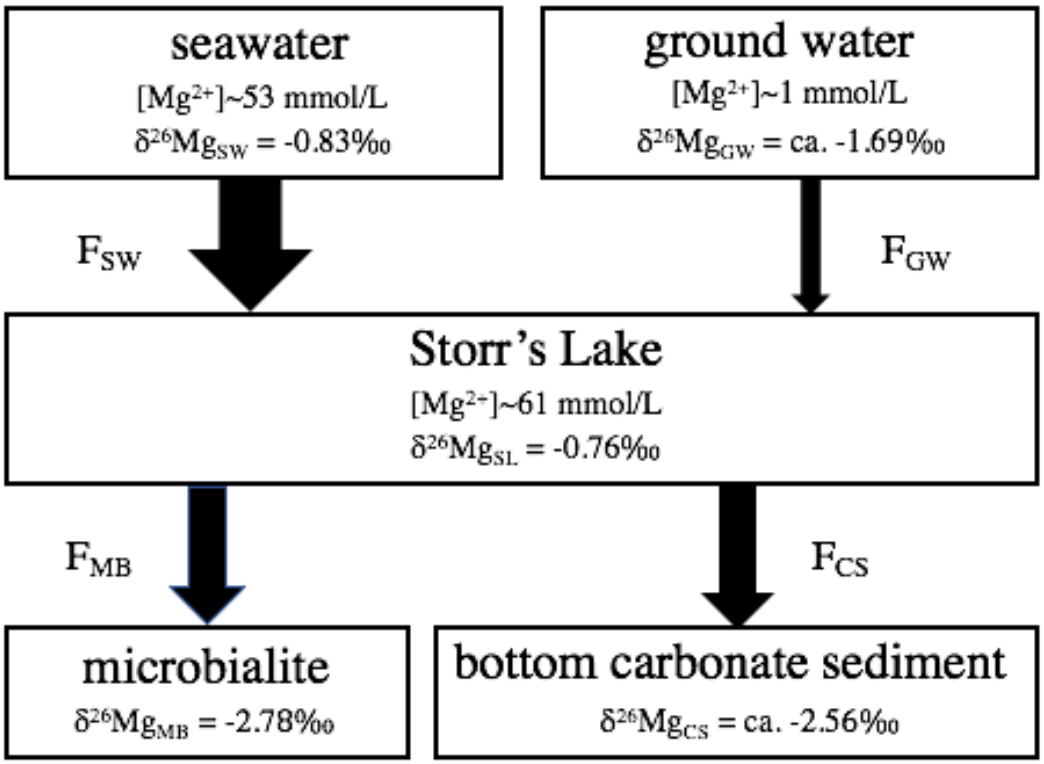

Figure 5-11 Schematic of the Storr's Lake Mg isotope budget with a steady-state lake water composition. The primary Mg flux into Storr's Lake (F_{SW}) results from seawater, with δ^{26}Mg value of $-0.83‰$, whereas minor input flux comes from ground water with an estimated δ^{26}Mg value of $-1.69‰$ (from Galy et al. 2002). The primary fluxes of Mg out of Storr's Lake are through microbialite precipitation (F_{MB}) with Mg isotopic composition of $-2.78‰$ and carbonate deposition in lake bottom sediment (F_{CS}) with Mg isotopic composition of ca. $-2.56‰$, based on δ^{26}Mg values of stromatolitic knob sublayers in this study.

Morphology and Mineralogy of Stromatolites from Storr's Lake

Morphology of Microbialites

Although this study only targeted two types of stromatolitic knobs (pinnacle mound and plateau-mushroom), microbialites with other external morphologies were identified and collected during the field trip. They include calcareous knobs, cauliflower-top mushroom, and multi-cuspate, as termed by Paul et al. (2016). Calcareous knobs and multi-cuspate morphological types were found to develop at a shallow water depth, whereas the two mushroom morphological types (plateau-mushroom and cauliflower-top mushroom) were found at deeper depths of 70-100 cm. Pinnacle mound types normally appear at the locations with the deepest water depth (~100-110 cm). The overall microbialite morphology is generally considered to be primarily controlled by environmental factors, though microorganisms play the role of actual accretion and fabric development (Dupraz et al., 2006). One of the major controls of morphological type is the water depth of Storr's Lake, and in turn the availability of light for the microorganisms, especially phototrophs. The bulging nature toward the top of the stromatolitic knobs indicates that the area closest to the surface is the most productive region, where maximum light is accessible and water depth is conducive (Paul et al., 2016).

Mineralogy of Stromatolitic Knobs

Distribution of carbonate minerals: Both high-Mg calcite and aragonite were identified in the pinnacle mound and plateau-mushroom samples, which is consistent with the study of Paul et al. (2016). We observed that the mol % Mg in the carbonate minerals of the pinnacle mound (WS1) and plateau-mushroom (WN7) type stromatolitic knobs initially decreased from the top to middle positions (WS1-i to WS1-2; WN7-i to WN7-1) and then was relatively constant (increased or decreased in a small range), moving from the middle toward the bottom of the stromatolitic knob (WS1-3 to WS1-9; WN7-3 to WN7-

4). The high-Mg calcite weight percentage correlated positively with the mol % Mg of the pinnacle mound and the plateau-mushroom types (Figure 4-14B). Generally, both the two stromatolitic knobs displayed a distribution pattern of high-Mg calcite enriched in the surficial crusts and aragonite dominated in the inner laminated zones. Previous studies of Storr's Lake stromatolitic knobs have reported only the presence of Mg-calcite and no aragonite (Hattin, 1983; Pentecost, 1989; Neumann et al., 1989; Fowler, 2011; Dupraz et al., 2013) except Paul et al (2016) as noted. Based on the observation result in this study, one possible explanation is that those studies only took the surface samples for mineralogy analysis.

The aragonite weight percentage showed a strong inverse correlation with Mg/Ca molar ratio but displayed a positive correlation with Sr/Ca molar ratio, which further confirmed the presence of aragonite (Figures 4-12 and 4-13). The large radius of Sr^{2+} (1.18 Å) is more readily accepted into the aragonite structure, whereas the smaller Mg^{2+} ion (0.72 Å) gets preferentially incorporated as a replacement for Ca^{2+} (1.00 Å) in calcite (Krauskopf and Bird, 1994). Calcite can accept a higher proportion of Mg in its crystal structure relative to aragonite, especially when the calcite is precipitated in biologically mediated reactions (Weiner and Dove, 2003). Therefore, aragonite is expected to have more Sr and less Mg than calcite does, which supports the results obtained in this study.

Factors that Control Mineralogy

Wind-blown detritus from the East Beach (located northeast of Storr's Lake) could be carried across the entire lake during the intense storm activity, and incorporated into the stromatolite structure (Paul et al., 2016). The incorporation of the carbonate-forming organisms was confirmed by the observation of ostracod and micropeloid in thin sections (Figure 4-9) and also by previous studies (Neaumaan et al. 1989 for gastropods; Park, 2012 for ostracodes; Fowler, 2011 for foraminifera). In all of the studies, including

this research, the detrital grains were only found to consist of a very small portion of the microbialite structure and were far from enough to explain the dominant source of aragonite in the laminated zones.

Saturation state: The saturation state of the carbonate minerals in water has been shown to be an essential component in determining stromatolitic knob development (Dupraz and Visscher, 2005). The SI values for current Storr's Lake water samples as determined in this research and previous studies (Figure 5-5 and Table 5-1; Dupraz et al., 2013; Paul et al., 2016) indicate that the lake water is supersaturated with respect to both calcite and aragonite. Saturation index can only explain the coexistence of high-Mg calcite and aragonite. However, the factors that control the spatial distribution of the two minerals observed within the stromatolitic knobs in this study still remain unknown.

In the stromatolitic knobs of this study, aragonite-enriched interiors were surrounded by Mg-calcite-rich exterior/surface zones. Because the interiors of the stromatolitic knobs represent older stromatolite growth, high-Mg calcite rather than aragonite seems logically regarded as the autochthonous mineral. No obvious recrystallization signature was observed on the high-Mg calcite of the surficial crusts (Figures 4-10A and 4-11), which potentially rules out the possibility of high-Mg calcite resulting from diagenetic transformation of aragonite.

Temperature: Several other factors such as temperature, the presence of metal ions, and organic matter are well known to have a strong influence on which polymorph is obtained (Han et al., 2006; Jin et al., 2011). Aragonite has been reported to be preferentially precipitated at higher temperatures (> 40 °C; Pentecost 2005). The daytime water temperature of the northern part of Storr's Lake in this study (winter) and in Paul et al. (2016) (summer) clustered around 24°C to 28 °C (Tables 4-1 and 5-1). Dupraz et al. (2013) observed a much higher daytime water temperature (averaged 38.5 °C; Table 5-1)

for southern part of Storr's Lake in summer. Because none of the recorded water temperature exceeded 40 °C, temperature cannot be the driving factor to form aragonite.

Mg/Ca molar ratio of solution: It is widely reported that a sufficiently high concentration of Mg^{2+} ions poisons the growth of calcite through preferential adsorption of the Mg^{2+} ions to the active growth sites of calcite (Folk, 1974; Berner, 1975) and impedes any further growth and therefore increases the solubility of Mg-calcite compared to pure calcite (Nielsen et al., 2013). The solubility of calcite with a magnesium content greater than 4 mol% is reported to steadily increase with increasing Mg content (Mackenzie et al., 1983), and magnesium calcite with a magnesium content larger than 12 mol% is said to have a higher solubility than aragonite (Andersson et al., 2008). The stromatolitic sublayers in this study are found to have a magnesium content larger than 12 mol% when high-Mg calcite content exceeds 90 wt.% (Table 4-2). As a result, the high-Mg calcite of the sublayers is expected to have a higher solubility than aragonite. However, partially dehydrated magnesium ions cannot be incorporated into the denser structure of aragonite (compared to calcite) and thus aragonite growth cannot be inhibited by high Mg concentrations (Berner, 1975; Loste et al., 2003). According to experimental studies, aragonite can form at room temperature in the presence of a high concentration of Mg (typically above ~10 $mmolL^{-1}$) (Arp et al., 2001; Pentecost, 2005). The averaged Mg^{2+} concentration of the Storr's Lake water is 61 $mmolL^{-1}$, which favors the formation of aragonite. Therefore, high-Mg calcite appears to be a metastable phase compared to aragonite (more stable) in Storr's Lake water.

The initial Mg/Ca molar ratio of solutions plays a vital role in controlling the mineralogy of the carbonates as evidenced by low temperature precipitation experiments. In solutions with a Mg/Ca molar ratio less than 2, calcite was the dominant mineral and its abundance increased with saturation states (Choudens-Sanchez and Gonzalez, 2009).

However, in a solution with an initial Mg/Ca molar ratio larger than 2, only aragonite was found to precipitate (Wang et al., 2012). The two experiments were both conducted under the condition that the initial solutions were supersaturated to both high-Mg calcite and aragonite. Storr's Lake water samples collected in this research have a relatively constant Mg/Ca molar ratio of 4.5 (Table 4-1). Therefore, it is reasonable to hypothesize that Storr's Lake water favors the precipitation of aragonite rather than high-Mg calcite under the condition without microbial metabolism influence. This hypothesis is consistent with previous finding that the bottom, calcified, ground substrate of the lake, where the stromatolitic knobs develop, is aragonitic in composition (Paul et al., 2016).

Microbial mat and organic matrix: The microbial mat and its integral part extracelluar organic matter (EOM) matrix provide nucleation sites, which is essential for the precipitation of carbonate in microbialite (Dupraz and Visscher, 2005). The EOM matrix possesses negatively charged functional groups capable of binding Ca^{2+} or Mg^{2+} ions, and thus provides location for carbonate minerals to nucleate and grow (Dupraz et al., 2009). The metabolic degradation of EOM (normally anaerobic respiration) releases the bound cations. EOM degradation can also increase the alkalinity (e.g., through SRB metabolism; Visscher et al., 2000; Dupraz and Visscher, 2005). This simultaneous increase in the calcium (and/or magnesium) concentration and the alkalinity results in carbonate precipitation and is important in the formation of open-marine stromatolites (Reid et al., 2000; Visscher et al., 2000) and hypersaline microbialites (Jonkers et al., 2003; Dupraz et al., 2004; Vasconcelos et al., 2006).

In addition to liberating Ca^{2+} and HCO_3^- during microbial alteration, EOM itself can influence chemical gradients that affect the mineral phase. The EOM matrix can reduce the mobility of hydrated Mg^{2+} (8 Å diameter) relative to hydrated Ca^{2+} (6 Å diameter). The delay of Mg diffusion would lead to an initial Ca-enrichment, decreasing

the Mg:Ca molar ratio of the microenvironment inside of the EOM (Verrecchia et al., 1995). As a result, changes in the amount or type of EOM could influence the rate of precipitation or types of crystals formed, as was observed in an increase in magnesium content in sequential lithified layers of mats in Lagoa Vermelha, Brazil (Vasconcelos et al., 2006).

Different types of microbial metabolism activities occurring within microbial mat may also play a role in influencing the carbonate mineralogy. Sulfate ions occur in the solution as a magnesium-sulfate (Mg^{2+}-SO_4^{2-}) ion pair and thus decrease the availability of magnesium ions (Vasconcelos and McKenzie, 1997; Warthmann et al., 2000). Gene analysis (16S rRNA) by Paul et al. (2016) found that purple sulfur bacteria (Gammaproteobacteria) and green non-sulfur bacteria (Chloroflexi) dominant in the microbial mat near the surface, whereas SRB was found to become abundant at the deeper levels (see detailed description of the microbial community distribution in the next subsection). This vertically organized sequence was consistent with previous studies (Nicholson et al., 1987; Overmann and van Gemerden, 2000). Both anoxygenic photosynthesis of green non-sulfur bacteria and sulfide oxidation of purple sulfur bacteria produce sulfate ions that promotes the association of the Mg^{2+}-SO_4^{2-} ion pair within the microbial mat. As a result, it is highly possible that the Mg/Ca molar ratio of the microenvironment drops below 2 (from 4.5) and favors the precipitation of high-Mg calcite over aragonite which explains the observed dominance of high-Mg calcite in the surficial crusts. At deeper depth, with the increase of sulfate reducing activity, sulfate ions are consumed and thus dissociate the Mg^{2+}-SO_4^{2-} ion pair, which increases the Mg/Ca molar ratio within the microbial mat. When the Mg/Ca molar ratio of the microenvironment increases to over two via this mechanism, aragonite becomes the initial precipitated mineral. This mechanism (Greer et al., 2015) is able to explain the aragonite-rich core

zones of the two studied stromatolitic knobs. Therefore, the microbial mat and EPS matrix indirectly affect the carbonate mineral phase through altering the availability of Mg^{2+} ions and thus the Mg/Ca molar ratio within the microenvironment.

Organomineralization and Laminae Formation

Microbial Community Distribution

Cultivation-independent microbial diversity analyses were conducted on the five different types of microbial mats form Storr's Lake (calcareous knob, plateau-mushroom, pinnacle mound, cauliflower-top mushroom shaped, and cheesecake) by Paul et al. (2016). The study found that only 24% of the recovered communities were shared among all five types of microbial mats, suggesting those microbial mats displayed high diversity. The plateau-mushroom microbial mat was most similar to the shallow-water calcareous knob in terms of microbial population, whereas the deep-water pinnacle mound clustered closely with the cauliflower-top microbial mat (Figure 2-5).

Paul et al. (2016) found that the microbial composition of the five types of mats fell into 12 major bacterial phyla and 2 unclassified bacterial groups with the plateau-mushroom having the entire 14 categories and pinnacle mound having only 10 categories. The unclassified microbial communities consist of a relatively main portion of the entire microbial population for the two microbial mats (20-23% for pinnacle mound and 32-35% for plateau-mushroom; percent denotes relative abundance of the total microbial population). Chloroflexi, which belongs to green non-sulfur bacteria, was found to comprise nearly half of the whole bacterial population of the pinnacle mound, whereas plateau-mushroom had around 16-20% of Chloroflexi (Figure 2-5). Another main bacteria community was the class Deltaproteobacteria (including several types of SRB). The plateau-mushroom type had 10-12% Deltaproteobacteria, whereas 5% of Deltaproteobacteria was found to occur in the pinnacle mound type. Members of purple

sulfur bacteria belonging to the class Gammaproteobacteria were detected in minor proportions of the whole bacterial population for both plateau-mushroom and deep-water pinnacle mound types. In all the five mat types, cyanobacteria were generally low in abundance ranging between <1.0% to 3.0% (highest levels were observed in shallow-water calcareous knobs). Less than 1.0% and ~0.01% of cyanobacteria were detected in plateau-mushroom and pinnacle mound types, respectively. The almost absence of cyanobacteria might be ascribed to high concentration of HS^- ions which were found to be poisonous to cyanobacteria but did not affect Chloroflexi (Giovannoni et al., 1987).

In general, for plateau-mushroom and pinnacle mound microbial mats, filamentous Chloroflexi and purple sulfur bacteria act as the photosynthetic members under the anoxygenic environments (Imhoff, 2006), whereas heterotrophic SRBs consume organic matter by anaerobic respiration. As mentioned in the previous discussion section, the microbial communities formed a vertically organized structure, where Chloroflexi and purple sulfur bacteria grouped at the surface of plateau-mushroom and pinnacle mound stromatolitic knobs whereas SRB dominated in the core laminated zones of the two types of stromatolitic knobs (Dupraz et al., 2009; Paul et al., 2016).

Organomineralization Processes

The complex interactions between microbial mats and the surrounding environments dominate the production of organo-carbonates. The microbial metabolism occurring within the microbial mats may alter the conditions of the microenvironment (e.g., change pH values and/or influence the availability of ions) and thus indirectly affect the mineral products including mineral composition and crystallography (Dupraz et al., 2009). The controls that metabolic activity has on carbonate organomineralization can be summarized as two closely coupled mechanisms following Dupraz et al. (2009): 1) alkalinity engine and 2) production and degradation of EOM matrix that can affect the

mineral nucleation. *Alkalinity engine* Carbonate precipitation is dominated by carbonate alkalinity and the availability of free cations (Ca^{2+} and Mg^{2+}). The relationship can be expressed by the saturation index, which is expressed as:

$$SI = \log (IAP/K_{sp}) \quad (5\text{-}1)$$

Where IAP represents the ion activity product ($[Ca^{2+}]\times[CO_3^{2-}]$) and K_{sp} denotes the solubility product of the corresponding mineral (Stumm and Morgan, 1996). The solubility products for calcite and aragonite are $10^{-6.37}$ and $10^{-6.19}$, respectively, under the condition of 25 °C, 1 bar atmospheric pressure and 35 PSU salinity (Zeebe and Wolf-Gladrow, 2001). When IAP> K_{sp}, the solution is supersaturated. Experimental studies showed that $CaCO_3$ precipitated spontaneously when SI>0.8 (Kempe and Kazmierczak, 1994), while the experiments by Arp et al. (2001) found that initial 10-fold calcite supersaturation is necessary for any cyanobacterial biofilm calcification. The $[CO_3^{2-}]$ depends on the chemical equilibrium of the following reactions:

$$H_2CO_3 \leftrightarrow HCO_3^- \leftrightarrow CO_3^{2-} \quad (5\text{-}2)$$

which has a pK_a of 5.9 and 8.9, respectively, under the condition of 25°C, 1 bar atmospheric pressure and 35 PSU salinity (Zeebe and Wolf-Gladrow, 2001). Carbon dioxide (CO_2) dissolution in water leads to the formation of H_2CO_3. Carbonate alkalinity ($[HCO_3^-]+2[CO_3^{2-}]$) is approximately equal to the total alkalinity ($[HCO_3^-]+[CO_3^{2-}]$, also known as dissolved inorganic carbon) in most natural water considering the low concentration of CO_3^{2-} ions. Assuming enough $[Ca^{2+}]$ is available, an increase in alkalinity (normally also an increase in pH) will consequently result in higher SI which favors carbonate precipitation.

Organomineralization Processes of Stromatolitic Knobs: Anoxygenic phototrophs (Chloroflexi and purple sulfur bacteria) within the microbial mat of the pinnacle mound

and plateau-mushroom types use sulfide as the electron donor to fix CO_2 in organic matter. The microbial reaction is simplified as:

$$HS^- + 2CO_2 + 2H_2O \rightarrow 2CH_2O + SO_4^{2-} + H^+ \quad (5\text{-}3)$$

where the produced proton consumes either HCO_3^- or CO_3^{2-} and thus decreases the alkalinity, inhibiting carbonate precipitation. The generated organic matter appears as extracellular organic matter (EOM) that is comprised of EPS and its hydrolysis product, low-molecular-weight organic compounds (LMWOC). The filamentous Chloroflexi and coccoid purple sulfur bacteria are embedded in the EPS matrix. The acidic functional groups of the EPS bind Ca^{2+} or Mg^{2+} ions from the surrounding domain and then the EPS-Ca (or Mg) group combines LMWOC to form a bidentate complex (EPS-Ca (Mg)-LMWOC; Braissant et al., 2009), which renders cations unavailable for carbonate precipitation (Figures 5-12A and 5-12B). However, the sequestration of cations by EPS matrix creates the condition for carbonate mineral nucleation (Dupraz et al., 2009).

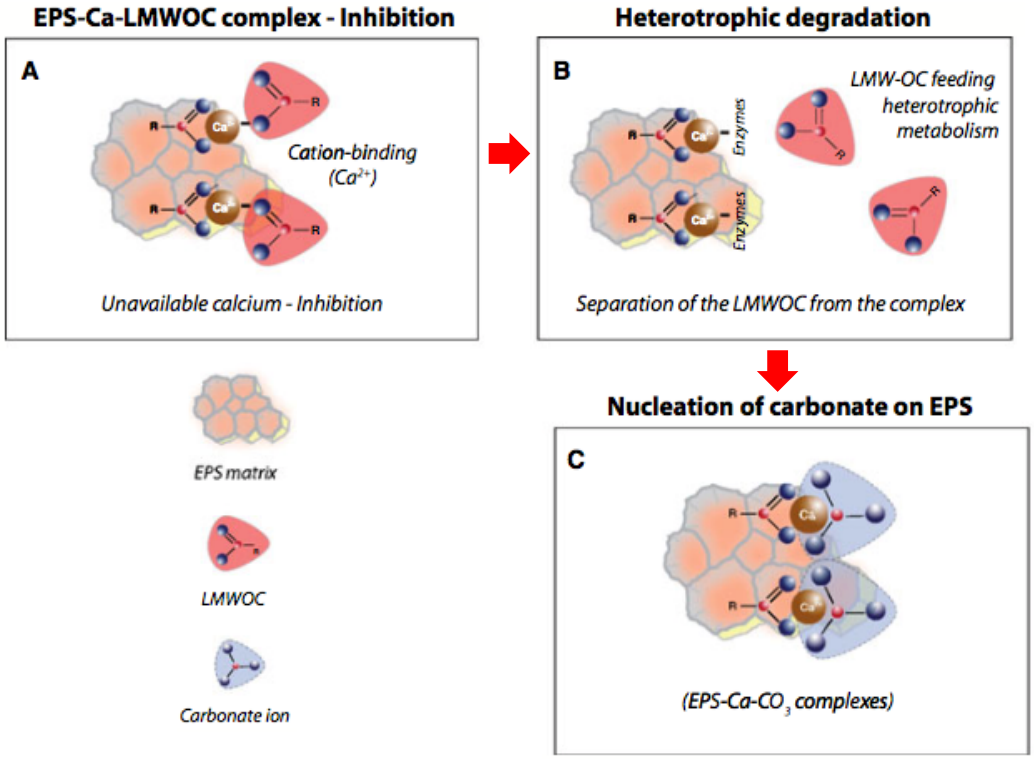

Figure 5-12 Conceptual model of EOM-influenced carbonate mineral nucleation through interactions between EPS and LMWOC. (A) Inhibition phase: EOM (comprised of EPS and LMWOC) inhibits precipitation by binding Ca^{2+} to the acidic functional groups of the EPS. The EPS-Ca group can then form a bidentate complex with LMWOC (EPS-Ca-LMWOC; Braissant et al., 2009) rendering calcium unavailable for precipitation; (B) Heterotrophic degradation phase: LMWOC is removed from the EPS-Ca-LMWOC complex through heterotrophic microbial degradation; (C) nucleation phase: The EPS-Ca complex that remains is available for carbonate nucleation, which forms a new bidentate complex (EPS-Ca-CO_3). Adapted from Dupraz et al. (2013).

Within the same microbial mat, anaerobic heterotrophs (mainly SRBs) become abundant and active at a deeper horizon and utilize LMWOC (SRBs are unable to directly use EPS) to reduce sulfate ions (Dupraz et al., 2013). The metabolic reaction is denoted as:

$$2C_2H_5O_3^- + 3SO_4^{2-} \rightarrow 3HS^- + 6HCO_3^- + H^+ \quad (5\text{-}4)$$

where the addition of one H^+ ion is offset by six HCO_3^- ions, therefore, the net production of five HCO_3^- ions increases alkalinity that favors carbonate precipitation (Dupraz et al., 2013). In addition, the heterotrophic microbial degradation removes LMWOC portion from the EPS-Ca (Mg)-LMWOC complex. Then the remaining EPS-Ca (Mg) complex becomes available for carbonate nucleation through forming a new bidentate complex (EPS-Ca (Mg)-CO_3; Figure 5-12C). The progression of EPS hydrolysis and the subsequent heterotrophic degradation of LMWOC support gradual replacement of EPS alveolar structure with carbonate, which is supported by the previous SEM analysis (Dupraz et al., 2004).

As mentioned previously, the mobility of hydrated Ca^{2+} and Mg^{2+} ions within microbial mat is different, with smaller hydrated Ca^{2+} ions moving faster. Although the anaerobic respiration of SRBs consumes sulfate ions and dissociates the Mg^{2+}-SO_4^{2-} ion pair, the delay of hydrated Mg^{2+} ions diffusion would still result in EOM matrix binding more Ca^{2+} ions (Dupraz and Visscher, 2005). The initial Ca-enrichment decreases the Mg/Ca molar ratio of the bound cations on the EOM matrix. Considering the original lake water has an average Mg/Ca molar ratio of 4.5, the decreased Mg/Ca molar ratio (might drop from 4.5 to below 2) is favorable for high-Mg calcite precipitation rather than low-Mg calcite precipitation (requiring Mg/Ca molar ratio lower than 0.25; Morse et al., 1997). The pivotal role of sulfate reducing activities in promoting initial high-Mg calcite formation has been demonstrated in both natural biogenic carbonates (Dupraz et al., 2004; Braissant et

al., 2007; Gallagher et al., 2012) and laboratory culture experiments (Van Lith et al., 2003).

The progressive precipitation of high-Mg calcite gradually replaces EOM matrix (EOM amount decreases) and increases the Mg/Ca molar ratio within the microbial mat by reducing the concentration of hydrated Ca^{2+} ions. As a result, more hydrated Mg^{2+} ions are bound on the residue EOM matrix and Mg/Ca molar ratio of the bound cations on EOM matrix increases. The incorporation of Mg^{2+} ions into the calcite lattice poisons the early stage high-Mg calcite crystallites and prevents their further growth. When the Mg/Ca molar ratio of the microbial mat reaches two or higher, the microenvironment promotes the phase transformation from metastable high-Mg calcite to aragonite. The phase transformation is dominated by the dissolution of high-Mg calcite followed by the crystallization of aragonite. It is proposed that the nucleation of aragonite nanocrystallites occurs beneath the surface of the high-Mg calcite rhombohedral particles. The monocrystalline-like aragonite rods with a higher density than high-Mg calcite gradually grow larger at the expense of the rhombohedral high-Mg calcite nanocrystallites. Finally, when all the high-Mg calcite nanocrystallites are completely consumed, sheaf-like clusters of pure aragonite rods result. The phase transformation processes are summarized by six major steps as shown in Figure 5-13. The proposed transformation model is consistent with a study on active-forming hot spring travertines (Greer et al., 2015), which observed mineralogy transformation from high-Mg calcite crust to aragonitic core just like the mineralogy distribution of stromatolitic knobs in this research.

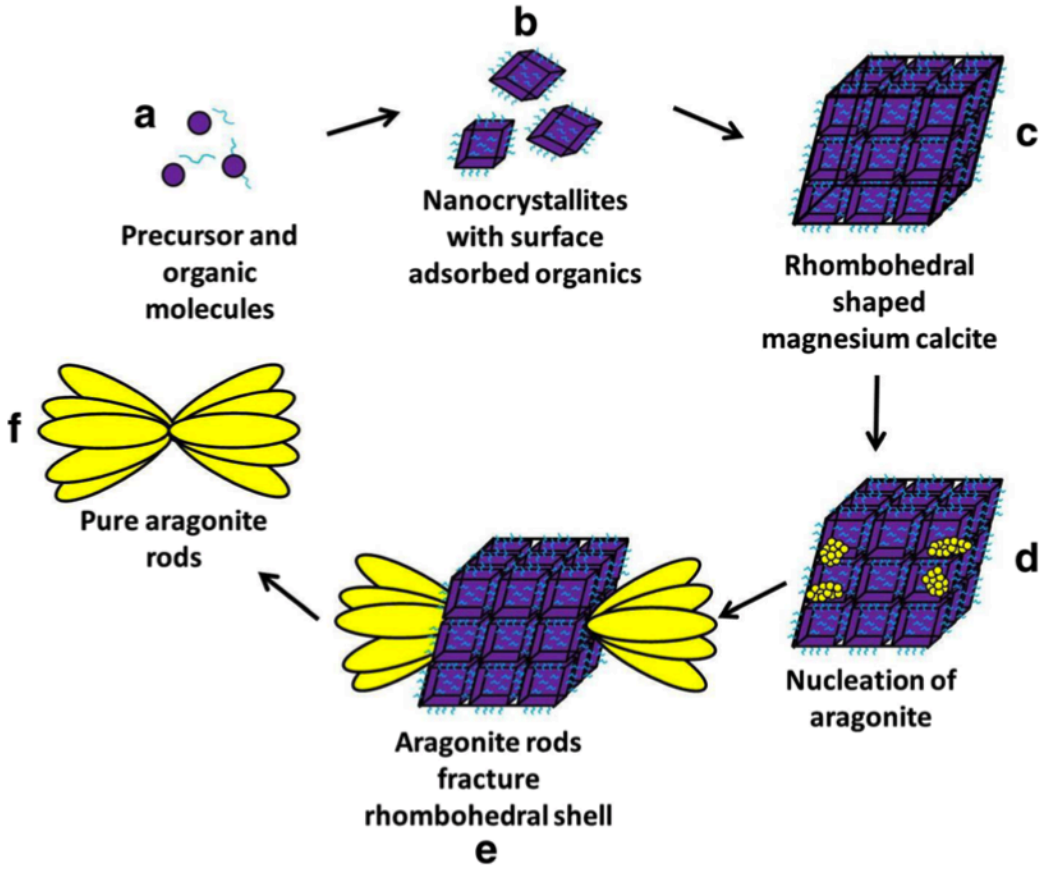

Figure 5-13 Schematic drawing of the proposed formation mechanism of the stromatolitic knobs and the phase transformation from high-Mg calcite to aragonite. From Greer et al. (2015)

Laminae Formation of Stromatolitic Knobs

The slightly positive $\delta^{13}C$ signature of the initial precipitate can be explained by a ^{13}C enrichment of the DIC in the vicinity of active anoxygenic phototrophs that preferentially take up the light ^{12}C isotope during photosynthesis (e.g., Merz-Preiß, 1992; Dupraz et al., 2013). As the structure grows with a new layer at the surface, the precipitate is moved downward, but the organomineralization processes associated with this precipitate does not stop. The continuing alteration of the EOM matrix by

heterotrophic activity at deeper horizons in the stromatolitic knob may further skew the C isotopic values toward more negative, explaining the C isotopic signature in this study (Figures 4-15 and 4-16). The $\delta^{18}O$ values of stromatolite sublayers in this study cluster around 1‰, which is the same as the $\delta^{18}O$ values of stromatolite heads in Paull et al. (1992), but slightly heavier than the oxygen isotopic compositions of stromatolite laminae (around 0‰) in Dupraz et al. (2013). In our study, we did not analyze the oxygen isotopic compositions of lake water, however, Paull et al. (1992) reported the $\delta^{18}O$ values of lake water samples from the northern, central, and southern parts of the Storr's Lake were 3.2, 3.0, and 2.8‰, respectively. Using the temperature equation of Craig (1965), Paull et al. (1992) further estimated the temperature at which the stromatolite carbonate precipitated was 25.1 ºC (assuming equilibrium precipitation), which was consistent with the average temperature of lake water in our study (25.9 ºC). Therefore, it is reasonable to assume that the oxygen isotopic compositions of stromatolitic sublayers in this study are in equilibrium with the lake water.

Besides the effects of microbial activities, mineralogy also plays a role in affecting carbon and oxygen isotopes in carbonates. Isotopes of carbon and oxygen were found to fractionate differently in calcite and aragonite due to differences in the internal vibrational frequencies of the polymorphs' carbonate ions (Rubinson and Clayton, 1969; Tarutani et al., 1969). For $CaCO_3$ precipitated at 25 °C from artificial seawater, $\delta^{18}O$ and $\delta^{13}C$ are enriched in the aragonite polymorph by 0.6‰ and 1.8‰, respectively, relative to the calcite polymorph. $\delta 1^{8}O$ is also enriched in high-Mg calcite (12.8 mol% Mg) by 1.1‰ relative to pure calcite, indicating a 0.09‰ enrichment in $\delta^{18}O$ per mol% Mg (Rubinson and Clayton, 1969).

In Dupraz et al. (2013), carbon isotope compositions of the well-developed and subfossil knobs were compared with that of the deeper layers of the young, active knobs.

The similar $\delta^{13}C$ signatures of the subfossil knobs and young knobs suggested that early diagenetic processes can rapidly alter the $\delta^{13}C$ biosignature of the initial precipitation and important geochemical information is likely lost deeper in the structure while the stromatolite is still actively accreting. The pinnacle mound and plateau-mushroom stromatolitic knobs in this study belong to “well-developed and subfossil knobs” (Paul et al., 2016), therefore, the primary $\delta^{13}C$ signature may have been modified due to early diagenesis.

The research of well-developed stromatolitic knobs in this study (pinnacle mound and plateau-mushroom) are combined with the finding of young, active knobs (similar to calcareous knobs in Paul et al. 2016) in Dupraz et al. (2013) to discuss the lamination formation processes for the microbialites in Storr’s Lake. The young, metabolically active knobs are quintessential examples of emerging morphologies that are dominated by microbial processes. The fine lamination of active knobs (composed of micritic layers) can be well modeled by using diffusion-limited aggregation (DLA) combined with cellular automata (CA) (Dupraz et al., 2006). The modeling results indicate an increase in irregularly spaced layering forms with time after an initial stable phase of regular lamination. The chaotic behavior might be ascribed to an increase in water turbidity and/or depth. With increasing water depth or turbidity, the accommodation space increases, and the control of light on the orientation of filamentous microbial communities weakens, both of which result in regular lamination disappearing. Therefore, the main microbial pathway in the upper layer of the mat is shifting from a net phototrophic to a net heterotrophic system, and the dominant mesostructured changes from laminated to clotted. This change in structure type could explain the formation of pinnacle mound and plateau-mushroom growth as seen in this study (bulbous crust at the top with delicate laminae in the bottom). Also, the association of large voids with the bulbous crust can be

explained by microbialite undergoing random and episodic growth with increasing accommodation space at deeper water depth.

Mg Isotopic Compositions of Stromatolitic Sublayers

Mineralogy Control on Mg Isotopic Values

The Mg isotopic compositions of stromatolitic sublayers (δ^{26}Mg values ranging from -3.04‰ to -2.33‰) fall within the range of previously reported δ^{26}Mg values for carbonates (Figure 5-8). The δ^{26}Mg values of high-Mg calcite (HMC) sublayers are generally lighter than that of aragonitic sublayers, which is consistent with the relationship between δ^{26}Mg measured in biogenic high-Mg calcite and biogenic aragonite (Figure 5-14).

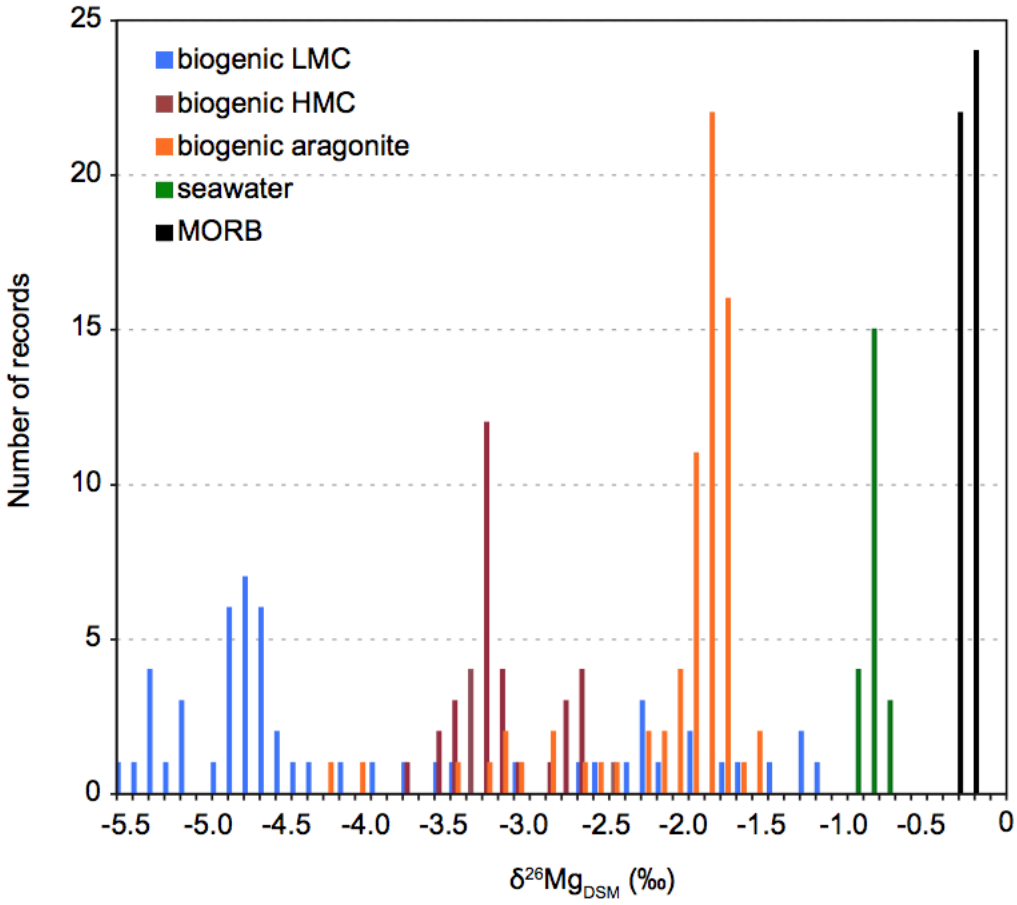

Figure 5-14 Histogram of $\delta^{26}Mg$ values in biogenic low magnesium calcite (blue), high magnesium calcite (red) and aragonite (orange), compared with those for seawater (green) and mid-ocean ridge basalts (MORB, black). The biogenic carbonate data in this plot are from Saenger and Wang (2013). Seawater data are from Foster et al. (2010) and MORB data are from Teng et al. (2010). All values are expressed relative to DSM. Figure from Saenger and Wang (2014).

The sublayers from the pinnacle mound and plateau-mushroom types with similar mineralogical compositions have identical $\delta^{26}Mg$ values, which indicates that the morphological type of the two stromatolitc knobs in this study does not affect the Mg isotopic compositions of their sublayers. The $\delta^{26}Mg$ values of stromatolitic sublayers

show a decreasing trend with Mg/Ca molar ratios (Figure 5-15A) and an increasing trend with Sr/Ca molar ratios (Figure 5-15B) and weight percentage of aragonite (Figure 5-15C), which indicates a mineralogical control on the Mg isotopic compositions of stromatolitic sublayers by mixing of different proportions of isotopically light high-Mg calcite (low Sr concentration) with isotopically heavy aragonite (high Sr concentration). However, no correlation was observed between the δ^{26}Mg values of stromatolitic sublayers and their carbon isotopic compositions (Figure 5-15D).

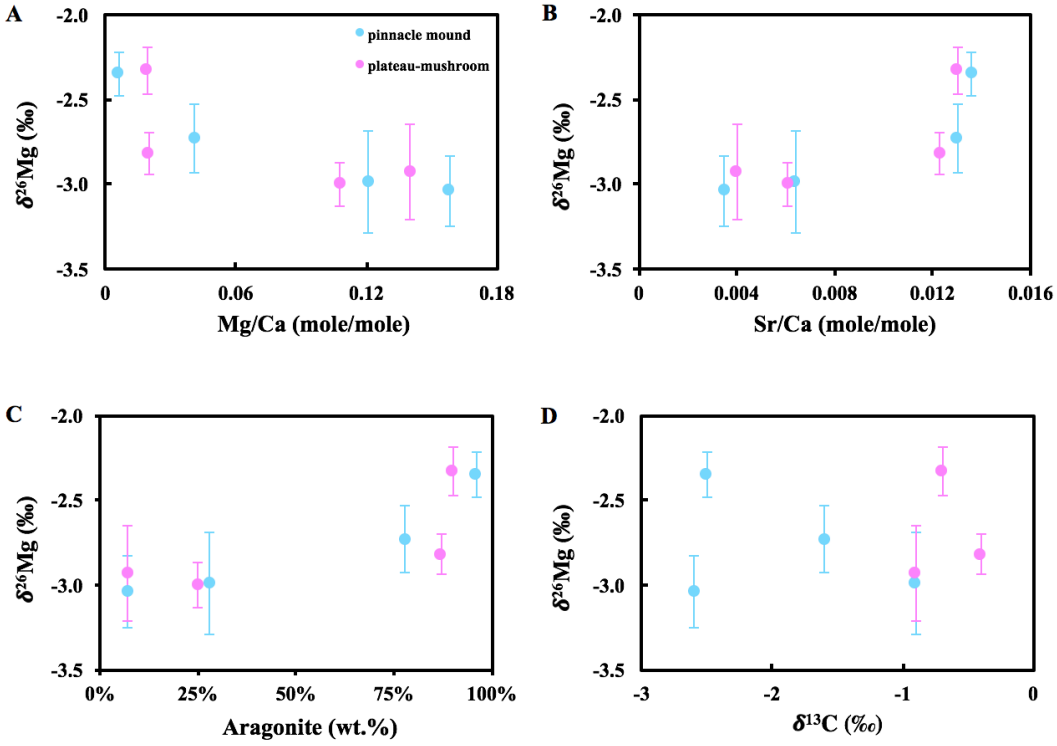

Figure 5-15 Cross plots of (A) δ^{26}Mg versus Mg/Ca molar ratio, (B) δ^{26}Mg versus Sr/Ca molar ratio, (C) δ^{26}Mg versus wt.% aragonite from XRD, and (D) δ^{26}Mg versus δ^{13}C. Blue dots represent sublayers (WS1-i, WS1-1, WS1-6, and WS1-9) from pinnacle mound and pink dots represent sublayers (WN7-i, WN7-ii, WN7-1, and WN7-3) from plateau-mushroom

In order to test mineralogy control, a two end-member (pure high-Mg calcite and pure aragonite) mixing model was applied to discuss the controls on Mg isotopic compositions of stromatolitic sublayers. First, the wt.% Mg of hypothetical pure high-Mg calcite and pure aragonite was calculated, which was based on the results of mineralogical composition and elemental analysis of stromatolitic sublayers (Table 4-2). In this study, two sublayers were chosen from a pinnacle mound type which were WS1-1 (high-Mg calcite rich) and WS1-9 (aragonite rich) and two linear equations were constructed with the wt.% Mg and mineralogical composition of the two sublayers. The results suggest that the wt.% Mg for pure high-Mg calcite and pure aragonite are 3.3% and 0.1%, respectively, which were consistent with published values (Finch and Allison, 2008). Secondly, the δ^{26}Mg values of the two end members were determined. For pure high-Mg calcite end member, WS1-i was chosen (having the most negative δ^{26}Mg value and the highest wt.% high-Mg calcite). Because the high-Mg calcite was calculated to contribute 99.77% of the whole Mg content of WS1-i, it was reasonable to assume the δ^{26}Mg value of the WS1-i (-3.04‰) can roughly represent the δ^{26}Mg value of pure high-Mg calcite. However, it was not correct to choose a δ^{26}Mg value of WS1-6 (having wt.% aragonite of 96%) as the δ^{26}Mg end member for pure aragonite, because aragonite was calculated to contribute only 42.11% of total Mg of this sample. Therefore, a δ^{26}Mg value of -1.70‰, which was the most reported value for natural biogenic aragonite (Saenger and Wang, 2014), was regarded as the δ^{26}Mg end member of pure aragonite. As a result, a mixing trend was calculated and illustrated in Figure 5-16. It seemed that the mixing trend fitted most data except one aragonitic sublayer of plateau-mushroom which had a heavier δ^{26}Mg value than the mixing model suggested. Consequently, it is reasonable to assume the end member high-Mg calcite and aragonite mixed in the stromatolitic

(pinnacle mound and plateau-mushroom) sublayers have δ^{26}Mg values of -3.04‰ and -1.70‰, respectively.

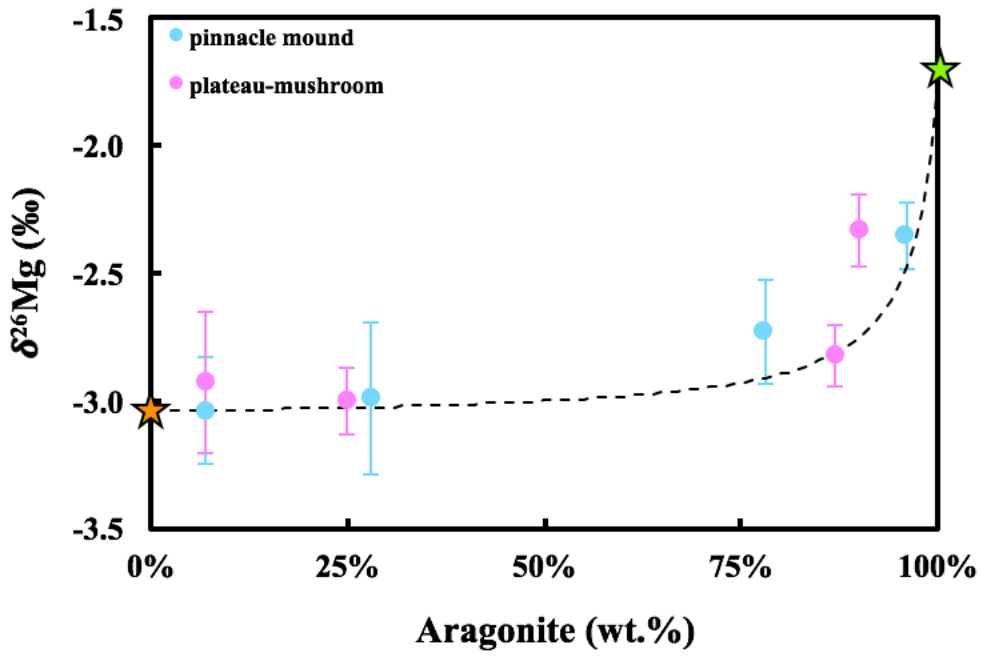

Figure 5-16 Cross plot of δ^{26}Mg versus wt.% aragonite from XRD. Blue dots represent sublayers (WS1-i, WS1-1, WS1-6, and WS1-9) from pinnacle mound and pink dots represent sublayers (WN7-i, WN7-ii, WN7-1, and WN7-3) from plateau-mushroom. The dotted line represents the mixing trend from the two end members. Orange pentagram represents pure high-Mg calcite end member with wt.% Mg of 3.3% and δ^{26}Mg value of -3.04‰, whereas the green pentagram represents pure aragonite end member with wt.% Mg of 0.1% and δ^{26}Mg value of -1.70‰. The δ^{26}Mg value of pure aragonite is from Saenger and Wang (2013).

Mg Isotope Fractionation During Organomineralization

The $\Delta^{26}Mg_{carbonate\text{-}lake\ water}$ values of sublayers from pinnacle mound and plateau-mushroom range from -2.24‰ to -1.55‰ and from -2.11‰ to -1.51‰, respectively (Figure 5-17). In the following section, $\Delta^{26}Mg_{carbonate\text{-}lake\ water}$ values of two end members

(hypothetical pure high-Mg calcite and pure aragonite) were compared with the fractionation values derived from biogenic carbonates and inorganic precipitation experiments, and their implications were discussed.

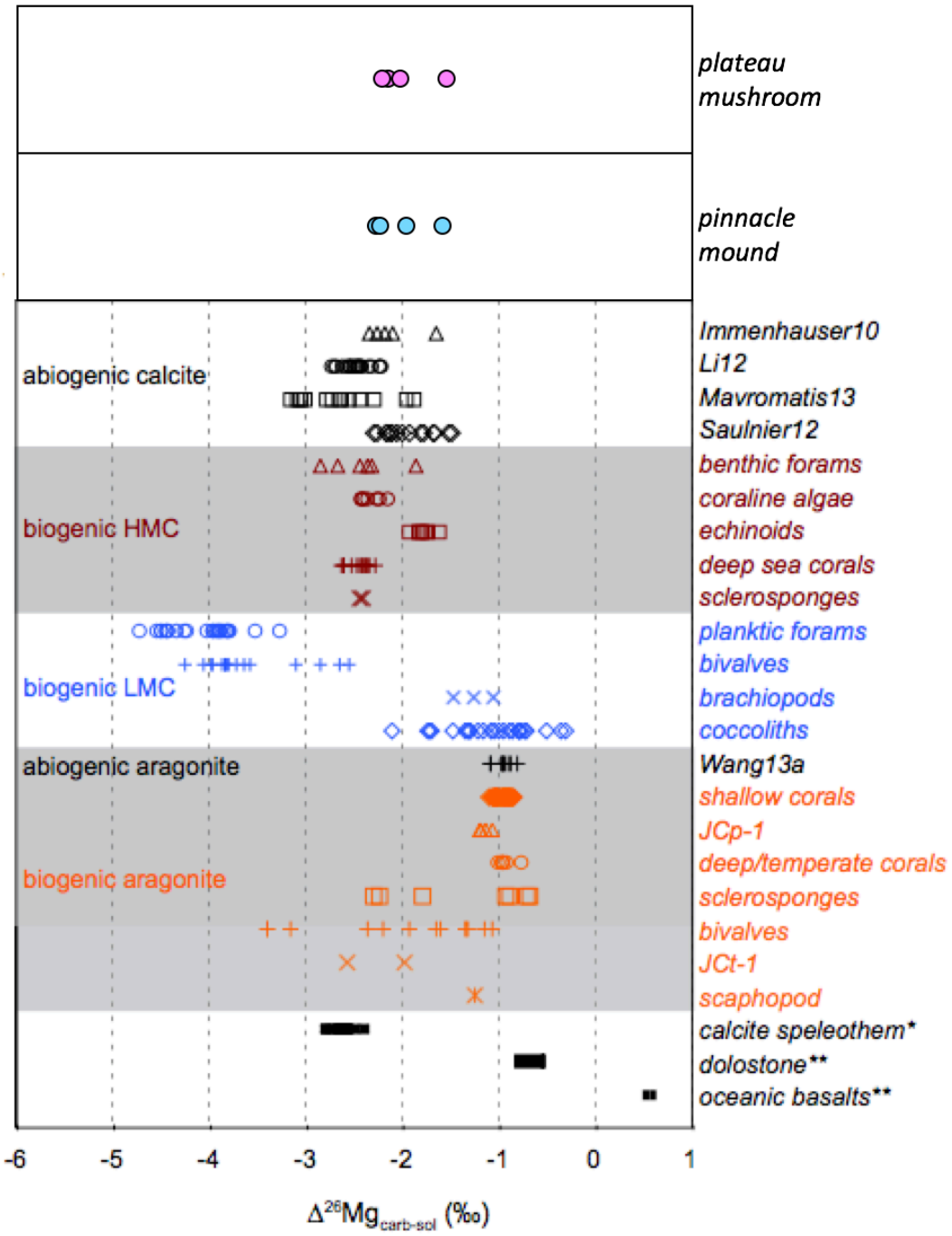

Figure 5-17 Comparison of $\Delta^{26}Mg_{carbonate\text{-}lake\ water}$ of stromatolitic sublayers in this study with $\Delta^{26}Mg_{carb\text{-}sol}$ values of various high-Mg calcite (red), low-Mg calcite (blue) and

aragonite (orange) in comparison with abiogenic experiments. Blue dots represent pinnacle mound sublayers and pink dots represent plateau-mushroom sublayers in this study. Abiogenic and biogenic data are from Saenger and Wang (2013). Also shown are the typical ranges for calcite speleothems and dolostone from Galy et al. (2002); abiogenic calcite samples in Immenhause et al. (2010), Li et al. (2012), Saulnier et al. (2012), and Mavromatis et al. (2013); and oceanic basalt in Teng et al. (2010). Modified from Saenger and Wang (2014).

For a pure high-Mg calcite end member, the $\delta^{26}Mg$ value of WS1_111cm (lake water collected from the surrounding of stromatolitic knob with a temperature of 24.8ºC) was applied to calculate $\Delta^{26}Mg_{carbonate\text{-}lake\ water}$. The $\Delta^{26}Mg_{HMC\text{-}lake\ water}$ value was -2.24‰, which was 0.26‰ heavier than the $\Delta^{26}Mg_{carb\text{-}sol}$ (-2.50‰ at 24.8ºC) derived from abiogenic calcite precipitation experiments (Li et al., 2012). However, the $\Delta^{26}Mg_{HMC\text{-}lake\ water}$ value in this study falls within the range of reported $\Delta^{26}Mg_{carb\text{-}sol}$ for biogenic high-Mg calcites (Figure 5-18). Just like biogenic high-Mg calcites, the offset between the $\Delta^{26}Mg_{HMC\text{-}lake\ water}$ in this study from the abiogenic calcite in Li et al. (2012) can be interpreted as a biological vital isotopic effect. There appear to be two principle causes for biological Mg isotope effects.

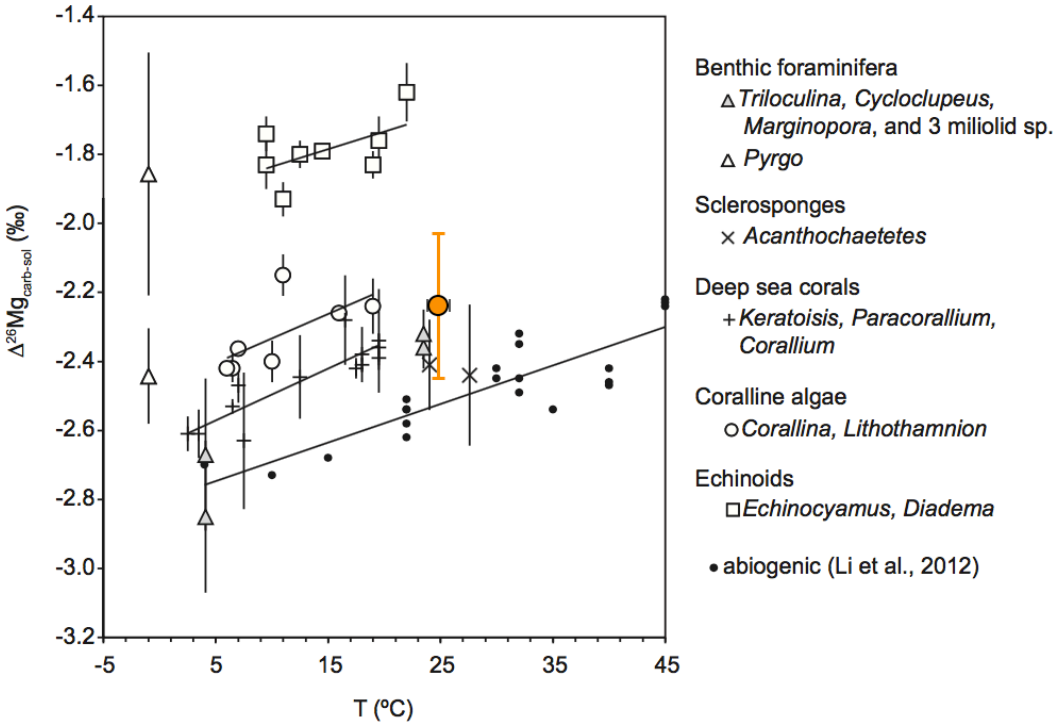

Figure 5-18 Comparison of $\Delta^{26}Mg_{HMC\text{-}lake\ water}$ of pure high-Mg calcite end member in this study (orange dot) with biogenic high-Mg calcite $\Delta^{26}Mg_{carb\text{-}sol}$ and with abiogenic experiments of Li et al. (2012). Modified from Saenger and Wang (2014).

The Mg concentration and the $\Delta^{26}Mg_{HMC\text{-}lake\ water}$ value may be affected by biomolecules at the site of precipitation. Wombacher et al. (2011) observed weaker Mg isotope fractionation in deep sea corals, coralline red algae and echinoid spines than in abiotic experimental calcite, which was ascribed to the mechanism of species specific biomolecules binding cations. Wombacher et al. (2011) argued that these organisms precipitate HMC by altering its local aqueous Mg/Ca ratio using biomolecules that lower the desolvation energy barrier for hydrated Mg^{2+} ions. It was further suggested that lowering the desolvation energy barrier reduces the Mg isotope fractionation. This hypothesis is also applicable to explain the Mg isotope fractionation behavior during the organomineralization of HMC in this study. The EOM matrix may lower the desolvation

energy barrier for Mg and thus render the smaller Mg isotope fractionation between the bound Mg in EOM matrix and the hydrated Mg^{2+} ions of the local aqueous environment. The finding by Stephenson et al. (2008) that reported higher Mg contents in calcite if peptides were present and hypothesized that peptides lower the desolvation energy barrier of Mg supports this hypothesis, because peptides are typical components that form EOM matrix (Dupraz et al., 2009). An additional possibility is that the precipitation of HMC via an amorphous calcium carbonate (ACC) transient precursor may exhibit smaller Mg isotope fractionations due to enhanced incorporation of hydrated or unfractionated Mg. Saenger and Wang (2013) observed the $\Delta^{26}Mg_{carb\text{-}sol}$ values of biogenic high-Mg calcite follow the order: benthic foraminifera (except *Pyrgo* sp.) and sclerosponges < deep sea corals < coralline algae < echinoids. This order generally matched the order of the proportion of hydrated Mg in HMC organisms derived from nuclear magnetic resonance imaging (Nebel and Epple, 2008). As a result, ACC precursor might be associated with the observed smaller Mg isotope fractionation of HMC compared to abiogenic calcite precipitation.

For a pure aragonite end member, the $\delta^{26}Mg$ value of WS1_111cm was still chosen as $\delta^{26}Mg_{lake\ water}$ to calculate $\Delta^{26}Mg_{carbonate\text{-}lake\ water}$, which was reasonable under the condition that WN7 water sample was missing and no difference in $\delta^{26}Mg_{lake\ water}$ was seen in this study between the north and the south sectors of the lake. The calculated $\Delta^{26}Mg_{aragonite\text{-}lake\ water}$ value is -0.90‰, which appeared to be within error of the value measured in abiogenic aragonites precipitated near the same temperature (Figure 5-19; Wang et al., 2013). Hippler et al. (2009) reported some shallow water corals (e.g., *Porites* sp.) had the identical $\Delta^{26}Mg_{carb\text{-}sol}$ values with the fractionation values from abiogenic aragonite precipitation experiments, which suggested that skeletogenesis in these organisms was relatively unaffected by vital effects. Therefore, the $\Delta^{26}Mg_{aragonite\text{-}lake\ water}$

signature observed in this study may also indicate the absence of biological Mg isotope effects, which is consistent with the previously proposed organomineralization process of aragonite. Aragonite precipitates under the condition that EOM matrix has been degraded by SRB to an extent that increases the Mg/Ca ratio of the local aqueous microenvironment that favors aragonite precipitation. With the EOM matrix amount dramatically decreasing, the effect of the lowering of the desolvation energy barrier for Mg isotopes becomes negligible. As a result, the aragonites in stromatolitic sublayers were proposed to result from abiogenic aragonite precipitation. Furthermore, active removal of Mg from the site of carbonate precipitation during the phase transformation from high-Mg calcite to aragonite seemed to have no effect on Mg isotope fractionation.

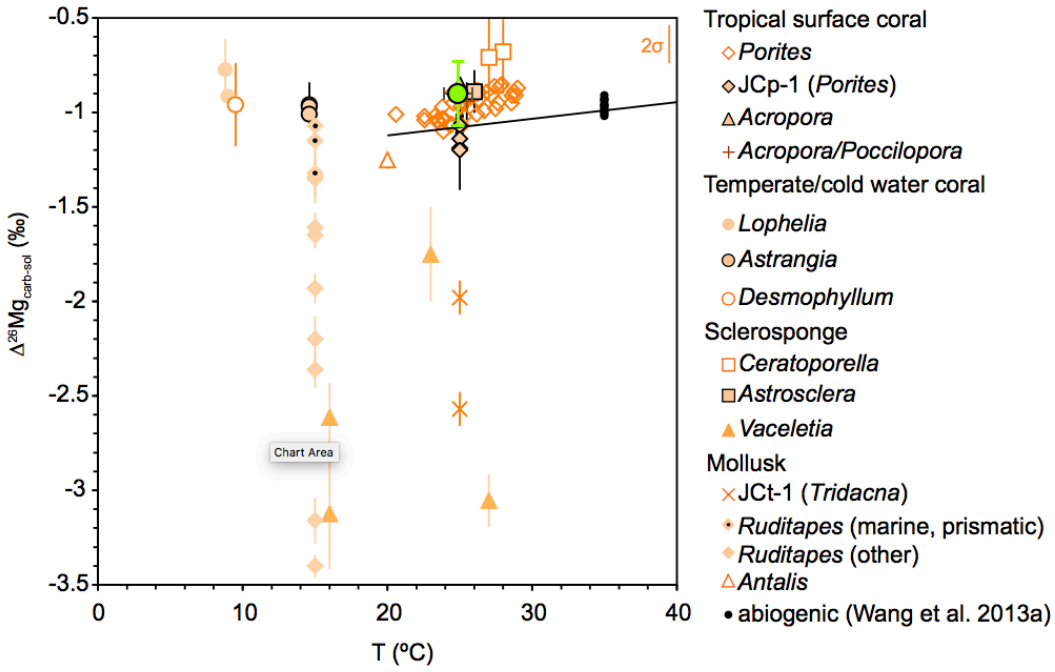

Figure 5-19 Comparison of $\Delta^{26}Mg_{aragonite\text{-}lake\ water}$ of pure aragonite end member in this study (green dot) with $\Delta^{26}Mg_{carb\text{-}sol}$ of biogenic aragonites and with abiogenic experiments (black) of Wang et al. (2013). Modified from Saenger and Wang (2014).

According to Higgins and Schrag (2012), recrystallization (diagenesis) would increase Mg isotope fractionation between carbonates and solutions. Because neither of $\Delta^{26}Mg_{HMC\text{-}lake\ water}$ and $\Delta^{26}Mg_{aragonite\text{-}lake\ water}$ was larger than the fractionation values derived from the abiogenic carbonate precipitation experiments at the same temperature, the possibility of diagenesis affecting Mg isotope fractionation was excluded, which was evidenced by the prevailing micritic structure through microscopic observation.

Comparison of Stromatolites in Different Environments

Comparisons can be made between the Storr's Lake stromatolites and the modern stromatolites from other environments to gain insight into the environmental and microbial controls on stromatolite formation (structure and organomineralization processes). The basic characteristics of stromatolites from each environment (Bahamian stromatolites in Storrs Lake, Highbourne Cay, Eleuthera, as well as the Sarine River in Switzerland) were summarized in Figure 5-20 from Fowler (2011).

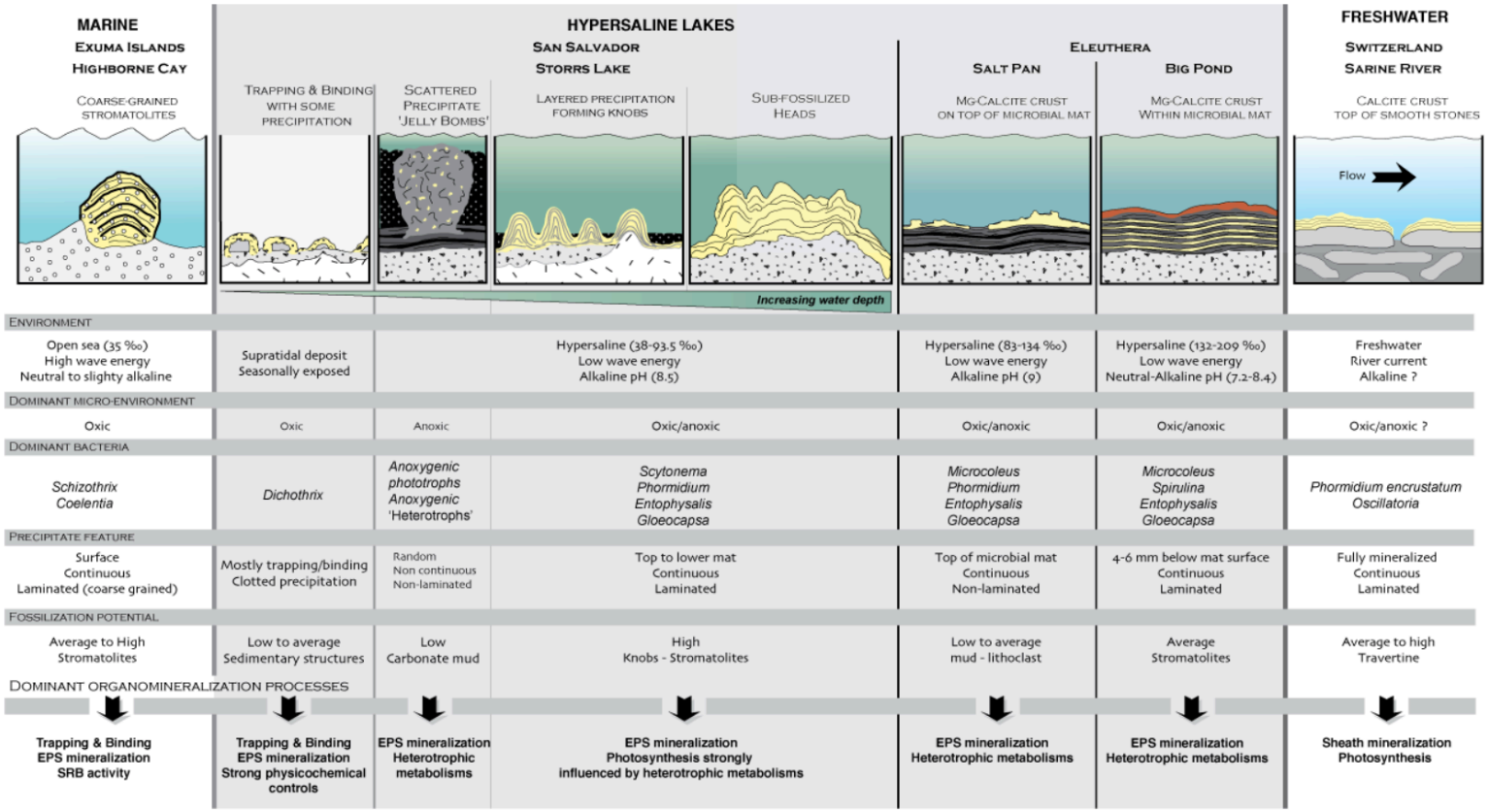

Figure 5-20 Comparison of stromatolites from hypersaline, open marine, and freshwater environments. From Fowler (2011).

Comparison of Stromatolites in Storr's Lake and Other Hypersaline Environments

The salinity of Storr's Lake (~37 PSU in winter and ~40-60 PSU in summer; Dupraz et al., 2013; Paul et al., 2016; this study) is lower than that of other lakes/ponds from the Bahamas, including Salt Pan (83-134 PSU) and Big Pond (132-209 PSU) on Eleuthera Island, Bahamas (Dupraz et al., 2004; Glunk et al., 2011). Though differences exists in salinity, the hypersaline nature of these three environments render them highly comparable to Storr's Lake. Oxygen isotopic values indicate that all of these lakes have evaporative signature, and lake water is supersaturated with respect to carbonate minerals (Dupraz et al., 2004; Glunk et al., 2011; Dupraz et al., 2013; Paul et al., 2016; this study). High-Mg calcite was found to precipitate within well-developed microbial mats in all of these environments. Only Storr's Lake was reported to have aragonite (this study; Paul et al., 2016; this study). The microbial mats of these environment share relatively equivalent functional microbial communities (cyanobacteria, chloroflexi, and sulfate-reducers) (Dupraz et al., 2004; Glunk et al., 2011; Paul et al., 2016).

The carbonate precipitation pattern in Storr's Lake is consistent with that in all other three hypersaline environments. Salt Pan and Big Pond both display a microstructure comprised of micritic micropeloidal structures surrounded by microsparite (Dupraz et al., 2004, Glunk et al., 2011), as seen in areas where EOM is degraded and replaced by high-Mg calcite for Storr's Lake stromatolitic knobs. None of these environments was found to precipitate carbonate within cyanobacterial sheaths (Dupraz et al., 2013), and heterotrophic degradation of EOM by SRB seems to be a major mechanism for carbonate precipitation in all of these environments (Dupraz et al., 2004; Glunk et al., 2011). Carbon isotope compositions show that the metabolism responsible for carbonate precipitation differs slightly among the lakes/ponds (Figure 5-21; Glunk et al., 2011; Dupraz et al., 2013; this study). Heterotrophic degradation of EOM by SRB

seems to be most dominant in Big Pond, as evidenced by the most negative $\delta^{13}C$ ratios of stromatolites (-7.2 to -1.9‰), and slightly dominant in Storr's Lake ($\delta^{13}C$ ratios of -2.6 to 1.6‰; Figure 5-21). The observed slightly positive $\delta^{13}C$ values in Storr's Lake may indicate that photosynthesis plays a more important role in carbonate precipitation in Storr's lake. Though the involvement of different types of metabolisms varies, it is proposed that both EOM degradation by SRBs and photosynthesis by cyanobacteria or anoxygenic phototrophs are active in each of these environments (Dupraz et al., 2004; Glunk et al., 2011; Dupraz et al., 2013; Paul et al., 2016; this study).

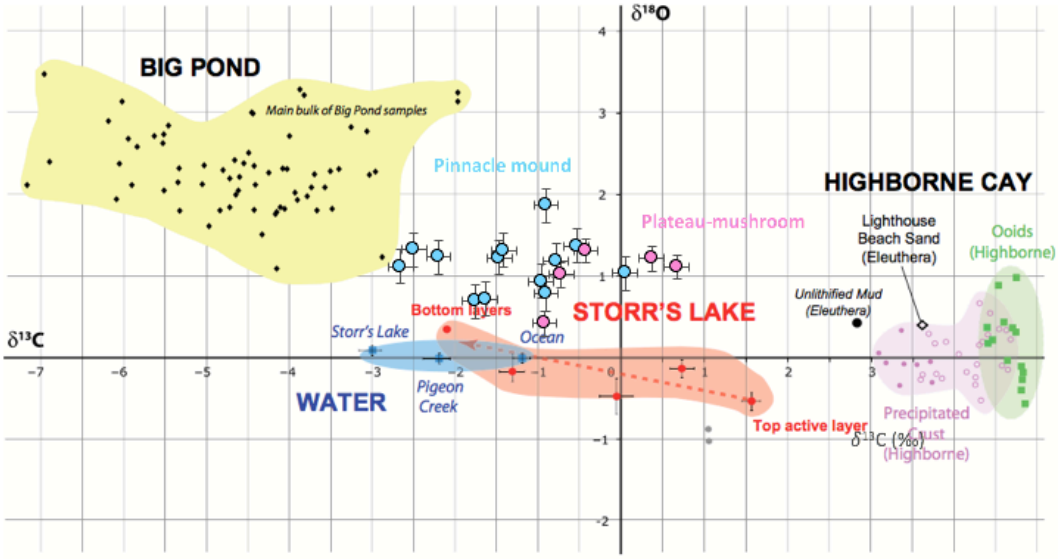

Figure 5-21 Carbon and oxygen isotopic compositions of stromatolitic sublayers from pinnacle mound and plateau-mushroom samples in Storr's Lake (this study), carbonate laminae from Storr's Lake *Scytonema* knobs and water (Dupraz et al., 2013), Big Pond stromatolites (Eleuthera Island, Bahamas; data from Glunk et al. 2011), sediment collected on Eleuthera Island (Bahamas; Dupraz et al., 2013), and precipitated micritic crust and ooids from open marine stromatolites (Highbourne Cay, Bahamas; data from Andres et al. 2006). Adapted from Dupraz et al. (2013).

The mesostructure of the mcirobialites from these hypersaline environments displays some differences. The stromatolites from Salt Pan are characterized by non-lamianted, leiolitic carbonate crust (Dupraz et al., 2004), unlike the laminated mesostructure seen in Storr's Lake and Big Pond (Glunk et al., 2011; Dupraz et al., 2013). The lamination in Big Pond is explained by periodic episodes of precipitation and non-precipitation (Glunk et al., 2011), which is different from the proposed mechanism of sequential lithification of microbial mats for Storr's Lake.

Comparison of Stromatolites in Storr's Lake and Open Marine Environments

Stromatolites from Highbourne Cay, Exuma Islands, Bahamas are regarded as representatives of modern open marine stromatolites. Although Highbourne Cay shares the same functional microbial communities (cyanbacteria and SRB) with hypersaline environments including Storr's Lake, Salt Pan, and Big Pond (Reid et al., 2000; Dupraz et al., 2004; Glunk et al., 2011; Dupraz et al., 2013; Paul et al., 2016), the stromatolite formation processes are different. During periods of high wave-energy, stromatolite formation is primarily achieved by trapping and binding of coarse-grained sediments by filamentous cyanobacteria, and in situ micrite precipitation is ascribed to the controls of photosynthesis and, more dominantly, heterotrophic metabolisms during periods of low wave-energy (Reid et al., 2000). In addition, carbonate precipitation within bored grains in the Highbourne Cay stromatolites is attributed to EOM degradation by SRBs, which is similar to the dominant mechanism of precipitation in hypersaline lakes. However, the lamination in Highbourne Cay stromatolites is ascribed to varied sedimentation rates (Reid et al., 2000), which is different from the proposed lamination mechanism in Storr's Lake.

Comparison of Stromatolites in Storr's Lake and Freshwater Environments

Stromatolites from Sarine River in Fribourg, Switzerland are regarded as representatives of modern freshwater stromatolites. The microbial communities in freshwater environment are different from those in hypersaline lakes and open marine environments. Cyanobacteria completely dominate the community functional groups in microbial mats from the Sarine River in Fribourg, Switzerland (Dupraz et al., 2009) and sulfur cycle plays a minor role under freshwater condition. It might be attributed to much lower amounts of organic matter to feed heterotrophic metabolisms in freshwater ecosystems (Dupraz et al., 2009). Cation binding by EOM matrix within microbial mats is much less in freshwater environments without a large amount of organic matter. As a result, an increase in carbonate alkalinity derived by photosynthesis leads to carbonate precipitation without impediment from EOM matrix binding cations, and without the heterotrophs degrading EOM matrix to release cations.

Therefore, the mechanism of organomineralization in freshwater environment is quite different from hypersaline lakes and open marine environments. In the freshwater scenario, carbonate precipitate within the cyanobacterial sheaths (Dupraz et al., 2009) rather than in the EOM matrix as seen in hypersaline lakes and open marine environments. Because photosynthesis is dominant in freshwater environment, the formation of laminae closely relates to alternating cyanobacterial filament orientations (Monty, 1976; Freytet and Plet, 1996; Freytet and Verrecchia, 1998; Dupraz et al., 2009); which is also seen in the young, active knobs of Storr's Lake (Dupraz et al., 2013).

Summary

The similarities and differences of the stromatolites from different environments indicate that environmental conditions and microbial metabolisms have profound effects on morphology, structure, and organomineralization processes. Environmental conditions influence the dominant metabolism that affect carbonate precipitation and the subsequent

macro- and mesostructure of the stromatolites. At Storr's Lake, water depth is a primary factor to control the macro- and mesostructure of stromatolites. Sedimentation rates may also have impact on the stromatolite morphology. These conclusions derived from comparisons may have implications for the formation of ancient stromatolites.

Chapter 6

Conclusions

This study builds upon analysis and interpretation of the hydrochemistry, the mineralogy of two types of stromatolitic mounds (pinnacle mound and plateau-mushroom), and the Mg isotope composition of lake water and stromatolitic sublayers. One of the main findings is the identification of seawater as the primary source (including Mg) for Storr's Lake water. Seawater also dominates the Mg isotope budget of the lake. Secondly, elemental analysis and Mg isotope studies suggest that major ions and Mg isotopes are spatially homogenous in Storr's Lake. Cations and anions show little seasonal variation in the north sector, whereas a significant increase in major ions concentrations was observed for the south sector waters collected in summer. Thirdly, the detailed study of the mineralogy of the stromatolitic sublayers reveals that the surficial crusts of both two stromatolites are enriched in high-Mg calcite and the weight percentage of aragonite increases inward. The proposed mineral phase transformation from high-Mg calcite to aragonite can be explained by an increase in Mg/Ca molar ratio within the stromatolitic knobs during the organomineralization process.

Furthermore, Mg isotopic investigation indicates that the $\delta^{26}Mg$ values of high-Mg calcitic sublayers are generally lighter than that of aragonitic sublayers. The Mg isotopic compositions of stromatolitic sublayers fall within the range of values previously reported for biogenic high-Mg calcite and aragonite and display strong dependence on mineral compositions. The $\Delta^{26}Mg_{carbonate\text{-}lake\ water}$ value of pure high-Mg calcite end member is more positive than the $\Delta^{26}Mg_{carbonate\text{-}solution}$ values of abiogenic calcite precipitation experiments, suggesting the vital effect on Mg isotope fractionation during the organomineralization of high-Mg calcite. However, the $\Delta^{26}Mg_{carbonate\text{-}lake\ water}$ value of pure aragonite end member is identical to the $\Delta^{26}Mg_{carbonate\text{-}solution}$ values of abiogenic aragonite precipitation

experiments, which indicates the absence of biological effect on Mg isotope fractionation during the organomineralization of aragonite.

The microstructure of the two stromatolitic mounds is primarily composed of micrite, as revealed by microscopy characterization. The in situ micrite precipitation is ascribed to the organomineralization processes mediated by both anoxygenic photosynthesis by Chloroflexi and heterotrophic degradation of EOM matrix by SRB. Through comparison, it is concluded that cyanobacteria act as the primary functional community to produce organic matter in other environments, which is different from the dominant Chloroflexi in Storr's Lake. Stromatolites in other environments can form lamination either through periodic precipitation and non-precipitation (hypersaline Big Pond) or via alternating cyanobacterial filament orientations (freshwater), whereas laminae formation in Storr's Lake occurs due to the sequential lithification of microbial mats. The mechanism for oraganomineralizaiton and laminae formation proposed in this study could provide additional useful clues for linking modern stromatolites to fossil counterparts.

Appendix A

Table of In Situ Water Chemistry Parameters Measured or Calculated for Storr's Lake Water, Conduit Water, Well Water, and Seawater from Dim Bay (San Salvador Island, Bahamas) Collected in January 2016

Sample	Easting	Northing	Distance from shore	Water depth	Total depth to microbial head	Temperature	pH
	m	m	m	cm	cm	°C	
Storr's Lake, north sector							
EN1, 5 cm	556855	2661653	1640	5	55	26.8	8.49
EN1, 55 cm	556855	2661653	1640	55	55	26.3	8.47
EN2, 5 cm	556740	2662083	1860	5	52	27.5	8.27
EN2, 52 cm	556740	2662083	1860	52	52	27.1	8.30
WN1, 5 cm, Jan 8	555672	2660727	129	5	44	25.3	8.22
WN1, 20 cm, Jan 8	555672	2660727	129	20	44	24.9	8.23
WN1, 40 cm, Jan 8	555672	2660727	129	40	44	24.6	8.17
WN1, 5 cm, Jan 11	555672	2660727	129	5	40	26.1	8.46
WN1, 5 cm, Jan 11 (field dup)	555672	2660727	129	5	40	26.0	8.46
WN1, 5 cm, Jan 11 (field trip)	555672	2660727	129	5	40	26.1	8.45
WN1, 20 cm, Jan 11	555672	2660727	129	20	40	26.1	8.45
WN1, 20 cm, Jan 11 (field dup)	555672	2660727	129	20	40	26.0	8.46
WN1, 20 cm, Jan 11 (field trip)	555672	2660727	129	20	40	26.0	8.46
WN1, 40 cm, Jan 11	555672	2660727	129	40	40	26.0	8.45
WN1, 40 cm, Jan 11 (field dup)	555672	2660727	129	40	40	26.0	8.45
WN1, 40 cm, Jan 11 (field trip)	555672	2660727	129	40	40	26.0	8.46
WN2, 5 cm, Jan 8	555710	2660741	168	5	82	26.2	8.27
WN2, 40 cm, Jan 8	555710	2660741	168	40	82	24.6	8.23

Sample	Easting	Northing	Distance from shore	Water depth	Total depth to microbial head	Temperature	pH
	m	m	m	cm	cm	°C	
Storr's Lake, north sector							
WN2, 82 cm, Jan 8	555710	2660741	168	82	82	24.6	8.21
WN2, 5 cm, Jan 11	555710	2660741	168	5	88	25.9	8.51
WN2, 40 cm, Jan 11 (dup)	555710	2660741	168	40	88	25.9	8.47
WN2, 40 cm, Jan 11 (trip)	555710	2660741	168	40	88	25.9	8.48
WN2, 82 cm, Jan 11	555710	2660741	168	88	88	25.8	8.48
WN2, 82 cm, Jan 11 (dup)	555710	2660741	168	88	88	25.8	8.48
WN2, 82 cm, Jan 11 (trip)	555710	2660741	168	88	88	25.8	8.48
WN3, 5 cm, Jan 8	555778	2660760	238	5	102	26.6	8.46
WN3, 20 cm, Jan 8	555778	2660760	238	20	102	26.1	n/a
WN3, 40 cm, Jan 8	555778	2660760	238	40	102	25.1	8.41
WN3, 60 cm, Jan 8	555778	2660760	238	60	102	24.4	n/a
WN3, 80 cm, Jan 8	555778	2660760	238	80	102	24.2	8.41
WN3, 102 cm, Jan 8	555778	2660760	238	102	102	24.5	8.37
WN3, 116 cm, Jan 8	555778	2660760	238	116	102	24.7	n/a
WN3, 5 cm, Jan 11	555778	2660760	238	5	104	26.2	8.50
WN3, 40 cm, Jan 11	555778	2660760	238	40	104	26.2	8.48
WN3, 40 cm, Jan 11	555778	2660760	238	80	104	26.1	8.48
WN3, 104 cm, Jan 11	555778	2660760	238	104	104	26.0	8.48

Sample	Easting	Northing	Distance from shore	Water depth	Total depth to microbial head	Temperature	pH
	m	m	m	cm	cm	°C	
Storr's Lake, north sector							
WN3, 124 cm, Jan 11	555778	2660760	238	124	104	26.0	n/a
WN4, 5 cm	556371	2662324	1860	5	75	26.7	8.33
WN4, 30 cm	556371	2662324	1860	30	75	26.6	n/a
WN4, 50 cm	556371	2662324	1860	50	75	25.9	n/a
WN4, 75 cm	556371	2662324	1860	75	75	24.7	8.34
WN4, 116 cm	556371	2662324	1860	116	75	24.2	n/a
WN6, 120 cm	556080	2661822	n/a	120	~120	27.1	8.48
WN8, 5 cm	555903	2660788	347	5	61	26.4	8.48
SWN1, 5 cm	555976	2659816	85	5	60	27.1	8.42
SWN1, 30 cm	555976	2659816	85	30	60	27.1	n/a
SWN1, 54 cm	555976	2659816	85	54	60	25.3	8.31
SWN1, 87 cm	555976	2659816	85	87	60	25.4	n/a
SWN2, 5 cm	555942	2659789	n/a	5	40	26.1	n/a
SWN2, 20 cm	555942	2659789	n/a	20	40	26.0	n/a
SWN2, 40 cm	555942	2659789	n/a	40	40	26.0	8.48
near SWN1, 5 cm	555975	2659817	n/a	5	60	25.9	n/a
near SWN1, 30 cm	555975	2659817	n/a	30	60	25.9	n/a
near SWN1, 60 cm	555975	2659817	n/a	60	60	25.8	8.49

Sample	Easting	Northing	Distance from shore	Water depth	Total depth to microbial head	Temperature	pH
	m	m	m	cm	cm	°C	
Storr's Lake, south sector							
ES1, 10 cm	556348	2658225	62.8	10	50	26.3	8.36
ES1, 50 cm	556348	2658225	62.8	50	50	26.3	8.36
WS1, 5 cm	556098	2658256	n/a	5	111	25.5	8.41
WS1, 50 cm	556098	2658256	n/a	50	111	25.3	8.44
WS1, 111 cm	556098	2658256	n/a	111	111	24.8	8.32
WS1, 125 cm	556098	2658256	n/a	125	111	24.8	n/a
WS1, sediment	556098	2658256	n/a	muck	111	25.0	n/a
WS2, 5 cm	556078	2658255	265	5	46	26.3	8.40
WS2, 20 cm	556078	2658255	265	20	46	26.3	8.40
WS2, 46 cm	556078	2658255	265	46	46	26.2	8.40
WS3, 5 cm	556069	2658253	n/a	5	40	26.6	8.49
WS3, 20 cm	556069	2658253	n/a	20	40	26.5	n/a
SSS1, 10 cm	555817	2657041	5	10	n/a	27.7	8.30
SSS1, 20 cm	555817	2657041	5	20	n/a	27.5	8.29
SSS1, 40 cm	555817	2657041	5	40	n/a	27.1	8.25
Conduit into Storr's Lake, north sector							
conduit - N, Jan 8	555563	2660659	n/a	5	n/a	22.2	7.80

Sample	Easting	Northing	Distance from shore	Water depth	Total depth to microbial head	Temperature	pH
	m	m	m	cm	cm	°C	
Conduit into Storr's Lake, north sector							
conduit - N, Jan 11	555563	2660659	n/a	5	n/a	27.8	8.03
conduit - N, Jan 11	555563	2660659	n/a	5	n/a	27.8	8.03
conduit - S, Jan 8	555563	2660659	n/a	5	n/a	21.9	7.85
conduit - S, Jan 11	555563	2660659	n/a	5	n/a	26.9	8.16
Gerace Research Center well	n/a	n/a	n/a	surface bucket	n/a	26.2	7.54
Seawater, Dim Bay	555911	2656751	n/a	n/a	n/a	26.1	8.26
Salt Pond							
North Salt Pond	555840	2656715	east shore	10	45	28.0	8.37
South Salt Pond	555729	2656398	1	40	n/a	26.2	8.38
Six Pack Marsh	552606	2660335	n/a	10	n/a	26.1	7.60
Triangle Pond	548911	2665965	n/a	3	n/a	n/a	8.72

Continued

Sample	Conductivity mS/cm	Salinity PSU	DO mg/L
Storr's Lake, north sector			
EN1, 5 cm	58.3	37.44	8.26
EN1, 55 cm	56.8	36.76	6.23
EN2, 5 cm	59.5	37.70	8.15
EN2, 52 cm	59.3	37.91	7.26
WN1, 5 cm, Jan 8	54.4	35.76	5.36
WN1, 20 cm, Jan 8	54.1	35.83	4.14
WN1, 40 cm, Jan 8	53.8	35.86	4.69
WN1, 5 cm, Jan 11	56.5	36.63	7.34
WN1, 5 cm, Jan 11 (field dup)	56.4	36.67	7.30
WN1, 5 cm, Jan 11 (field trip)	56.4	36.62	7.66
WN1, 20 cm, Jan 11	56.4	36.61	7.08
WN1, 20 cm, Jan 11 (field dup)	56.4	36.64	6.94
WN1, 20 cm, Jan 11 (field trip)	56.4	36.66	7.28
WN1, 40 cm, Jan 11	56.4	36.66	6.30
WN1, 40 cm, Jan 11 (field dup)	56.4	36.65	5.84
WN1, 40 cm, Jan 11 (field trip)	56.4	36.65	6.15
WN2, 5 cm, Jan 8	55.7	36.01	5.70
WN2, 40 cm, Jan 8	53.9	35.92	5.32
WN2, 82 cm, Jan 8	54.4	36.31	2.84
WN2, 5 cm, Jan 11	56.4	36.77	8.20
WN2, 40 cm, Jan 11 (dup)	56.4	36.77	7.66
WN2, 40 cm, Jan 11 (trip)	56.4	36.78	7.49
WN2, 82 cm, Jan 11	56.3	36.79	5.34
WN2, 82 cm, Jan 11 (dup)	56.3	36.78	6.08
WN2, 82 cm, Jan 11 (trip)	56.4	36.81	5.85
WN3, 5 cm, Jan 8	55.7	35.69	7.98
WN3, 20 cm, Jan 8	55.1	35.67	7.25
WN3, 40 cm, Jan 8	54.2	35.76	6.62
WN3, 60 cm, Jan 8	53.7	35.93	6.00

Sample	Conductivity mS/cm	Salinity PSU	DO mg/L
Storr's Lake, north sector			
WN3, 80 cm, Jan 8	53.7	36.13	5.32
WN3, 102 cm, Jan 8	54.1	36.20	3.31
WN3, 116 cm, Jan 8	54.7	36.43	2.70
WN3, 5 cm, Jan 11	56.8	36.77	8.24
WN3, 40 cm, Jan 11	56.7	36.76	7.48
WN3, 40 cm, Jan 11	56.7	36.80	6.73
WN3, 104 cm, Jan 11	56.6	36.85	5.07
WN3, 124 cm, Jan 11	56.7	36.89	2.38
WN4, 5 cm	57.7	37.05	9.20
WN4, 30 cm	57.7	37.10	8.94
WN4, 50 cm	57.5	37.55	8.70
WN4, 75 cm	56.3	37.68	7.00
WN4, 116 cm	55.7	37.64	6.03
WN6, 120 cm	58.7	37.42	5.40
WN8, 5 cm	56.8	36.62	7.60
SWN1, 5 cm	58.0	36.96	7.31
SWN1, 30 cm	57.9	36.85	6.78
SWN1, 54 cm	56.5	37.34	3.16
SWN1, 87 cm	54.9	36.01	1.53
SWN2, 5 cm	56.3	36.53	7.01
SWN2, 20 cm	56.2	36.55	6.72
SWN2, 40 cm	56.3	36.58	5.96
near SWN1, 5 cm	56.2	36.59	7.20
near SWN1, 30 cm	56.1	36.56	6.43
near SWN1, 60 cm	56.1	36.62	5.45
Storr's Lake, south sector			
WS1, 5 cm	55.9	36.73	6.36
WS1, 50 cm	55.8	36.79	4.24
WS1, 111 cm	56.1	37.44	0.80
WS1, 125 cm	56.2	37.51	0.50

Sample	Conductivity mS/cm	Salinity PSU	DO mg/L
Storr's Lake, south sector			
WS1, sediment	51.9	34.11	0.02
WS2, 5 cm	57.1	36.91	6.16
WS2, 20 cm	57.3	37.10	5.22
WS2, 46 cm	57.2	37.09	5.32
WS3, 5 cm	57.9	37.26	6.86
WS3, 20 cm	57.8	37.30	6.14
SSS1, 10 cm	54.2	33.83	6.00
SSS1, 20 cm	53.8	33.69	6.09
SSS1, 40 cm	53.6	33.81	6.00
Conduit into Storr's Lake, north sector			
conduit - N, Jan 8	2.3	1.27	4.90
conduit - N, Jan 11	4.2	2.12	3.58
conduit - S, Jan 8	2.4	1.33	4.65
conduit - S, Jan 11	4.4	2.23	4.72
Gerace Research Center well	n/a	n/a	3.60
Seawater, Dim Bay	45.9	29.02	7.05
Salt Pond			
North Salt Pond	58.0	36.25	6.81
South Salt Pond	54.4	35.05	5.44
Six Pack Marsh	1.9	0.95	3.41
Triangle Pond	n/a	n/a	n/a

Appendix B

Table of Water Chemistry Parameters and Elemental Abundance for Storr's Lake Water, Conduit Water, Well Water, and Dim Bay Seawater Collected in January 2016

Sample	Turbidity NTU	Total Akalinity mg/L as $CaCO_3$	Ca hardness mg/L as $CaCO_3$	Mg hardness mg/L as $CaCO_3$	Ca^{2+} mmol/L	Mg^{2+} mmol/L	Na^{+} mmol/L
Storr's Lake, north sector							
EN1, 55 cm	98	122	1370	7330	13.59	62.84	569.7
EN2, 52 cm	109	127	1390	7310	13.37	60.05	564.3
WN1, 40 cm, Jan 8	110	113	1380	7320	13.54	61.02	573.0
WN1, 40 cm, Jan 11	100	131	1350	7450	n/a	n/a	n/a
WN1, 40 cm, Jan 11 (field dup)	95	129	1410	7090	n/a	n/a	n/a
WN1, 40 cm, Jan 11 (field trip)	95	127	1330	7570	n/a	n/a	n/a
WN2, 82 cm, Jan 8	219	117	1380	7620	13.55	60.65	568.0
WN2, 82 cm, Jan 11	102	126	1370	7330	13.45	60.00	562.4
WN3, 102 cm, Jan 8	259	109	1585	7715	12.95	59.10	548.8
WN3, 104 cm, Jan 11	106	121	1350	7050	13.35	60.06	563.9
WN4, 75 cm	107	123	1330	7370	13.40	61.85	565.1
WN6, 120 cm	104	128	1440	6960	13.19	61.04	557.0
WN8, 61 cm	97	129	1470	7430	13.42	60.12	565.4
SWN1, 54 cm	171	137	1390	7010	13.45	59.96	570.1
SWN2, 40 cm	98	134	1400	7400	13.55	60.38	569.4
near SWN1, 60 cm	100	127	1400	7200	n/a	n/a	n/a
Storr's Lake, south sector							
ES1, 10 cm	93	132	1350	7600	13.60	60.22	561.7

Sample	Turbidity NTU	Total Akalinity mg/L as $CaCO_3$	Ca hardness mg/L as $CaCO_3$	Mg hardness mg/L as $CaCO_3$	Ca^{2+} mmol/L	Mg^{2+} mmol/L	Na^{+} mmol/L
Storr's Lake, south sector							
ES1, 50 cm	94	127	1385	7515	13.47	60.04	567.0
WS1, 5 cm	94	149	1390	7110	13.62	62.47	565.2
WS1, 50 cm	100	147	1360	7440	13.47	60.43	569.4
WS1, 111 cm	95	138	1345	7555	13.62	63.53	579.2
WS2, 46 cm	101	160	1310	7190	13.96	64.85	608.2
WS3, 40 cm	109	140	1390	7410	13.50	60.92	571.0
Storr's Lake, south of south sector							
SSS1, 40 cm	58	137	1790	6710	17.72	52.37	505.7
Conduit into Storr's Lake, north sector							
conduit - N, Jan 8	0.8	280	270	630	2.08	2.07	19.0
conduit - S, Jan 8	0.7	266	230	270	1.98	2.14	19.6
Gerace Research Center well	1.9	247	170	330	1.10	1.42	2.5
Seawater, Dim Bay	0.8	118	950	5950	10.32	53.12	439.2

Sample	Turbidity NTU	Total Akalinity mg/L as $CaCO_3$	Ca hardness mg/L as $CaCO_3$	Mg hardness mg/L as $CaCO_3$	Ca^{2+} mmol/L	Mg^{2+} mmol/L	Na^{+} mmol/L
Salt Pond							
North Salt Pond	14.8	164	1720	6780	17.47	58.19	546.8
South Salt Pond	12.7	173	1770	8923	17.59	56.84	524.2
Six Pack Marsh	3.0	225	260	240	1.76	1.09	12.5

Continued

Sample	K^{+} mmol/L	Sr^{2+} mmol/L	HCO_3^{-} mmol/L	Cl^{-} mmol/L	SO_4^{2-} mmol/L	Ionic Strength mole
Storr's Lake, north sector						
EN1, 55 cm	12.16	0.16	2.44	764.9	38.3	0.82
EN2, 52 cm	12.63	0.17	2.54	713.7	36.6	0.79
WN1, 40 cm, Jan 8	12.73	0.17	2.26	512.6	56.6	0.71
WN1, 40 cm, Jan 11	n/a	n/a	2.62	n/a	n/a	n/a

Sample	K^+ mmol/L	Sr^{2+} mmol/L	HCO_3^- mmol/L	Cl^- mmol/L	SO_4^{2-} mmol/L	Ionic Strength mole
Storr's Lake, north sector						
WN1, 40 cm, Jan 11 (field dup)	n/a	n/a	2.58	n/a	n/a	n/a
WN1, 40 cm, Jan 11 (field trip)	n/a	n/a	2.54	n/a	n/a	n/a
WN2, 82 cm, Jan 8	12.66	0.17	2.34	408.2	26.8	0.63
WN2, 82 cm, Jan 11	12.51	0.17	2.52	706.2	35.6	0.78
WN3, 102 cm, Jan 8	12.42	0.16	2.18	557.8	28.5	0.69
WN3, 104 cm, Jan 11	12.63	0.17	2.42	695.4	35.6	0.78
WN4, 75 cm	12.05	0.16	2.46	738.7	37.5	0.80
WN6, 120 cm	11.84	0.16	2.56	504.5	31.9	0.68
WN8, 61 cm	11.50	0.17	2.58	1119.5	63.5	1.02
SWN1, 54 cm	12.66	0.17	2.74	719.5	36.0	0.79
SWN2, 40 cm	12.64	0.17	2.68	724.6	36.5	0.80
near SWN1, 60 cm	n/a	n/a	2.54	n/a	n/a	n/a
Storr's Lake, south sector						
ES1, 10 cm	12.53	0.17	2.64	723.7	37.3	0.79
ES1, 50 cm	12.60	0.17	2.54	729.3	37.4	0.80
WS1, 5 cm	12.17	0.16	2.98	712.3	36.2	0.79
WS1, 50 cm	12.60	0.17	2.94	906.1	47.6	0.90
WS1, 111 cm	12.42	0.16	2.76	712.6	37.4	0.81

Sample	K^+ mmol/L	Sr^{2+} mmol/L	HCO_3^- mmol/L	Cl^- mmol/L	SO_4^{2-} mmol/L	Ionic Strength mole
Storr's Lake, south sector						
WS2, 46 cm	13.42	0.15	3.20	716.4	37.3	0.82
WS3, 40 cm	12.45	0.16	2.80	708.6	39.8	0.79
Storr's Lake, south of south sector						
SSS1, 40 cm	11.44	0.16	2.74	655.8	36.7	0.72
Conduit into Storr's Lake, north sector						
conduit - N, Jan 8	0.40	0.06	5.60	23.2	0.7	0.03
conduit - S, Jan 8	0.89	0.06	5.32	21.0	0.2	0.03
Gerace Research Center well	0.09	0.09	4.94	3.3	0.5	0.01
Seawater, Dim Bay	9.84	0.08	2.36	346.8	26.8	0.52
Salt Pond						
North Salt Pond	12.59	0.19	3.28	503.9	29.2	0.67
South Salt Pond	12.03	0.19	3.46	627.3	34.4	0.72

Sample	K^+ mmol/L	Sr^{2+} mmol/L	HCO_3^- mmol/L	Cl^- mmol/L	SO_4^{2-} mmol/L	Ionic Strength mole
Six Pack Marsh	0.24	0.03	4.50	33.0	3.0	0.03
Triangle Pond	9.78	0.08	3.30	502.0	28.8	0.60
Lab Blank	0.01	0.00	0.00	0.0	0.0	n/a

Continued

Sample	Mg/Ca mole/mole	Sr/Ca mole/mole	$SI_{calcite}$	$SI_{aragonite}$
Storr's Lake, north sector				
EN1, 55 cm	4.63	0.012	0.99	0.82
EN2, 52 cm	4.49	0.012	0.87	0.71
WN1, 40 cm, Jan 8	4.51	0.012	0.69	0.52
WN1, 40 cm, Jan 11	n/a	n/a	n/a	n/a
WN1, 40 cm, Jan 11 (field dup)	n/a	n/a	n/a	n/a
WN1, 40 cm, Jan 11 (field trip)	n/a	n/a	n/a	n/a
WN2, 82 cm, Jan 8	4.48	0.013	0.80	0.64
WN2, 82 cm, Jan 11	4.46	0.012	1.01	0.85
WN3, 102 cm, Jan 8	4.56	0.012	0.86	0.69
WN3, 104 cm, Jan 11	4.50	0.012	1.00	0.84
WN4, 75 cm	4.62	0.012	0.84	0.68
WN6, 120 cm	4.63	0.012	1.09	0.93
WN8, 61 cm	4.48	0.013	0.92	0.76
SWN1, 54 cm	4.46	0.013	0.88	0.72
SWN2, 40 cm	4.46	0.012	1.04	0.88
near SWN1, 60 cm	n/a	n/a	n/a	n/a
Storr's Lake, south sector				
ES1, 10 cm	4.43	0.012	0.93	0.77
ES1, 50 cm	4.46	0.012	0.91	0.75
WS1, 5 cm	4.59	0.011	1.02	0.86
WS1, 50 cm	4.49	0.012	0.98	0.82
WS1, 111 cm	4.66	0.012	0.88	0.72
WS2, 46 cm	4.65	0.011	1.05	0.89
WS3, 40 cm	4.51	0.012	1.04	0.88
Storr's Lake, south of south sector				
SSS1, 40 cm	2.96	0.009	1.01	0.84

Sample	Mg/Ca mole/mole	Sr/Ca mole/mole	$SI_{calcite}$	$SI_{aragonite}$
Conduit into Storr's Lake, north sector				
conduit - N, Jan 8	0.99	0.030	0.66	0.50
conduit - S, Jan 8	1.08	0.030	0.69	0.53
Gerace Research Center well	1.29	0.084	0.30	0.14
Seawater, Dim Bay	5.15	0.008	0.70	0.53
Salt Pond				
North Salt Pond	3.33	0.011	1.12	0.96
South Salt Pond	3.23	0.011	1.21	1.05
Six Pack Marsh	0.62	0.017	0.31	0.14
Triangle Pond	6.16	0.010	1.22	1.05
Lab Blank	n/a	n/a	n/a	n/a

Appendix C

X-ray Diffraction Pattern of Stromatolitic Knob Sublayer Samples

(Black curve represents sample spectral analysis line, red lines represent spectral pattern for standard sample 98-000-0098 of aragonite, blue lines represent spectral pattern for standard sample 98-000-0293 of Mg-calcite with 12.9 mole % Mg, and green lines represent spectral pattern for standard sample 98-000-0235 of halite)

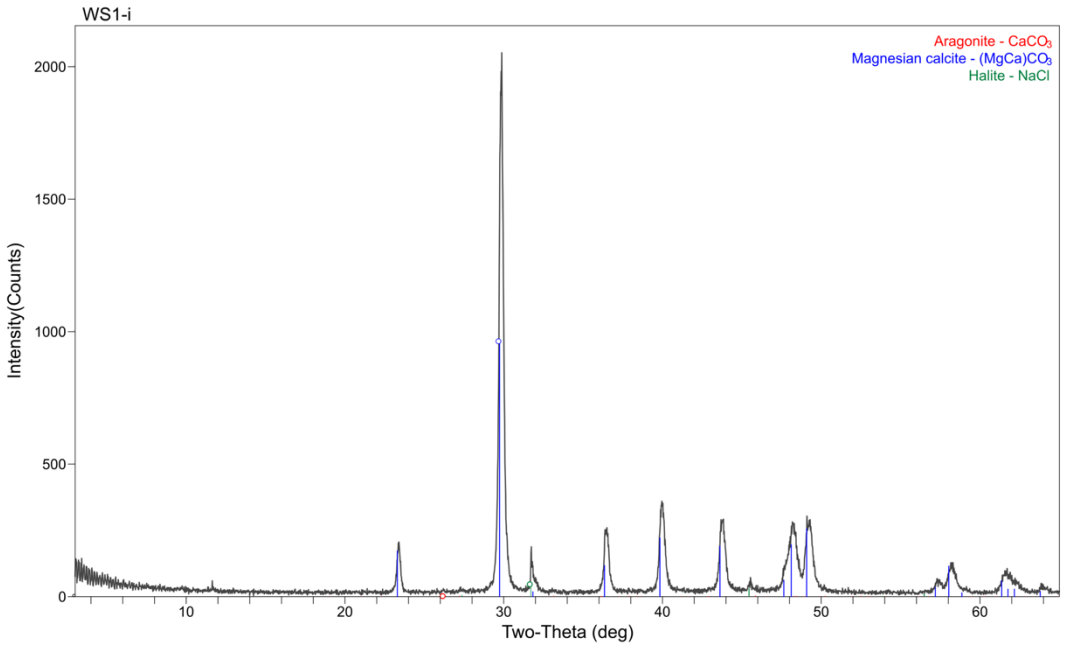
WS1-i
Aragonite - CaCO3
Magnesian calcite - (MgCa)CO3
Halite - NaCl
Intensity(Counts)
2000
1500
1000
500
0
10
20
30
40
50
60
Two-Theta (deg)

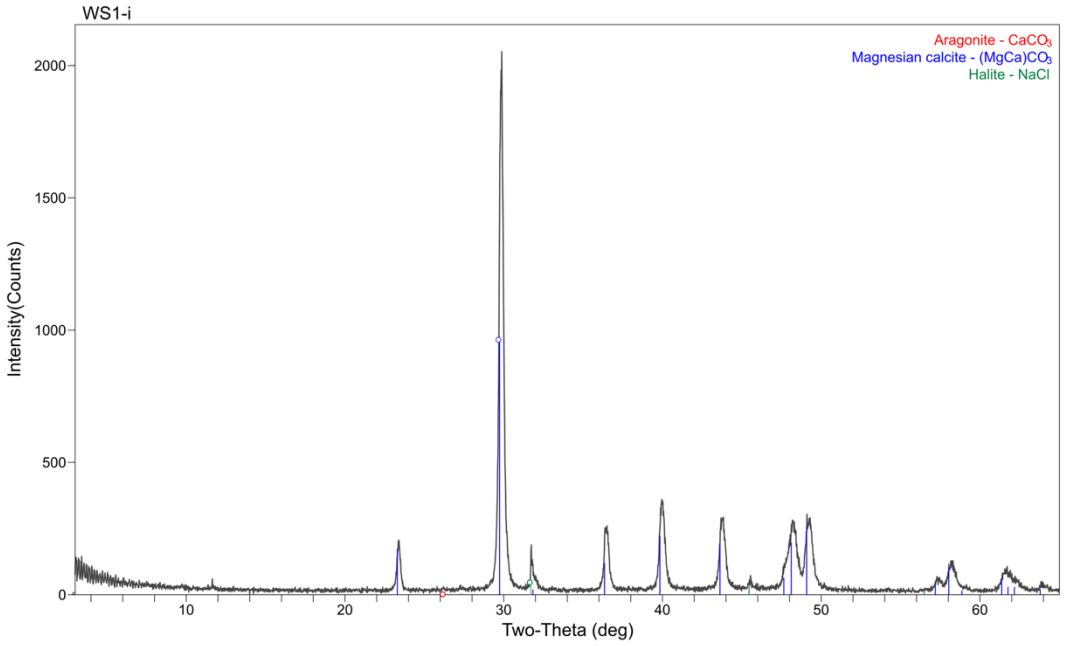
WS1-i
Aragonite - CaCO3
Magnesian calcite - (MgCa)CO3
Halite - NaCl
Intensity(Counts)
2000
1500
1000
500
0
10
20
30
40
50
60
Two-Theta (deg)

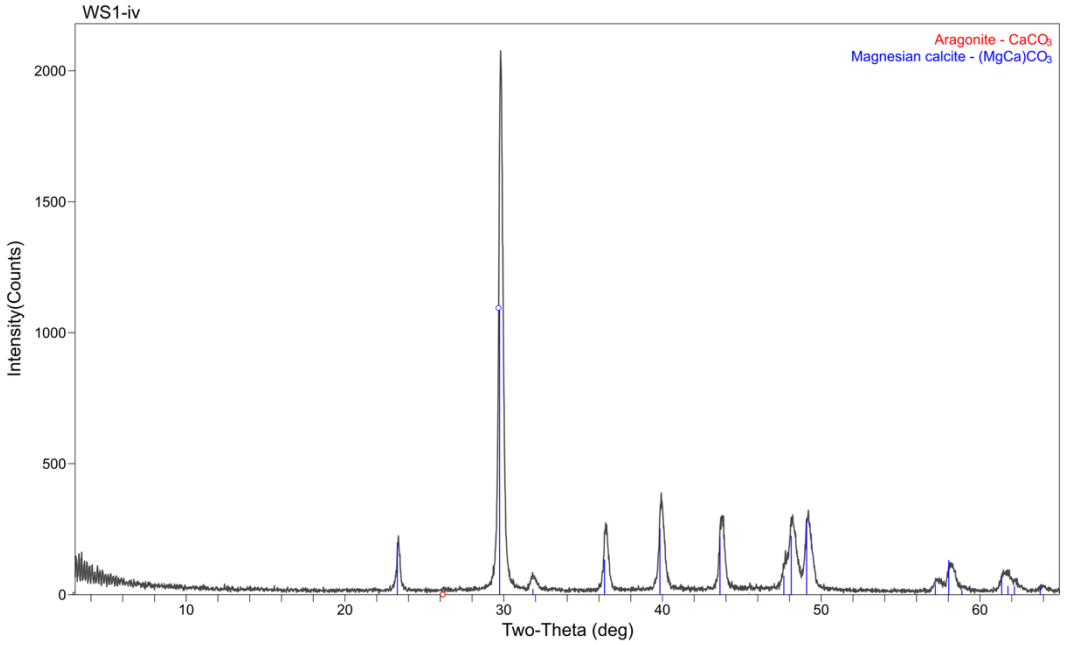
WS1-iv
Aragonite - CaCO3
Magnesian calcite - (MgCa)CO3
Intensity(Counts)
2000
1500
1000
500
0
10
20
30
40
50
60
Two-Theta (deg)

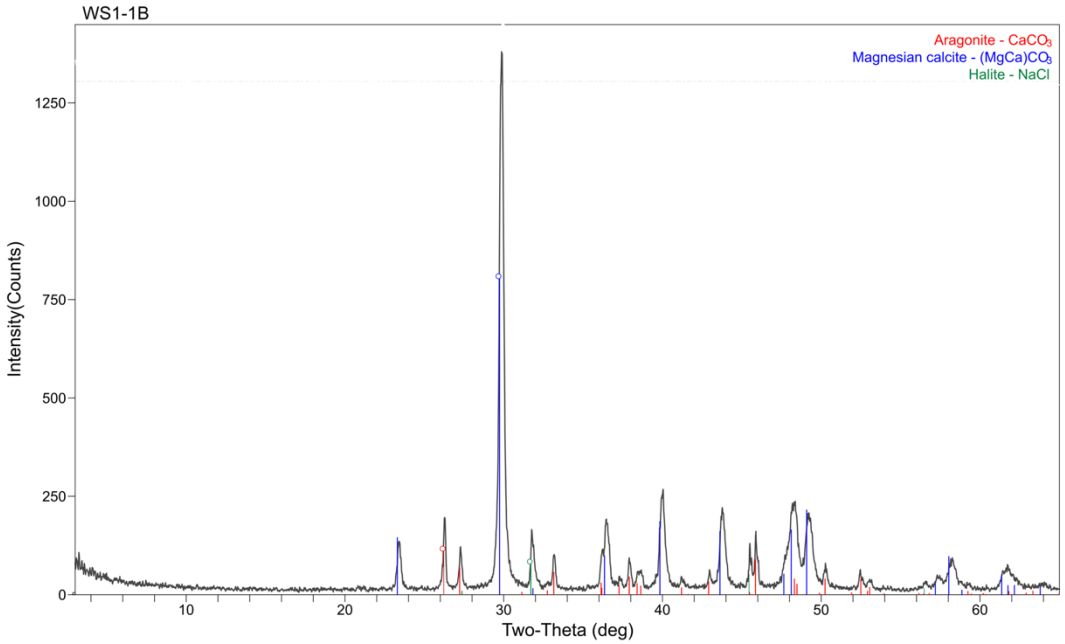
WS1-1B
Aragonite - CaCO3
Magnesian calcite - (MgCa)CO3
Halite - NaCl
Intensity(Counts)
1250
1000
750
500
250
0
10
20
30
40
50
60
Two-Theta (deg)

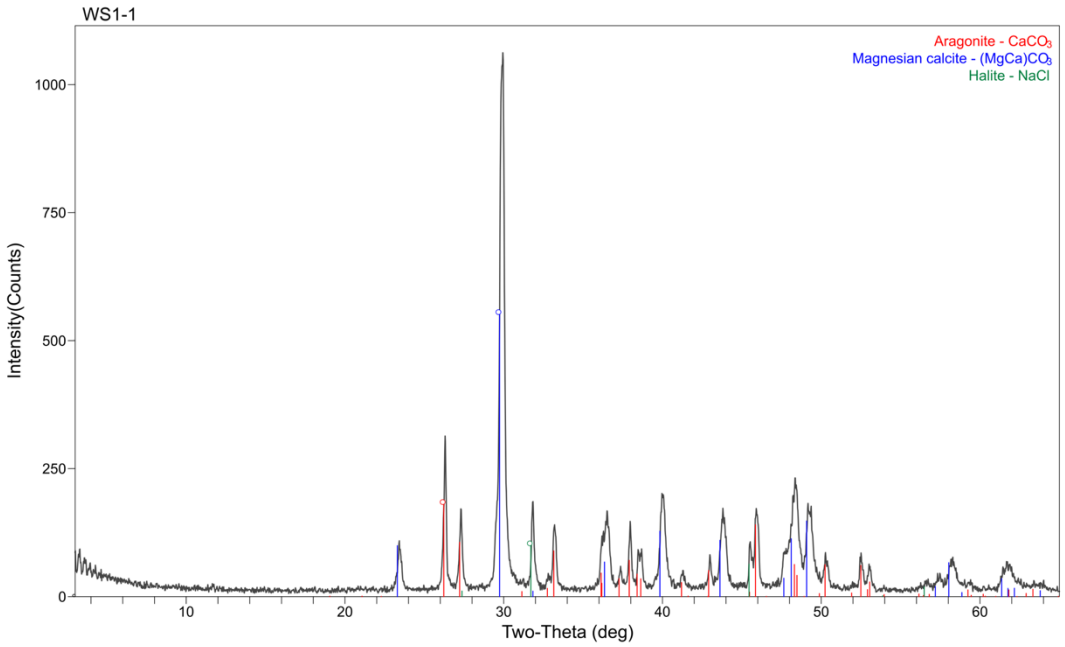
WS1-1
Aragonite - CaCO3
Magnesian calcite - (MgCa)CO3
Halite - NaCl
Intensity(Counts)
1000
750
500
250
0
10
20
30
40
50
60
Two-Theta (deg)

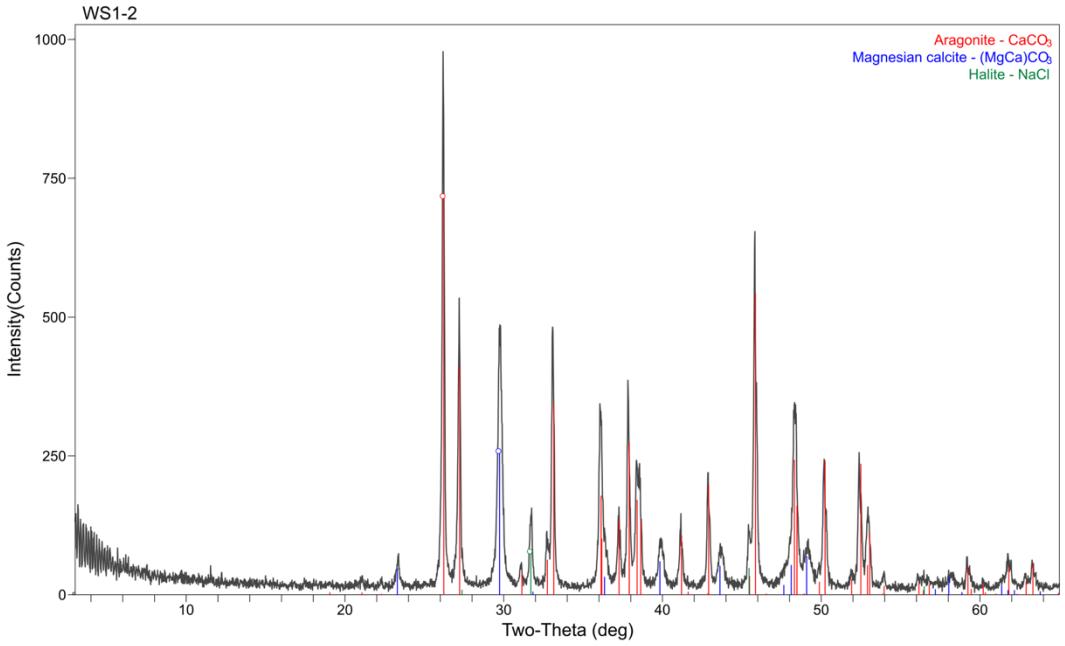
WS1-2
Aragonite - CaCO3
Magnesian calcite - (MgCa)CO3
Halite - NaCl
Intensity(Counts)
1000
750
500
250
0
10
20
30
40
50
60
Two-Theta (deg)

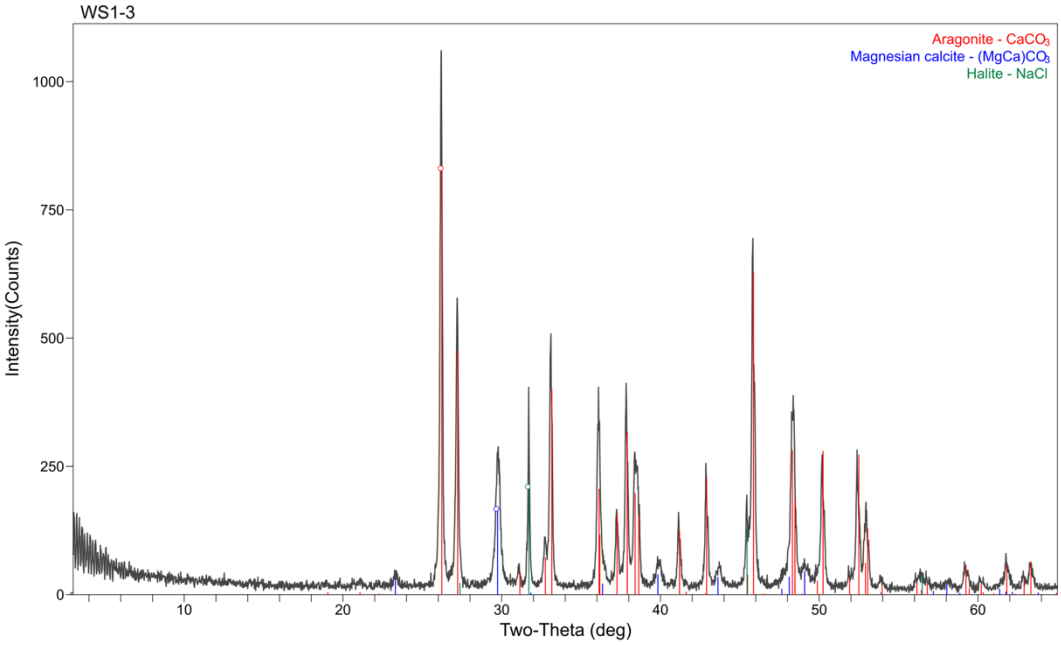
WS1-3
Aragonite - CaCO3
Magnesian calcite - (MgCa)CO3
Halite - NaCl
Intensity(Counts)
Two-Theta (deg)

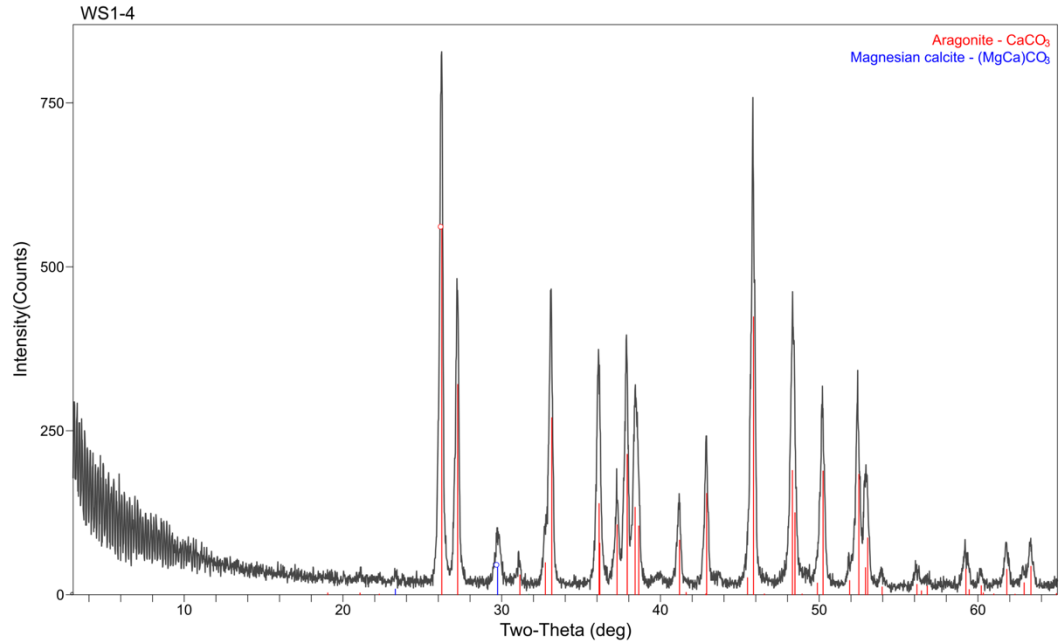
WS1-4
Aragonite - CaCO3
Magnesian calcite - (MgCa)CO3
Intensity(Counts)
Two-Theta (deg)

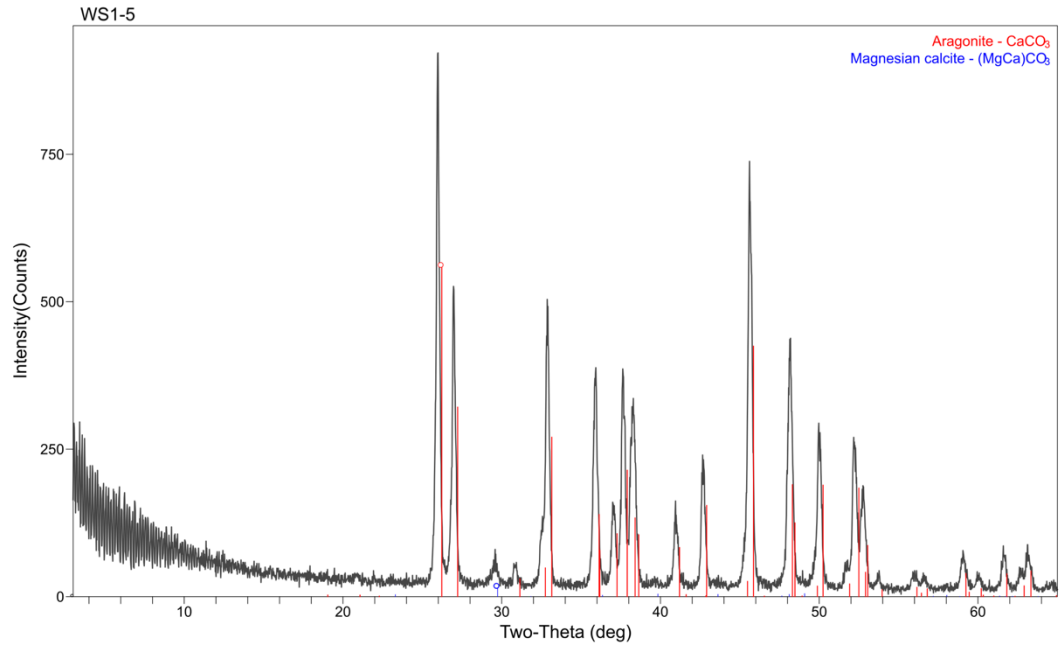
WS1-5
Aragonite - CaCO3
Magnesian calcite - (MgCa)CO3
Intensity(Counts)
0
250
500
750
10
20
30
40
50
60
Two-Theta (deg)

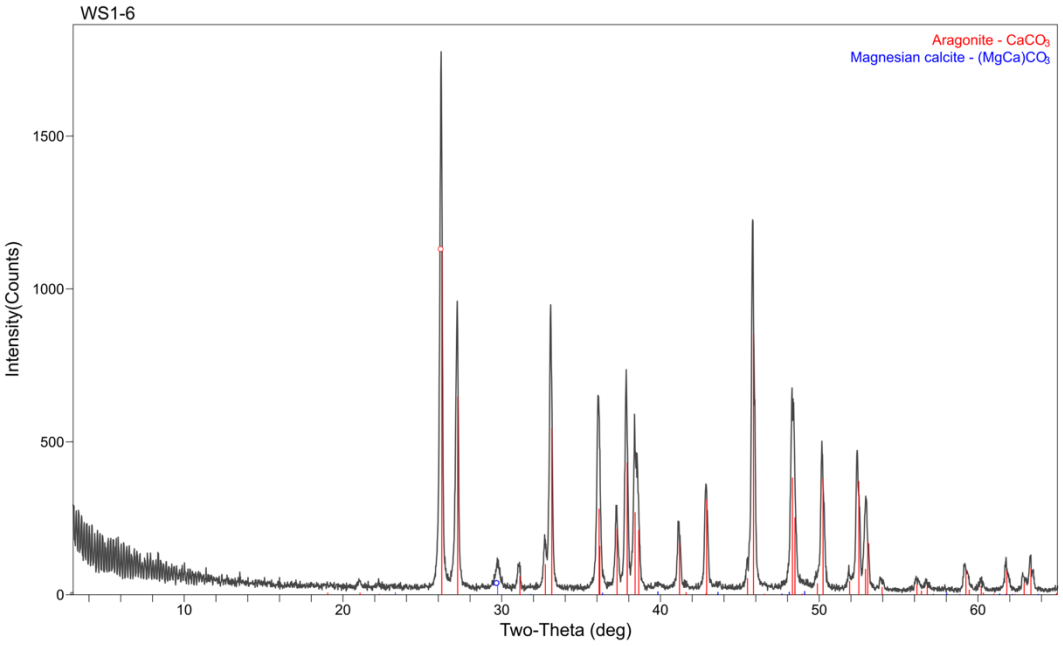
WS1-6
Aragonite - CaCO3
Magnesian calcite - (MgCa)CO3
Intensity(Counts)
0
500
1000
1500
10
20
30
40
50
60
Two-Theta (deg)

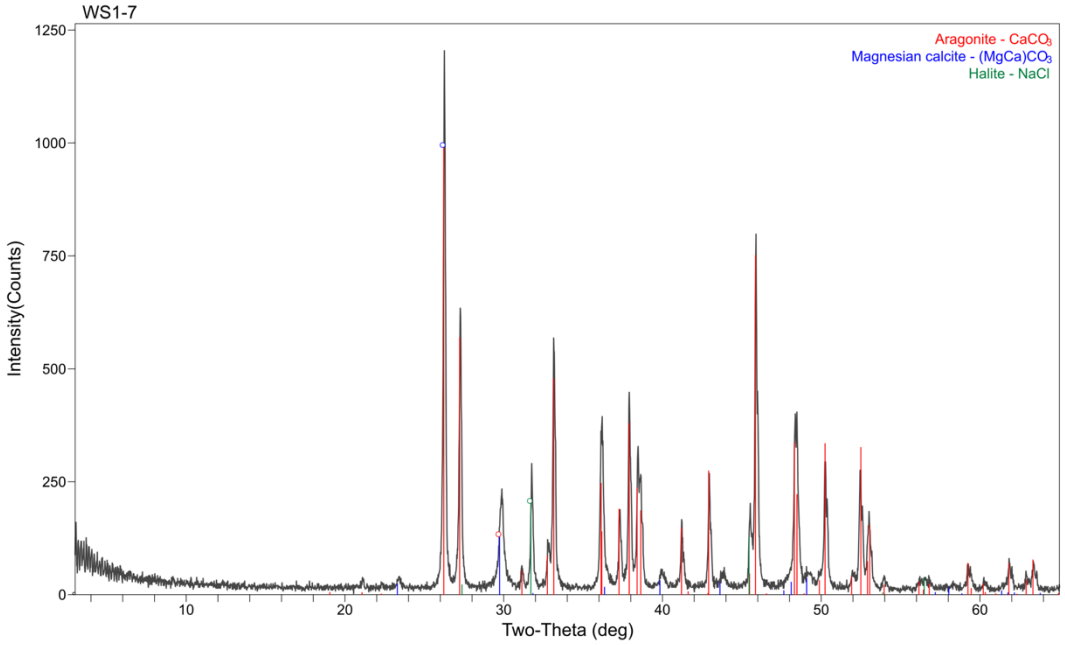
WS1-7
Aragonite - CaCO3
Magnesian calcite - (MgCa)CO3
Halite - NaCl
Intensity(Counts)
Two-Theta (deg)

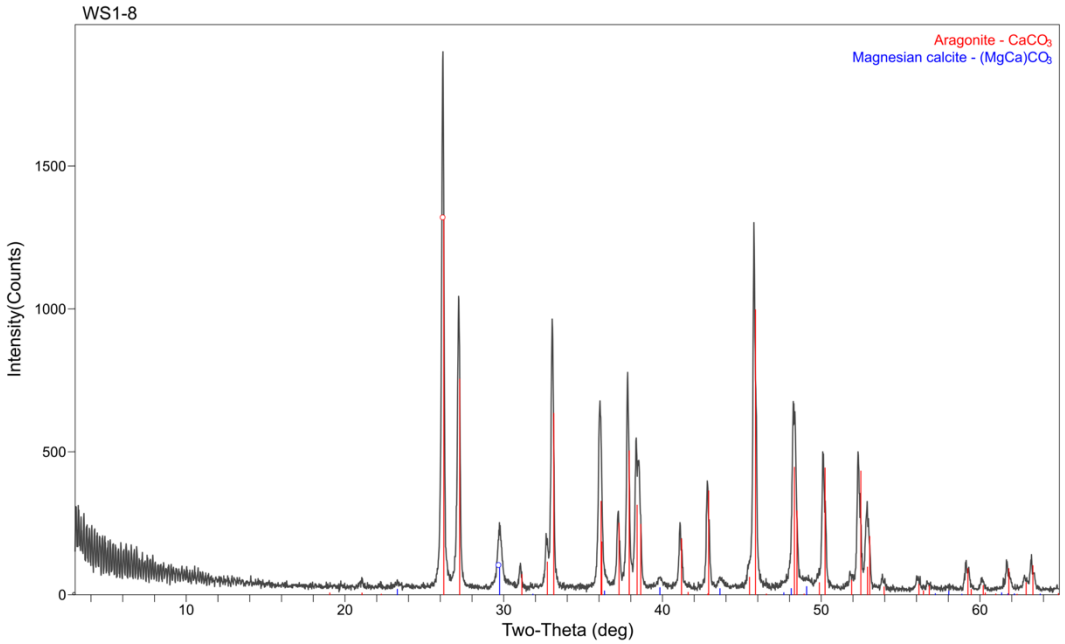
WS1-8
Aragonite - CaCO3
Magnesian calcite - (MgCa)CO3
Intensity(Counts)
Two-Theta (deg)

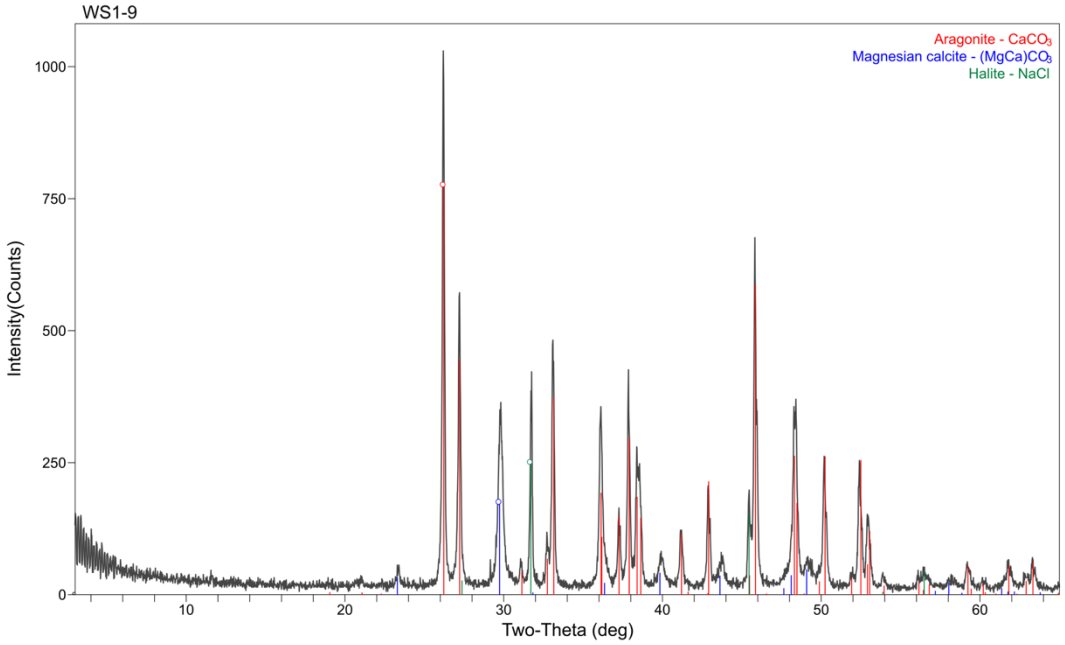
WS1-9
Aragonite - CaCO3
Magnesian calcite - (MgCa)CO3
Halite - NaCl
Intensity(Counts)
Two-Theta (deg)

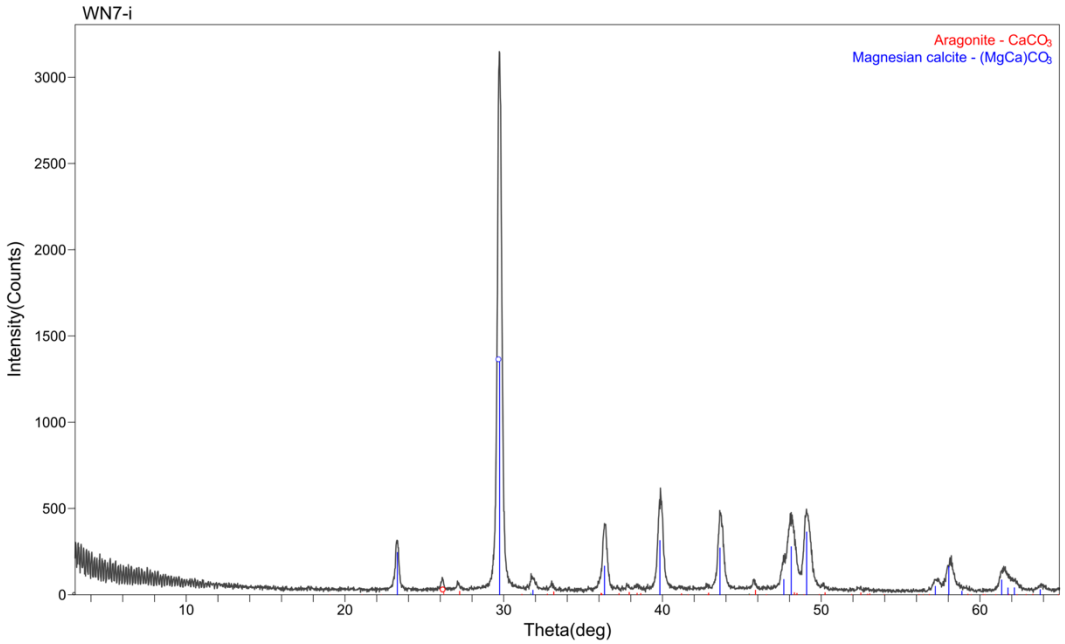
WN7-i
Aragonite - CaCO3
Magnesian calcite - (MgCa)CO3
Intensity(Counts)
Theta(deg)

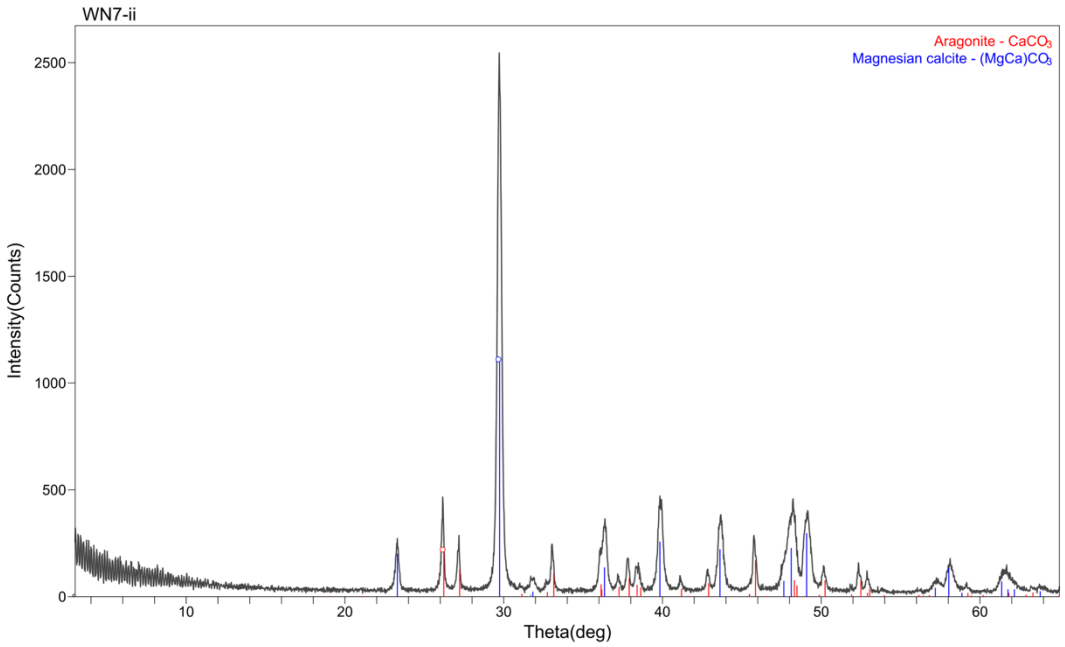
WN7-ii
Aragonite - CaCO3
Magnesian calcite - (MgCa)CO3
Intensity(Counts)
2500
2000
1500
1000
500
0
10
20
30
40
50
60
Theta(deg)

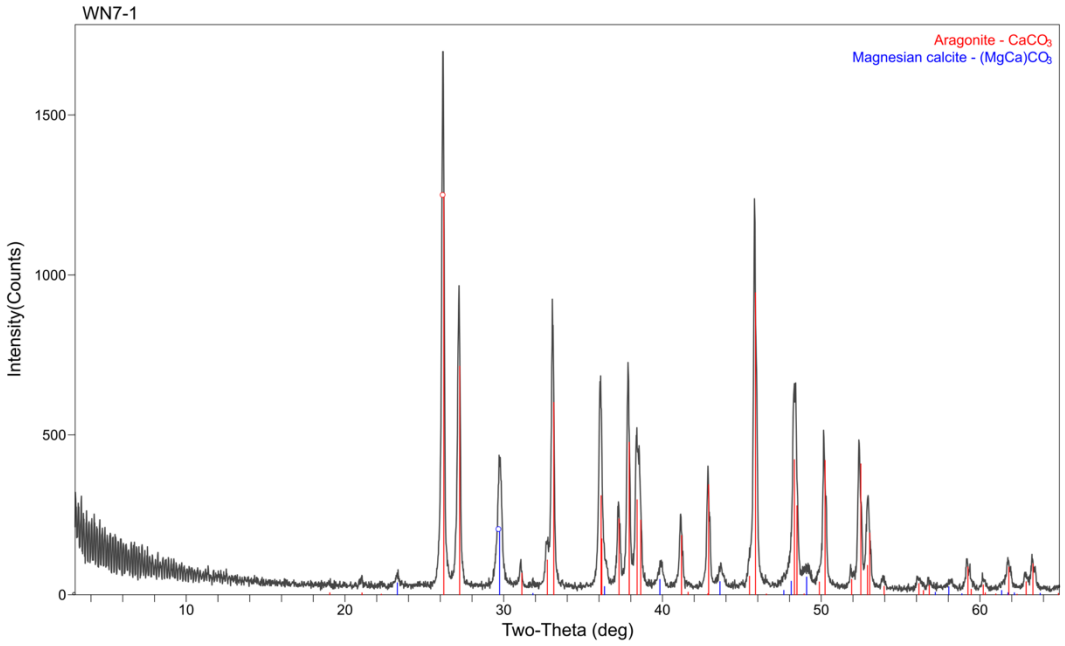
WN7-1
Aragonite - CaCO3
Magnesian calcite - (MgCa)CO3
Intensity(Counts)
1500
1000
500
0
10
20
30
40
50
60
Two-Theta (deg)

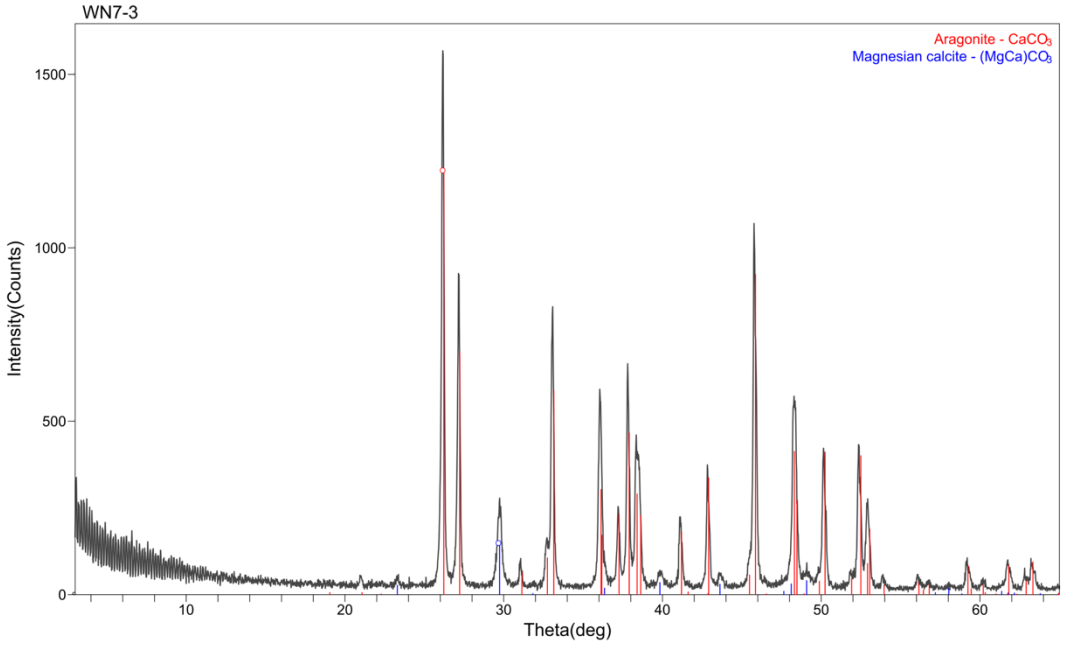
WN7-3
Aragonite - CaCO3
Magnesian calcite - (MgCa)CO3
Intensity(Counts)
Theta(deg)
0
500
1000
1500
10
20
30
40
50
60

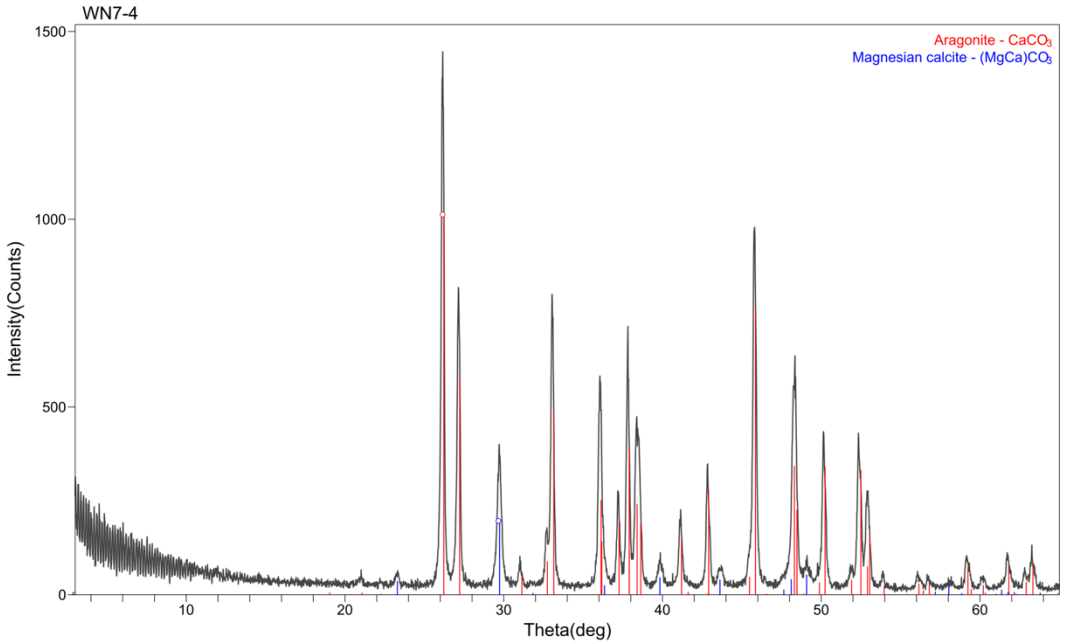
WN7-4
Aragonite - CaCO3
Magnesian calcite - (MgCa)CO3
Intensity(Counts)
Theta(deg)
0
500
1000
1500
10
20
30
40
50
60

Appendix D

Old Mg Column Method and Column Chemistry Worksheet

Step 1: Separation Mg from Matrix - Mg Column Method

Extracting Mg from Samples via 15 ml Savillex® PFA Microcolumn & 2.3 ml Bio-Rad 200-400 mesh AG50W-X8 Cation Exchange Resin

Work in clean lab only.
Wear gloves and clean lab apparel.

Note: The procedure is only relevant for the columns that have been calibrated. Different columns will involve different quantities of acids and must be calibrated before use.

1. Clean AG50W-X8 resin
    a. Spoon dry AG50W-X8 resin into 100 ml "Clean AG50W-X8" bottle (PFA).
    b. Fill the bottle with milli-Q water and shake slightly to submerge the dry resin. Add dry resin until resin volume is around 50 ml.
    c. Screw up the bottle cap. Shake the bottle vigorously. Allow resin to settle (this will take around 10~15 min.). Decant water to the sink. Repeat water clean twice more.
    d. Fill the bottle with 8N HCl (1D) and shake vigorously. Allow resin to settle. Decant acid to HCl waste container.
    e. Fill the bottle with milli-Q and shake vigorously. Allow resin to settle. Decant water to HCl waste container.
    f. Repeat d and e steps twice more.
    g. Fill the bottle with 1N HNO_3 (1D) and shake vigorously. Allow resin to settle. Decant acid to HNO_3 waste container.
    h. Fill the bottle with milli-Q and shake vigorously. Allow resin to settle. Decant water to HNO_3 waste container.
    i. Repeat g and h steps twice more.
    j. Fill the bottle with milli-Q and shake vigorously. Allow resin to settle. Decant water to the sink. Repeat this step until the decant water has pH around 5.
2. Weigh samples (20 µg Mg)
    a. Prepare clean sample beakers for each sample and label them.
    b. Weigh blank beakers and record the values as m_1.
    c. Weigh loaded beakers with proper amounts of samples (containing 20 µg Mg, according to Mg weight percent of each sample) and record the value as m_2.
    d. The weight of sample is m_2-m_1.
3. Digest carbonate samples (water samples skip to step 3)

a. Add a few drops of 10% H_2O_2 into sample beakers and wait for 48 h to remove organic matter. dissolution in dilute hydrochloric acid in preparation for chemical separation.
b. Then add dilute HCl to dissolve samples until no bubbles appear.

4. Dry down samples.
    a. On hot plate inside drying beakers with filtered air. (First dry down with 120°C, when the sample is close to dry, adjust the temperature to 80°C and dry until the samples become wet salt state)
    ~1 hour per ml to be dried down
    b. Weigh beakers again and record the values as m_3.
5. Bring up the samples
    a. Let samples to cool down to room temperature.
    b. Add 100 µl 1N HNO_3 into each beaker.
    c. Tighten the caps of beakers and weigh them, record the values as m_4. The weight of liquid sample is m_4-m_3.
    d. Swish the acid around in the beakers in order to get all of the sample off the walls of the beakers.
    e. Let stand to dissolve (~10 minutes). Sonicate if necessary (1~2 minutes).
6. Clean columns.
    a. Pour 50% clean HNO_3 acid (1D) in large plastic volumetric cylinder.
    b. Submerge the columns upside down into the acid. Use pipette to suck the air out of the columns and fill the columns with acid (pipette tips are acid-cleaned).
    c. Sonicate the loaded cylinder.
    ~30 minutes
    d. Pour the acid out of the cylinder, take out the columns, and use pipette to squeeze the acid out of the columns.
    e. Use wash bottle (filled with Milli-Q) to clean the columns inside and out.
    f. Pour Milli-Q in the glass tray. Submerge the columns in Milli-Q. Use pipette to suck the air out of the columns and fill the columns with water.
    ~15 minutes
    g. Place the columns in the Mg column rack. Make a note on spreadsheet which sample corresponds with which column. Put one waste vial under each column.
    h. Fill the columns with Milli-Q. Use pipette to squeeze out the air in the capillary. Let at least 10 ml Milli-Q flows through the columns (If waste vial is full, dump the water to the sink).
    ~5 minutes
7. Fill columns with resin.
    a. Make sure water is dripping out of the columns (no air in the capillary). Fill the column first with Milli-Q to more than 5 ml in the reservoirs.
    b. Add pre-cleaned resin to columns, allowing the resin to settle down by gravity. Keep adding the resin until the top of the resin is a little higher

than the bottom of the reservoir (the joint between the reservoir and the capillary), as HNO_3 conditioning will noticeably lower the level.
~20 minutes

c. Do not allow the resin to dry out.

8. Clean resin in column (to be tested).
    a. Make each waste vial is half full with Milli-Q.
    b. Rinse resin with 3 ml of 6 N Clean HCl (1D).
    ca. 40~50 minutes
    c. Rinse resin with 3 ml of Milli-Q water.
    ca. 40~50 minutes
    d. Dump waste liquids to the HCl hazardous waste containers
9. Condition the resin with 1 N clean HNO_3 (1D).
    a. Add 6 ml 1 N clean HNO_3 (1D) and allowing it to drip through the column into waste vials. The solution in waste vials can be discarded into the HNO_3 hazardous waste containers.
    80~100 minutes
    b. Again, do not allow the resin to dry out.
10. Adjust height of resin
    a. Add 200 µl 1 N clean HNO_3 (1D) and use pipette to remove the extra resin to a clean beaker. To keep the final resin levels at the bottom of the reservoir (the joint between the reservoir and the capillary). Make sure the resin levels are correct (it is important because the columns have been calibrated based on a specific amount of resin in the columns).
    ~30 minutes
11. Load samples onto columns.
    a. Prepare a separate acid-cleaned pipette tip for each sample. Tighten the caps of beakers and shake beakers up and down to let samples rinse the inner wall of the beakers.
    b. Carefully load 50 µl of each sample on to the resins.
    c. When the samples have percolated into the resins, add 50 µl more of each sample.
    ~1/4 hour
    d. Weigh the beakers again and record the values as m_5. The weight of loaded sample is m_4-m_5.
12. Wash the sides of sample beakers and columns with 1 ml of 1 N clean HNO_3 (1D).
    a. Wash sample sides of sample beaker with 100 µl and load onto column. Wait until it percolates into the column and the level is once again at the bottom rim. Then repeat once more.
    b. Wash carefully the sides of the columns with 200 µl. Wait until level is at rim, then repeat with once more.
    c. Repeat with 400ul.
    1/2 hour

13. Wash with 23 ml of 1 N clean HNO_3 (1D).
    a. Add 10 ml of 1 N clean HNO_3 (1D) to columns. (Let the first 1 ml of 1 N clean HNO_3 (1D) drops on the sides of the columns. Add the acid in drops instead of flows to avoid the resins being disturbed. The two rules are also applied in later steps)
    b. When acid levels just cover the bottom sides of the reservoirs (~1 ml), add the remaining 13 ml of 1 N clean HNO_3 (1D) to columns.
    c. Weigh the labeled 22 ml clean Teflon beakers, and record the value as m_6.
    d. When acid level is at the bottom rim, remove the waste vials from underneath the columns and replace with a set of clean 22 ml Teflon beakers. It will take about 14~18 min. per cc for the acid to drip through the columns.
    e. Do not let the resin dry out.
    f. Dump the waste liquids to the HNO_3 hazardous waste containers.
    6~7 hours
14. Collect Mg cut by eluting 15 ml of 1 N clean HNO_3 (1D).
    a. Add 1 ml of 1 N clean HNO_3 (1D).
    b. When acid level is at the bottom rim, add the remaining 14 ml of 1 N clean HNO_3 (1D).
    3.5~4.5 hours
    c. The 15 ml collected eluant represents the Mg cut. Weigh the loaded beakers and record the values as m_7. The weight of collected Mg cut is m_7-m_6.
15. Remove used resin.
    a. The resin should be replaced after each set of samples has been run. Add Milli-Q to the columns and use pipette to suck the resin out of the columns. Collect & store used resin in the acid-cleaned and labeled PFA bottle.
16. Measure Mg concentration on ICP-OES.
    a. Prepare a set of clean 15 ml beakers and label them. Acid clean corresponding amount of disposable tubes and label them.
    b. Weight their weights on the balance and record the values as m_8.
    c. Use pipette to remove 5 ml of Mg cut of each sample to a 15 ml beaker and weight the loaded 15 ml beaker, record its value as m_9. The weight of removed Mg cut is m_9-m_8.
    d. Dry down the 5ml and 10 ml of Mg cut on the hot plate.
    ~1 hour per ml to be dried down
    e. Weigh the dried 15 ml beakers and record their values as m_{10}.
    f. Bring up 15 ml beakers with 4 ml 2% HNO_3 and weigh the loaded beakers, record their values as m_{11}. The weight of 4 ml 2% HNO_3 is m_{11}-m_{10}.

g. Sonicate the loaded beakers and then transfer the 4 ml 2% HNO_3 to corresponding tubes.
   ~30 minutes
h. Prepare blank and Mg standard. Measure Mg concentration on ICP-OES
   ~10 minutes for each sample
i. Calculate Mg yields with ICP data as well as the weight values recorded in the procedure.

17. Measure Mg isotopic compositions at PSU
    a. Ship the dried 22 ml beakers to PSU for Mg isotopic composition analysis in Metal Isotope Laboratory if the Mg yields are satisfactory.

Step 1 Mg Column

Name: Time:

	Rack	Rack					
	Column	1	2	3	4	5	6
	Sample						
	Lab ID						
Step 1	5 ml H2O						
Step 2	Fill resin in H2O						
Step 3	6 ml 1N HNO3						
Step 4	Adjust height of resin						
Step 5	100 μl sample						
Step 6	200 μl 1N HNO3						
Step 7	300 μl 1N HNO3						
Step 8	500 μl 1N HNO3						
Step 9	23 ml 1N HNO3						
Step 10	1 ml 1N HNO3						
Step 11	14 ml 1N HNO3						

Old step 1 Mg column chemistry worksheet. (This step is to separate Mg from matrix.)

Step 2: Separation Mg from Ca matrix – Ca Column Method

Extracting Mg from Ca matrix via 6 ml Savillex® PFA Microcolumn & 750 µl MCI GEL 100 mesh CK08P Cation Exchange Resin

Preparing materials (*done days before doing column work*):

- Clean the MCI resin *typically already done*
- Clean 3 vials for each sample and blank
- Prepare 1.8 M ultrapure (Optima) HCl
- Prepare 6 M ultrapure (Optima) HCl– note 50% by volume works

Preparing Mg Samples for Ca Columns (*done at least 1 day before doing column work*):

- Dry down (evaporate) sample on hotplate (at 100 to 150 °C), ~1 hour per ml
- Reconstitute dried sample in 75 ul 1.8M HCl - *Ultrasonicate if needed to completely dissolve sample (~10 minutes)*
- Weigh empty (clean) collection Teflon vials

Ca Column Methodology:

1. Fill columns with MilliQ on rack; using pipette to force air out of column
    - Be sure the frits are situated above the line on the column (push up using pipette tip
2. **Load ~1 mL MCI resin** in water onto columns filled with water
    - *Remove excess water from reservoir, leveling resin bed above reservoir bottom*
3. **Wash columns** with 3 mL of 6 M HCl

4. **Wash columns** with 3 mL of MilliQ
    - ***at the end of the wash, push up each frit using a clean pipette tip***
    - ***then, level the resin level to be just at the reservoir bottom, remove excess resin***

5. **Condition the columns**: with 2 mL of 1.8M calibrated HCl

6. **Load the sample** onto the column (75 uL of 1.8M HCl) AND REPLACE waste collection with weighed empty (clean) collection Teflon vials

7. **Continue to load the sample by rinsing the sample vial and adding 50 uL twice, thenn 100 uL twice, then 200 uL**

8. **Wash with 3 ml of 1.8M HCl AND COLLECT for Mg isotopes**

9. Remove collection vials and weigh (full)

10. **Clean Ca off columns** by adding at least 3 ml of 6M HCl, letting this drip into **SAFETY vials** (not need to weigh these – they will only be used if the Mg yield is poor)

After finishing the chemistry, discard the resin in the used resin waste bottle.

Mg yield check:

- Weigh EMPTY Teflon vial (before adding aliquot of collected sample)

- Add _1_ ml of sample solution equivalent to ~5 ug Mg to empty, weighed Teflon vials to test / analyze on ICPES – this should constitute ~1/4 of the weight of the collected sample (NOT MORE THAN ONE FOURTH of 3.5 mL collected)

- Weigh Teflon vials again (after adding sample) – difference is sample weight added

- Dry down (evaporate) sample on hotplate (at 100 to 150 °C), ~1 hour per ml

- Reconstitute dried sample in 4 ml of 2% (by volume) ultrapure HNO_3. Ultrasonicate if needed to completely dissolve sample (~10 minutes)

- Record final weight of 2% HNO_3 sample (in Teflon vial)

- Pour sample into acid-cleaned (10% HNO_3 overnight) ICP tubes (15 ml centrifuge tubes)

- Measure these samples (along with the test load samples if prepared) on the ICPES; Calculate yield…

Step 2 Ca Column **Ca Separation using Calibration from**

Name: Time:

		time start	sample						
	Column								
10 ml 6N HCl	wash	*nd*							
10 ml MilliQ	wash	*nd*							
Load 1 ml Resin	load								
3 ml 6N HCl	wash								
3 ml MilliQ	wash								
2 ml 1.8N HCl	condition								
Load Sample (75 ul)	**SAMPLE**								
50 ul 1.8N HCl	rinse		0 to 0.5						
50 ul 1.8N HCl	sample								
100 ul 1.8N HCl	vial +								
100 ul 1.8N HCl	COLLECT								
200 ul 1.8N HCl	FOR Mg								
3.0 mL1.8N HCl	COLLECT		0.5 to 3.5						
3.0 mL 6N HCl	SAFETY								

Notes:

weights needed for calculating percent yield

	sample COLLECT vial weight empty	sample COLLECT vial weight full	1/4 test vial weight empty	1/4 test vial weight full
1 -				
2 -				
3 -				
4 -				
5 -				
6 -				

Old step 2 Ca column chemistry worksheet.(This step is to separate Mg from Ca matrix)

Appendix E

New Mg Column Method and Column Chemistry Worksheet

Step 1 Mg-Ca column Name: Time:

		Column		time start	1	2	3	4	5	6
		Sample								
		2 reservoir volume MilliQ	wash	*nd*						
		load 1 mL AG50-X8 resin	load resin	*nd*						
	collect in HF waste beakers	3 mL 0.5 N HF	wash							
		3 mL MilliQ								
		3 mL 0.5 N HF								
		3 mL MilliQ								
	collect in HCl waste beakers	3 mL 10 N HCl								
		3 mL MilliQ								
		2 mL 10N HCl	condition							
		adjust resin height	adjust resin							
collect Mg + matrix	collect in 7 ml vials	Load Sample (250 uL 10N)	load sample							
		200 uL 10N HCl	rinse with 10 N HCl							
		300 uL 10N HCl								
		500 uL 10N HCl								
		1.5 mL 10N HCl								
	collect in HCl waste beakers	0.5 ml 8N HCl	rinse with 8 N HCl							
collect Ca	collect in 10 ml vials	10 ml 8N HCl								
		fill reservoir 6N HCl	wash							

New step 1 Mg-Ca column chemistry worksheet. (This step is to separate Mg+matrix from Ca for samples with high Mg/Ca ratio)

Step 2 Mg column Name: Time:

		Column		time start	1	2	3	4	5	6
		Sample								
		2 reservoir volume MilliQ	wash	*nd*						
		load 1 mL AG50-X8 resin	load resin	*nd*						
	collect in HF waste beakers	3 mL 0.5 N HF	wash							
		3 mL MilliQ								
		3 mL 0.5 N HF								
		3 mL MilliQ								
	collect in HCl waste beakers	3 mL 10N HCl								
		3 mL MilliQ								
		3 mL 0.4N HCl	condition							
		adjust resin height	adjust resin							
matrix		Load Sample (250 uL 0.4N)	load sample							
		200 uL 0.4N HCl	rinse with 0.4 N HCl							
		300 uL 0.4N HCl								
		500 uL 0.4N HCl								
		9 mL 0.4N HCl								
		9 mL 0.4N HCl								
		9 mL 0.4N HCl								
		1 ml 1N HCl	rinse with 1 N HCl							
collect Mg	collect in 22 ml vials	13 ml 1N HCl								
		fill reservoir 6N HCl	wash							

New step 2 Mg column chemistry worksheet. (This step is to separate Mg from matrix).

References

Adams, R.W., 1983. General Guide to the Geological Features of San Salvador. In Gerace, D.T. (ed), Field Guide to the Geology of San Salvador. 3rd (Ed.), CCFL Bahamian Field Station, San Salvador, Bahamas, pp. 1–66.

Aitken, J.D., 1967. Classification and environmental significance of cryptalgal limestones and dolomites, with illustrations from the Cambrian and Ordovician of southwestern Alberta. J. Sed. Petrol 37, 1163–1178.

Allwood, A.C., Walter, M.R., Kamber, B.S., Marshall, C.P., Burch, I.W., 2006. Stromatolite reef from the Early Archaean era of Australia. Nature 441, 714–718.

Allwood, A.C., Walter, M.R., Burch, I.W., Kamber, B.S., 2007. 3.43 billion-year-old stromatolite reef from the Pilbara Craton of Western Australia: Ecosystem-scale insights to early life on Earth. Precambrian Research 158, 198–227.

Andersson, A.J., Mackenzie, F.T., Bates, N.R., 2008. Life on the margin: implications of ocean acidification on Mg-calcite, high latitude and cold-water marine calcifiers. Mar. Ecol. Prog. Ser. 373, 265–273.

Arp, G., Reimer, A., Reitner, J., 2001. Photosynthesis-induced biofilm calcification and calcium concentrations in Phanerozoic oceans. Science 292, 1701–1704.

Bathurst, R.G.C., 1975. Carbonate Sediments and their Diagenesis. 2nd (Ed.), Elsevier, Netherlands, pp. 93-147.

Benzerara, K., Menguy, N., Lopez-Garcıa, P., Yoon, T.-H., Kazmierczak, J., Tyliszczak, T., Guyot, F., Brown Jr., G.E., 2006. Nanoscale detection of organic signatures in carbonate microbialites. Proc. Natl. Acad. Sci. 103, 9440–9445.

Berner, R.A., 1975. The role of magnesium in the crystal growth of calcite and aragonite from sea water. Geochim. Cosmochim. Acta 39, 489–504.

Bethke, C.M., and Yeakel, S., 2016. The Geochemist's Workbench®, Release 11: GWB Essentials Guide. Aqueous Solutions LLC, Champaign, IL, pp. 188.

Braissant, O., Cailleau, G., Dupraz, C., Verrecchia, E.P., 2003. Bacterially induced mineralization of calcium carbonate in terrestrial environments: the role of exopolysaccharides and amino acids. J. Sediment. Res. 73, 485–490.

Braissant, O., Decho, A.W., Dupraz, C., Glunk, C., Przekop, K.M., Visscher, P.T., 2007. Exopolymeric substances of sulfate-reducing bacteria: interactions with calcium at alkaline pH and implication for formation of carbonate minerals. Geobiology, 5, 401–411.

Braissant, O, Decho, A.W., Przekop, K.M., Gallagher, K.L., Glunk, C., Dupraz, C., Visscher, P.T., 2009. Characteristics and turnover of exopolymeric substances in a hypersaline microbial mat. FEMS Microbiol. Ecol. 67, 293–307.

Braga, J.C., Martin, J.M., Riding, R., 1995. Controls on microbial dome fabric development along a carbonate-siliciclastic shelf-basin transect, Miocene, SE Spain. Palaios 10, 347–361.

Brenot, A., Cloquet, C., Vigier, N., Carignan, J., France-Lanord, C., 2008. Magnesium isotope systematics of the lithologically varied Moselle river basin, France. Geochim. Cosmochim. Acta 72, 5070–5089.

Buhl, D., Immenhauser, A., Smeulders, G., Kabiri, L., Richter, D.K., 2007. Time series D26Mg analysis in speleothem calcite: kinetic versus equilibrium fractionation, comparison with other proxies and implications for palaeoclimate research. Chem. Geol. 244, 715–729.

Burne, R.V, and Moore, L.S., 1987. Microbialites; organosedimentary deposits of benthic microbial communities. Palaios 2, 241–254.

Chakrabarti, R., Jacobsen, S.B., 2010. The isotopic composition of magnesium in the inner Solar System. Earth Planet. Sci. Lett. 293, 349–358.

Chang, V.T.C., Makishima, A., Belshaw, N.S., O'Nions, R.K., 2003. Purification of Mg from low-Mg biogenic carbonates for isotope ratio determination using multiple collector ICP-MS. J. Anal. At. Spectrom. 18, 296–301.

Chang, V.T.-C., Williams, R.J.P., Makishima, A., Belshawl, N.S., O'Nions, R.K., 2004. Mg and Ca isotope fractionation during $CaCO_3$ biomineralisation. Biochem. Biophys. Res. Commun. 323, 79–85.

Craig, H., 1965. The measurement of oxygen isotope paleotemperatures. In: E. Tongiorgi (Ed.), Stable Isotopes in Oceanographic Studies and Paleotemperatures, Spoleto, Consiglio Naz. Ricerche, Lab. Geol. Nucl. Nucl., Pisa, pp. 162–182.

Curran, H.A., and White, B., 1995. Introduction: Bahamas Geology. In Curran, H.A., and White, B. (Ed.), Terrestrial and Shallow Marine Geology of the Bahamas and Bermuda. Geological Society of America Special Paper 300. Boulder, Colorado, pp. 1–3.

Curran, H.A., 1997. Introduction to the Geology of the Bahamas and San Salvador Island, With an Overflight Guide. In Curran, H.A., (Ed.), Guide to Bahamian Ichnology: Pleistocene, Holocene, and Modern Environments. Bahamian Field Station, San Salvador, Bahamas, pp. 1–10.

Dauphas, N., Teng, F.-Z., Arndt, N.T., 2010. Magnesium and iron isotopes in 2.7 Ga Alexo komatiites: mantle signatures, no evidence for Soret diffusion, and identification of diffusive transport in zoned olivine. Geochim. Cosmochim. Acta 74, 3274–3291.

De Choudens-Sánchez, V., González, L.A., 2009. Calcite and Aragonite Precipitation Under Controlled Instantaneous Supersaturation: Elucidating the Role of

$CaCO_3$ Saturation State and Mg/Ca Ratio on Calcium Carbonate Polymorphism. J. Sediment. Res. 79, 363–376.

De Philippis, R., Margheri, M.C., Materassi, R., Vincenzini, M., 1998. Potential of unicellular cyanobacteria from saline environments as exopolysaccharide producers. Appl. Environ. Microbiol. 64, 1130–1132.

De Villiers, S., Dickson, J.A.D., Ellam, R.M., 2005. The composition of the continental river weathering flux deduced from seawater Mg isotopes. Chem. Geol. 216, 133–142.

Depaol, D.J., 2011. Surface kinetic model for isotopic and trace element fractionation during precipitation of calcite from aqueous solutions. Geochim, Cosmochim, Acta, 75, 1039–1056.

Dupraz, C., Strasser, A., 1999. Microbialites and micro-encrusters in shallow coral bioherms (Middle–Late Oxfordian, Swiss Jura Mountains). Facies 40, 101–130.

Dupraz, C., Strasser, A., 2002. Nutritional modes in coral-microbialite reefs (Jurassic, Oxfordian, Switzerland): evolution of trophic structure as a response to environmental change. Palaios 17, 449–471.

Dupraz, C., Visscher, P.T., Baumgartner, L.K., Reid, R.P., 2004. Microbe–mineral interactions: early carbonate precipitation in a hypersaline lake (Eleuthera Island, Bahamas). Sedimentology 51, 745–765.

Dupraz, C., Visscher, P.T., 2005. Microbial lithification in marine stromatolites and hypersaline mats. Trends Microbiol. 13, 429–438.

Dupraz, C., Patissina, R., Verrecchia, E.P., 2006. Simulation of stromatolite morphospace using 'DLA-CA' growth model': translation of energy in morphology. Sediment. Geol. 185, 185–203.

Dupraz, C., Reid, R.P., Braissant, O., Decho, A.W., Norman, R.S., Visscher, P.T., 2009. Processes of carbonate precipitation in modern microbial mats. Earth-Sci. Rev. 96, 141–162.

Dupraz, C., Fowler, A., Tobias, C., Visscher, P.T., 2013. Stromatolitic knobs in Storr's Lake (San Salvador, Bahamas): a model system for formation and alteration of laminae. Geobiology 11, 527–548.

Durov, S.A., 1948. Classification of natural waters and graphical representation of their composition. Dokl. Akad. Nauk. USSR. 59 (1), 87–90.

Eisenhauer, A., Kisakrüek, B., Böhm, F., 2009. Marine calcification: An alkali earth metal isotope perspective. Elements 5, 365–368.

Fantle, M.S. and Depaolo ,D.J. 2007. Ca isotopes in carbonate sediment and pore fluid from ODP Site 807A: The Ca^{2+}(aq)-calcite equilibrium fractionation factor and calcite recrystallization rates in Pleistocene sediments. Geochim, Cosmochim, Acta 71, 2524–2546.

Feldmann, M., and McKenzie, J., 1998. Stromatolite-thrombolite association in a modern environment, Lee Stocking Island, Bahamas. Palaios 13, 201–212.

Fernandez-Diaz, L., Putnis, A., Prieto, M., Putnis, C.V., 1996. The role of magnesium in the crystallization of calcite and aragonite in a porous medium. J. Sediment. Res. 66, 482–491.

Finch, A.A. and Allison, N., 2008. Mg structural state in coral aragonite and implications for the paleoenvironmental proxy. Geophys. Res. Lett. 35, 1–5.

Fowler, A.J., 2011. Stromatolitic knobs in Storr's Lake, San Salvador, Bahamas: insights into organomineralization. [Master's thesis], University of Connecticut, Storrs, CT.

Folk, R.L., 1959. Practical petrographic classification of limestones. AAPG Bulletin. 43, 1–38.

Foster, G.L., Strandmann, P.A.E.P., von Rae, J.W.B., 2010. Boron and magnesium isotopic composition of seawater. Geochem. Geophys. Geosyst. 11, 1–10.

Freytet, P., and Plet, A., 1996. Modern freshwater microbial carbonates: the Phormidium stromatolites (Tufa-travertine) of southeastern Burgundy (Paris Basin, France). Facies 34, 219–238.

Freytet, P., and Verrecchia, E.P., 1998. Freshwater Organisms that Build Stromatolites: a Synopsis of Biocrystallization by Prokaryotic and Eukaryotic Algae. Sedimentology 45, 535–563.

Galy, A., Bar-Matthews, M., Halicz, L., O'Nions, R.K., 2002. Mg isotopic composition of carbonate: insight from speleothem formation. Earth Planet. Sci. Lett. 201, 105–115.

Galy, A., Yoffe, O., Janney, P., Williams, R., Cloquet, C., Alard, O., Halicz, L., Wadhwa, M., Hutcheon, I., Ramon, E., Carignan, J., 2003. Magnesium-isotope heterogeneity of the isotopic standard SRM980 and new reference materials for magnesium- isotope-ratio measurements. J. Anal. Atom. Spect. 18, 1352–1356.

Gallagher, K.L., Kading, T.K., Braissant, O., Dupraz, C., Visscher, P.T., 2012. Inside the Alkalinity Engine: The role of electron donors in the organomineralization potential of sulfate-reducing bacteria. Geobiology 10, 518–530.

Giovannoni, S.J. and Revsbech, N.P., 1987. Obligately phototrophic Chloroflexus: primary production in anaerobic hot spring microbial mats. Arch. Microbiol. 147, 80–87.

Given, R.K. and Wilkinson, B.H., 1985. Kinetic control of morphology, composition, and mineralogy of abiotic sedimentary carbonates. J. Sediment. Petrol. 55, 109–119.

Glunk, C., Dupraz, C., Braissant, O., Gallagher, K.L., Verrecchia, E.P., Visscher, P.T., 2011. Microbially Mediated Carbonate Precipitation in a Hypersaline Lake, Big Pond (Eleuthera, Bahamas). Sedimentology 58, 720–738.

Green B., 1993. IUPAC Quantities, Units, and Symbols in Physical Chemistry, 2nd (Ed.), Blackwell Scientific Publications, Oxford, pp 59.

Gussone, N., Eisenhauer, A., Heuser, A., Dietzel, M., Bock, B., Böhm, F., Spero, H.J., Lea, D.W., Bijma, J., Nägler, T., 2003. Model for kinetic effects on calcium isotope fractionation () in inorganic aragonite and cultured planktonic foraminifera. Geochim. Cosmochim. Acta 67, 1375–1382.

Gussone, N., Böhm, F., Eisenhauer, A., Dietzel, M., Heuser, A., Teichert, B.M.A, Reitner, J., Wörheide, G., Dullo, W.-C. 2005. Calcium isotope fractionation in calcite and aragonite. Geochim. Cosmochim. Acta 69, 4485–4495.

Han, Y.S., Hadiko, G., Fuji, M., Takahashi, M., 2006. Crystllizaiton and transformation of vaterite at controlled pH. J. Cryst. Growth 289, 269-274.

Harland, W.B., Armstrong, R.L., Cox, A.V., Craig, L.E., Smith, A.G., Smith, D.G., 1990. A Geologic Time Scale 1989. Cambridge University Press, Cambridge, pp. 3.

Hattin, D.T., 1982. Holocene Lithification of Carbonate Sediments, San Salvador Island, Bahamas. In Gerace, D.T. (Ed.) Proceedings of the First Symposium on the Geology of the Bahamas. CCFL Field Station, San Salvador, Bahamas, pp. 45–62.

Higgins, J.A. and Schrag, D.P., 2012. Records of Neogene seawater chemistry and diagenesis in deep-sea carbonate sediments and pore fluids. Earth Planet. Sci. Lett., 386–396,

Hippler, D., Buhl, D., Witbaard, R., Richter, D.K., Immenhauser, A., 2009. Towards a better understanding of magnesium-isotope ratios from marine skeletal carbonates. Geochim. Cosmochim. Acta 73, 6134–6146.

Hofmann, H.J., Grey, A.H., Hickman, A.H., Thorpe, R.I., (1999): Origin of 3.45 Ga coniform stromatolites in Warrawoona Group, Western Australia. Geol. Soc. Am. Bull. 111, 1256–1262.

Imhoff, J.F., Hiraishi, A., Suling, J., 2006. Anoxygenic Phototrophic Purple Bacteria. In: 2nd (Ed.) Bergey's Mannual of Systematic Bacteriology, vol. 2, Springer, pp. 119–132.

Immenhauser, A., Buhl, D., Richter, D., Niedermayr, A., Riechelmann, D., Dietzel, M., Schulte, U., 2010. Magnesium-isotope fractionation during low-Mg calcite precipitation in a limestone cave—field study and experiments. Geochim. Cosmochim. Acta 74, 4346–4364.

Jacobson, A.D., Zhang, Z., Lundstrom, C.C., Huang, F., 2010. Behavior of Mg isotopes during dedolomitization in the Madison Aquifer, South Dakota. Earth Planet. Sci. Lett. 297, 446–452.

Jin, D., Wang, F., Yue, L., 2011. Phase and morphology evolution of vaterite crystals in water/ethanol binary solvent. Cryst. Res. Technol. 46, 140-144.

Johnson, C.M., Beard, B.L., Albarede, F., 2004. Overview and general concepts. In: Johnson C.M., Beard B.L., Albarede F. (Eds), Geochemistry of Non-Traditional Stable Isotopes. Reviews in Mineralogy & Geochemistry, vol. 55. Mineralogical Society of America, Washington D.C., pp. 1–24.

Jonkers, H.M., Ludwig, R., De Wit, R., Pringault, O., Muyzer, G., Niemann, H., Finke, N., De Beer, D., 2003. Structural and functional analysis of a microbial mat

ecosystem from a unique permanent hypersaline inland lake: 'La Salada de Chiprana' (NE Spain). FEMS Microbiol. Ecol. 44, 175–189.

Kennard, J.M., and James, N.P., 1986. Thrombolites and stromatolites: Two distinct types of microbial structures. Palaios 1, 492–503.

Konhauser, K., 2007. Introduction to Geomicrobiology. Blackwell Science, UK.

Krauskopf, K.B. and Bird, D.K., 1994. Introduction to Geochemistry, 3rd (Ed.), McGraw-Hill, New York, pp. 721.

Lemarchand, D., Wasserburg, G.J., Papanastassiou, D.A., 2004. Rate-controlled calcium isotope fractionation in synthetic calcite. Geochim. Cosmochim. Acta 68, 4665–4678.

Li, W., Chakraborty, S., Beard, B.L., Romanek, C.S., Johnson C.M., 2012. Magnesium isotope fractionation during precipitation of inorganic calcite under laboratory conditions. Earth Planet. Sci. Lett. 333-334, 204–316.

Li, W.-Y., Teng, F.-Z., Ke, S., Rudnick, R.L., Gao, S., Wu, F.-Y., Chappell, B.W., 2010. Heterogeneous magnesium isotopic composition of the upper continental crust. Geochim. Cosmochim. Acta 74, 6867–6884.

Liu, S.-A., Teng, F.-Z., He, Y., Ke, S., Li, S., 2010. Investigation of magnesium isotope fractionation during granite differentiation: Implication for Mg isotopic composition of the continental crust. Earth Planet. Sci. Lett. 297, 646–654.

Lloyd, J.A., and Heathcote, J.A., 1985. Natural inorganic hydrochemistry in relation to groundwater: An introduction. Oxford Uni. Press, New York, pp. 296.

Loste, E., Wilson, R.M., Seshadri, R., Meldrum, F.C., 2003. The role of magnesium in stabilising amorphous calcium carbonate and controlling calcite morphologies. J. Cryst. Growth 254, 206–218.

Mackenzie, F.T., Bischoff, W.D., Bishop, F.C., Loijens, M., Schoonmaker, J., Wollast, R., 1983. Magnesium calcites; low temperature occurrence, solubility and solid state behavior. Rev. Mineral. Geochem. 11, 97–144.

Mann, C.J., and Hoffman, L.R., 1984. Algal mounds in Storr's Lake, San Salvador, Bahamas. In Gerace, D.T. (Ed.), Proceedings of the Second Symposium on the Geology of the Bahamas. CCFL Bahamian Field Station, San Salvador, Bahamas, pp. 41–51.

Mann, C.J., and Nelson, W.M., 1989. Microbialitic structures in Storr's Lake, San Salvador Island, Bahamas Islands. Palaios 4, 287–293.

Marriott, C.S., Henderson, G.M., Belshaw, N.S., Tudhope, A.W., 2004. Temperature dependence of δ^7Li, δ^{44}Ca and Li/Ca during growth of calcium carbonate. Earth Planet. Sci. Lett. 222, 615–624.

Mavromatis, V., Gautier, Q., Bosc, O., Schott, J., 2013. Kinetics of Mg partition and Mg stable isotope fractionation during its incorporation in calcite. Geochim. Cosmochim. Acta 114, 188–203.

McNeese, L.R., 1988. Modern Stromatolites in hypersaline Storr's Lake, San Salvador, Bahamas. [Master's thesis], University of North Carolina Chapel Hill, pp. 95.

Merz-Preiß, M., 1992. The biology of carbonate precipitation by cyanobacteria. Facies 26, 81–102.

Monty, C.L.V., 1976. The origin and development of crypalgal fabric. In: Walter, M.R. (Ed.), Stromatolites. Developments in Sedimentology, vol. 55, Elsevier, Amsterdam, pp.193–249.

Morse, J.W., Wang, Q., Tsio, M.Y., 1997. Influences of temperature and Mg:Ca ratio on $CaCO_3$ precipitates from seawater. Geology 25: 85–87.

Mullins, H.T., and Lynts, G.W., 1977. Origin of the Northwestern Bahama Platform: Review and Reinterpretation. Geol. Soc. Am. Bull. 88, 1147–1161.

Myshrall, K.L., Mobberley, J.M., Green, S.J., Visscher, P.T., Havemann, S.A., Reid, R.P., Foster, J.S., 2010. Biogeochemical cycling and microbial diversity in the thrombolitic microbialites of Highborne Cay, Bahamas. Geobiology 8, 337–354.

Nebel, H., Epple, M., 2008. Continuous preparation of calcite, aragonite and vaterite and of magnesium-substituted amorphous calcium carbonate (Mg-ACC). Z. fur Anoranische allg. Chem. 634, 1439–1443.

Neumann, C.A., Bebout, B.M., McNeese, L.R., Paul, C.K., Paerl, H.W., 1989. Modern stromatolites and associated mats: San Salvador, Bahamas. In: Mylroie, J. (Ed.), Proceedings of the 4th Symposium on the Geology of the Bahamas. Bahamas Field Station, San Salvador, Bahamas, pp. 235–251.

Nicholson, J.A.M., Stolz, J.F., Pierson, B.K., 1987. Structure of a microbial mat at Great Sippewissett Marsh, Cape Cod, Massachusetts. FEMS Microbiol. Lett. 45, 343–364.

Nielsen, L.C., de Yoreo, J.J., DePaolo, D.J., 2013. General model for calcite growth kinetics in the presence of impurity ions. Geochim. Cosmochim. Acta 115,100–114.

Overmann, J. and van Gemerden, H., 2000. Microbial interactions involving sulfur bacteria: implications for the ecology and evolution of bacterial communities. FEMS Microbiol. Rev. 24, 591–599.

Park, L.E., 2012. Comparing two long-term hurricane frequency and intensity records from San Salvador Island, Bahamas. J. Coastal Res. 28, 891–902.

Patterson, W.P. and Walter, L.M., 1994. Depletion of ^{13}C in seawater $\sum CO_2$ on modern carbonate platforms: Significance for the carbon isotopic record of carbonates. Geology, 22, 885–888.

Paul, V.G., Wronkiewicz, D.J., Mormile, M.R., 2016. Mineralogy and microbial diversity of the microbialites in the hypersaline Storr's Lake, the Bahamas. Astrobiology 16, 282–299.

Paull, C.K., Neumann, A.C., Bebout, B., Zabielski, V., Showers, W., 1992. Growth rate and stable isotopic character of modern stromatolites from San Salvador, Bahamas. Palaeogeogr. Palaeoclimatol. Palaeoecol. 95, 335–344.

Pearce, C.R., Saldi, G.D., Schott, J., Oelkers, E.H., 2012. Isotopic fractionation during congruent dissolution, precipitation and at equilibrium: Evidence from Mg isotopes. Geochim. Cosmochim. Acta 92, 170–183.

Pentecost, A., 1989. Observations on the *Scytonema* mats of San Salvador, Bahamas. In Mylroie, John E. (Ed.), Proceedings of the Fourth Symposium on the Geology of the Bahamas. CCFL Bahamian Field Station, San Salvador, Bahamas, pp. 295–302.

Pentecost, A., 2005. Travertine. Springer, The Netherlands.

Pinckney, J., Paerl, H.W., Fitzpatrick, M., 1995. Impacts of seasonality and nutrients on microbial mat community structure and function. Mar. Ecol. Prog. Ser. 123, 207–216.

Planavsky, N. and Ginsburg, R.N., 2009. Taphonomy of modern marine Bahamian microbialites. Palaios 24, 5–17.

Planavsky, N., Reid, R.P., Lyons, T.W., Myshrall, K.L., Visscher, P.T., 2009. Formation and diagenesis of modern marine calcified cyanobacteria. Geobiology 7, 566–576.

Pogge von Strandmann, P.A.E., Burton, K.W., James, R.H., van Calsteren, P., Gislason, S.R., Sigfusson, B., 2008a. The influence of weathering processes on riverine magnesium isotopes in a basaltic terrain. Earth Planet. Sci. Lett. 276, 187–197.

Pogge von Strandmann, P.A.E., James, R.H., van Calsteren, P., Gislason, S.R., Burton, K.W., 2008b. Lithium, magnesium and uranium isotope behaviour in the estuarine environment of basaltic islands. Earth Planet. Sci. Lett. 274, 462–471.

Reid, R.P., Visscher, P.T., Decho, A.W., Stolz, J.F., Bebout, B.M., Dupraz, C., Macintyre, I.G., Paerl, H.W., Pinckney, J.L., Prufert-Bebout, L., Steppe, T.F., DesMarais, D.J., 2000. The role of microbes in accretion, lamination and early lithification of modern marine stromatolites. Nature 406, 989–992.

Reid, R.P, James, N.P., Macintyre, I.G., Dupraz, C., Burne, R.V., 2003. Shark Bay stromatolites: Microfabrics and reinterpretation of origins. Facies 49, 45–53.

Reimer, Adreas., 2011. Alkalinity. In Reitner, Joachim, and Thiel, Volker (Eds), Encyclopedia of Geobiology. Springer, University of Göttingen, Germany, pp. 20–24.

Riding, R., 2000. Microbial carbonates: the geological record of calcified bacterial- algal mats and biofilms. Sedimentology 47, 179–214.

Riding, R., 2011. Microbialites, stromatolites, and thrombolites. In J. Reitner and V. Thiel (Eds), Encyclopedia of Geobiology. Encyclopedia of Earth Science Series, Springer, Heidelberg, pp. 635-654.

Riding, R., 1991. Classification of microbial carbonates. In Riding, R. (Ed.), Calcareous Algae and Stromatolites. Springer-Verlag, New York, pp. 21-51.

Rosman, K.J.R. and Taylor, P.D.P., 1998. Isotopic compositions of the elements. Pure Appl. Chem. 70, 217-235.

Rubinson, M. and Clayton, R.N., 1969. Carbon-13 fractionation between aragonite and calcite. Geochim. Cosmochim. Acta 33, 997–1002.

Saenger, C., Wang, Z., Gaetani, G., Cohen, A.L., Lough, J.M., 2013. The influence of temperature and vital effects on magnesium isotope variability in Porites and Astrangia corals. Chem. Geol., 105–117.

Saenger, C. and Wang, Z., 2014. Magnesium isotope fractionation in biogenic and abiogenic carbonates: implications for paleoenvironmental proxies. Quat. Sci. Rev. 90, 1–21.

Saulnier, S., Rollion-Bard, C., Vigier, N., Chaussidon, M., 2012. Mg isotope fractionation during calcite precipitation: an experimental study. Geochim. Cosmochim. Acta 91, 75–91.

Schauble, E.A., 2011. First-principles estimates of equilibrium magnesium isotope fractionation in silicate, oxide, carbonate and hexaaquamaanesium(2+) crystals. Geochim. Cosmochim. Acta 75, 844–869.

Schieber, J. and Arnott, J., 2003. Nannobacteria as a byproduct of enzyme-driven tissue decay. Geology 31, 717–720.

Schopf, J.W., 2006. Fossil evidence of Archaean life. Phil. Trans. R. Soc. B 361, 869–885.

Shapiro, R.S., 2000. A comment on the systematic confusion of thrombolites. Palaios 15, 166–169.

Shirokova, L.S., Mavromatis, V., Bundeleva, I.A., Pokrovsky, O.S., Bénézeth, P., Gérard, E., Pearce, C.R. Oelkers, E.H., 2013. Using Mg isotopes to trace cyanobacterially mediated magnesium carbonate precipitation in alkaline lakes. Aquat. Geochem. 19, 1–24.

Sommers, M., Awramik, S., Woo, K., 2000. Evidence for initial calcite-aragonite composition of Lower Algal Chert Member ooids and stromatolites, Paleoproterozoic Gunflint Formation, Ontario, Canada. Can. J. Earth. Sci. 37, 1229–1243.

Stephenson, A.E., DeYoreo, J.J., Wu, L., Wu, K.J., Hoyer, J., Dove, P.M., 2008. Peptides enhance magnesium signature in calcite: insights into origins of vital effects. Science 322, 724– 727.

Stumm, W. and Morgan, J.J., 1996. Aquatic Chemistry. John Wiley & Sons, New York., pp. 780.

Suarez-Gonzalez, Quijada, P.I.E., Benito, M.I., Mas, R., Merinero, R., Riding, R., 2014. Origin and significance of lamination in Lower Cretaceous stromatolites and proposal for a quantitative approach. Sediment. Geol. 300, 11–27.

Sutherland, I.A., 2001. Biofilm exopolysaccharides: a strong and sticky framework. Microbiology 147, 3–9.

Tang. J., Köhler. S.J., Dietzel. M., 2008a. Sr^{2+}/Ca^{2+} and $^{44}Ca/^{40}Ca$ fractionation during inorganic calcite formation: I. Sr incorporation. Geochim. Cosmochim. Acta 72, 3718–3732.

Tang, J., Dietzel, M., Böhm, F., Köhler, S.J. Eisenhauer, A., 2008b. Sr^{2+}/Ca^{2+} and $^{44}Ca/^{40}Ca$ fractionation during inorganic calcite formation: II. Ca isotopes. Geochim. Cosmochim. Acta 72, 3733–3745.

Teng, F.-Z., Wadhwa, M., Helz, R.T., 2007. Investigation of magnesium isotope fractionation during basalt differentiation: implications for a chondritic composition of the terrestrial mantle. Earth Planet. Sci. Lett. 261, 84–92.

Teng, F.-Z., Li, W.-Y., Ke, S., Marty, B., Dauphas, N., Huang, S., Wu, F.-Y., Pourmand, A., 2010. Magnesium isotopic composition of the Earth and chondrites. Geochim. Cosmochim. Acta 74, 4150–4166.

Tipper, E.T., Galy, A., Bickle, M.J., 2006. Riverine evidence for a fractionated reservoir of Ca and Mg on the continents: implications for the oceanic Ca cycle. Earth Planet. Sci. Lett. 247, 267–279.

Tipper, E.T., Galy, A., Bickle, M.J., 2008. Calcium and magnesium isotope systema- tics in rivers draining the Himalaya–Tibetan-Plateau region: lithological or fractionation control? Geochim. Cosmochim. Acta 72, 1057–1075.

Tipper, E.T., Gaillardet, J., Louvat, P., Capmas, F., White, A.F., 2010. Mg isotope constraints on soil pore-fluid chemistry: evidence from Santa Cruz, California. Geochim. Cosmochim. Acta 74, 3883–3896.

Tarutani, T., Clayton, R.N., Mayeda, T.K., 1969. The effect of polymorphism and magnesium substitution on oxygen isotope fractionation between calcium carbonate and water. Geochim. Cosmochim. Acta 33, 987–996.

Turner, E.C., James, N.P., Narbonne, G.M., 2000. Taphonomic control on microstructure in Early Neoproterozoic reefal stromatolites and thrombolites. Palaios 15, 87-111.

Van Lith, Y., Warthmann, R., Vasconcelos, C., McKenzie, J.A., 2003. Microbial fossilization in carbonate sediments: a result of the bacterial surface involvement in dolomite precipitation. Sedimentology 50, 237–245.

Vasconcelos, C., Warthmann, R., McKenzie, J.A., Visscher, P.T., Bittermann, A.G., van Lith, Y., 2006. Lithifying microbial mats in Lagoa Vermelha, Brazil: Modern Precambrian relics? Sediment. Geol. 185: 175–183.

Vasconcelos, C., McKenzie, J.A., 1997. Microbial mediation of modern dolomite precipitation and diagenesis under anoxic conditions (Lagoa Vermelha, Rio de Janeiro, Brazil). J. Sediment. Res. 67, 378–390.

Verrecchia, E.P., Freytet, P., Verrecchia, K.E., Dumont, J.L., 1995. Spherulites in calcrete laminar crusts: biogenic $CaCO_3$, precipitation as a major contributor to crust formation. J. Sediment. Res. 65, 690–700.

Visscher, P.T., Reid, R.P., Bebout, B.M., 2000. Microscale observations of sulfate reduction: Correlation of microbial activity with lithified micritic laminae in modern marine stromatolites. Geology 28, 919–922.

Visscher, P.T., and Stolz, J.F., 2005. Microbial mats as bioreactors: populations, processes and products. Paleogeogr. Paleoclimatol. Paleooecol. 219, 87–100.

Warthmann, R., van Lith, Y., Vasconcelos, C., McKenzie, J.A., Karpoff, A.M., 2000. Bacterially induced dolomite precipitation in anoxic culture experiments. Geology 28, 1091–1094.

Wang, D., Hamm, L.M., Giuffre, A.J., Echigo, T., Rimstidt, J.D., De Yoreo, J.J., Grotzingerc, J., Dove, P.M., 2012. Revisiting geochemical controls on patterns of carbonate deposition through the lens of multiple pathways to mineralization. Farad. Discuss. 159: 371–386.

Wang, Z., Hu, P., Gaetani, G., Liu, C., Saenger, C., Cohen, A., Hart, S., 2013. Experimental calibration of Mg isotope fractionation between aragonite and seawater. Geochim. Cosmochim. Acta 102, 113–123.

Weiner, S. and Dove, P.M., 2003. An overview of biomineralization processes and the problem of the vital effect. Reviews in Mineralogy and Geochemistry 54, 1–29.

White, W.M., 2015. Isotope Geochemistry, Wiley-Blackwell, Chichester, pp. 363.

Wiechert, U., Halliday, A.N., 2007. Non-chondritic magnesium and the origins of the inner terrestrial planets. Earth Planet. Sci. Lett. 256, 360–371.

Wimpenny, J., Burton, K.W., James, R.H., Gannoun, A., Mokadem, F., Gislason, S.R., 2011. The behaviour of magnesium and its isotopes during glacial weathering in an ancient shield terrain in West Greenland. Earth Planet. Sci. Lett. 304, 260–269.

Wombacher, F., Eisenhauer, A., Heuser A., Weyer, S., 2009. Separation of Mg, Ca and Fe from geological reference materials for stable isotope ratio analyses by MC-ICP-MS and double-spike TIMS. J. Anal. At. Spectrom. 24, 627–636.

Wombacher, F., Eisenhauer, A., Böhm, F., Gussone, N., Regenberg, M., Dullo, W.-Chr., Rüggeberg, A., 2011. Magnesium stable isotope fractionation in marine biogenic calcite and aragonite. Geochim. Cosmochim. Acta 75, 5797–5818.

Zabielski, V.P., 1991. The depositional history of Storr's Lake San Salvador Island, Bahamas [PhD thesis]: University of North Carolina Chapel Hill, pp. 1-24.

Zavarzin, G.A., 2002. Microbial geochemical calcium cycle. Microbiology 71, 5–22.

Zeebe, R.E. and Wolf-Gladrow, D., 2001. CO_2 in Seawater: Equilibrium, Kinetics and Isotopes. (Eds.), Elsevier, New York, pp. 346.

Biographical Information

Zijian Li received a Bachelor of Science with a major in geology from China University of Geosciences, Beijing in July 2014. He entered The University of Texas at Arlington in July 2015 for Master's study and he will graduate in August 2017. His research interest is geochemistry. The project that he is working on is Mg isotope investigation of stromatolites from Storr's Lake, Bahamas. He will pursue a Ph.D. degree after Master's graduation.